THE UNIVERSITY *of* EDINBURGH

Frequency-dependent anisotropy in partially saturated rocks

Zhaoyu Jin

Thesis submitted in fulfilment of

the requirements for the degree of

Doctor of Philosophy

School of GeoSciences

The University of Edinburgh

2019

Declaration

I declare that this thesis has been composed by myself and that it has not been submitted, in whole or in part, in any previous application for a degree. Except where states otherwise by reference or acknowledgement, the work presented is entirely my own.

Zhaoyu Jin

July 2019

Abstract

Seismic wave propagation through fractured rocks is greatly influenced by the fracture system and fluid content. This has become increasingly apparent from recent laboratory measurements and field observations which have shown evidence that seismic anisotropy varies systematically with frequency and fluid saturation. Exploiting this behaviour for reservoir characterization relies on the availability of adequate theoretical rock physics models.

Many previous theories on frequency-dependent anisotropy have been limited to the single fluid assumption, despite the fact that almost all reservoirs are partially saturated. This thesis focuses on improving the understanding of multiphase saturation effects on anisotropic seismic wave response in reservoirs containing aligned fractures. I do this by theoretically deriving expressions for the anisotropic frequency-dependent elastic constants. These depend on the relative mobilities of the saturating fluids and the coupled impact of 'squirt flow' and 'patch saturation' effects, which have previously been considered independently, on anisotropic seismic wave propagation. The effect of relative permeability is pronounced; fluid mobility can be lower in partially saturated rocks compared to the fully saturated case, and this can lead to a stiffening which dominates compressibility effects. This can result in unexpected non-monotonic relationships between moduli and water saturation, complicating attempts to invert saturation from seismic data.

I test the theory against laboratory measurements carried out at the National Oceanography Centre, Southampton (NOCS) of S-wave splitting and P-wave anisotropy in synthetic fractured sandstones saturated by mixtures of both water/air and brine/CO_2. I demonstrate that both squirt and patch mechanisms are significant for the interpretation

of saturation effects on frequency-dependent anisotropy.

I use the theory to predict the impact of anisotropic dispersion on azimuthal P-wave reflections based on an sand model with transverse isotropy with horizontal axis of symmetry (HTI) overlaid by shale with transverse isotropy with vertical axis of symmetry (VTI). Although VTI in the overburden does not lead to azimuthal anisotropy, its effect on angle dependence could significantly affect the azimuthal Amplitude-Versus-Offset (AVO) responses at far offsets. I show a modest effect on the amplitude and large effect on the phase, the latter of which could even be mistaken for azimuthal velocity variations. I present a Bayesian inversion based on a forward modelling technique aimed at recovering water saturation, fracture density and fracture length of an HTI sand. The results show potential of using frequency-dependent azimuthal AVO for the discrimination of large-scale fractures from micro-scale cracks.

Lay summary

In the Earth's crust, fractures are perhaps the most abundant geological features. They can significantly influence permeability and fluid flow in the subsurface. Characterizing fracture systems in a subsurface reservoir is therefore important to various applications including hydrocarbon production and geological storage of CO_2.

Fractures are known to cause seismic anisotropy, which is defined as the dependence of seismic wave velocity on the direction of wave propagation. Seismic anisotropy is also greatly influenced by fluid contents in the pore space of the fractured rock. Knowledge of how pore fluids and fractures can affect seismic wave propagation is therefore needed for obtaining these physical properties from seismic data. Recent field observations and laboratory measurements have shown evidence that seismic anisotropy varies systematically with frequency and fluid saturation. Exploiting this behaviour for reservoir characterization relies on the availability of adequate theoretical rock physics models. Many previous theories considering such frequency and fluid dependences have been limited to the single fluid assumption, despite the fact that almost all reservoirs are partially saturated.

To address this problem, I develop a theory that describes anisotropic seismic wave response in partially saturated reservoirs containing aligned fractures. The theory emphasizes combined effects of wave-induced fluid flow, uneven fluid pressures and effective fluid mobility on the behaviour of frequency-dependent anisotropy. Testing the theory against recent laboratory measurements suggests that these effects are significant for the interpretation of saturation effects on seismic anisotropy. I also demonstrate potential application of this theory to recovering water saturation, fracture density and fracture size of a partially saturated reservoir from seismic data.

Acknowledgements

I would like to thank my supervisors, Mark Chapman and Ian Main, for their guidance and support throughout my PhD in Edinburgh.

I would also like to thank Giorgos Papageorgiou and Ismael Falcon-Suarez for their help with developing the theory and modelling experimental data.

I thank Xiaoyang Wu, Phillip Cilli, Li Yang and Yangkang Chen for many inspiring discussions, and my friends in Edinburgh for many enjoyable days.

I am grateful to financial support of Principal's Career Development PhD Scholarship and Edinburgh Global Research Scholarship from the University.

Finally, I wish to express my gratitude to Yan Cheng and my family, Quelin Jin and Hanqin Zhu, for their love, support and encouragement.

Contents

Declaration **I**

Abstract **III**

Lay summary **V**

Acknowledgements **VII**

Contents **IX**

List of Figures **XIII**

List of Tables **XIX**

1 Introduction **1**

2 Review of seismic anisotropy **7**

2.1 Overview 7

2.2 Anisotropic form of Hooke's law 9

2.3 Anisotropic symmetry system 11

2.4 Thomsen's parameters for VTI medium 14

2.5 Equivalent medium theory for fracture characterization 16

2.6 S-wave splitting 19

2.7 Azimuthal P-wave anisotropy 20

3 Review of poroelasticity **23**

3.1 Biot-Gassmann theory of poroelasticity 23

3.2 Squirt flow 26

3.3 Frequency-dependent anisotropy 28
3.4 Partial saturation effects 33

4 Derivation of a squirt-patchy model 39
4.1 Introduction 39
4.2 Expression of fluid mass in an inclusion 40
4.3 Fluid mass exchange based on Darcy's law 43
4.4 Solution of the elastic constants 46
4.5 The isotropic limit of the model 49
4.6 Analysis of the model 50
4.7 Conclusion 55

5 Partial saturation effects on frequency-dependent anisotropy 57
5.1 Introduction 57
5.2 Theory and methods 58
5.3 Numerical example- the absence of fractures 60
5.4 Numerical example- the presence of fractures 64
5.4.1 Saturation effects on S-wave anisotropy 64
5.4.2 Saturation effects on P-wave anisotropy 67
5.5 The impact of relative permeability 72
5.6 Modelling experimental results 73
5.6.1 Case one: water/air saturations 74
5.6.2 Case two: brine/CO_2 saturations 77
5.7 Conclusion 81

6 Frequency-dependent azimuthal effects on P-wave reflections 83
6.1 Introduction 84
6.2 Theory and methods 86
6.2.1 Calculation of reflection coefficients in anisotropic media 86
6.2.2 Forward modelling of seismic reflections in anisotropic dispersive media 92

6.3 Frequency-dependent azimuthal AVO 92
6.4 Bayesian inversion for fluid and fracture properties 102
6.5 Conclusions 106

7 Conclusions and discussion **107**
7.1 Conclusions 107
7.2 Discussion and future work 108

References **115**

Publications **133**

List of Figures

2.1 (a) The VTI model; (b) The HTI model (from Tsvankin, 2001). 12

2.2 The orthorhombic anisotropy model (from Tsvankin, 2001). 13

3.1 Effective bulk moduli of water-gas mixture calculated by the Reuss (equation 3.22), Voigt (equation 3.24) and Brie (equation 3.25 with $e = 3$) averages. 35

4.1 The variation of the effective fluid bulk modulus K_f, predicted by equation 4.26, with water saturation for various values of q. 52

4.2 The relative permeability model $\kappa_w = S_w^n; \kappa_g = (1 - S_w)^n$ under various values of n. 53

4.3 The variation of the grain-scale characteristic frequency ω_m and the fracture-scale characteristic frequency ω_f with water saturation for various values of n. The patch parameter q is assumed to be $10q_0$. 54

4.4 The variation of the grain-scale characteristic frequency ω_m and the fracture-scale characteristic frequency ω_f with water saturation for various values of the patch parameter q. The relative permeability model is chosen as $\kappa_w = S_w^3; \kappa_g = (1 - S_w)^3$. 54

5.1 The variation of shear modulus with water saturation for a range of frequencies and the patch parameters q in the absence of fractures. 61

5.2 The variation of S-wave velocity with water saturation for a range of frequencies and the patch parameters q in the absence of fractures. 62

5.3 The variation of S-wave attenuation with water saturation for a range of frequencies and the patch parameters q in the absence of fractures. 63

5.4 The variation of SWS with water saturation for a range of frequencies and the patch parameters q in the presence of fractures. Propagation is at 70 degrees to the fracture normal. 65

5.5 The variation of SWS, Quasi S-wave velocity and Pure S-wave velocity with frequency at various water saturations and q values. Propagation is at 70 degrees to the fracture normal. The dashed line represents the fracture-scale frequency ω_0', and the dotted line represents the grain-scale frequency ω_0. 66

5.6 The variation of Quasi P-wave velocity with frequency for a range of water saturations and the patch parameters q in the presence of fractures. On the left is propagation normal to fractures. On the right is propagation parallel to fractures. 69

5.7 The variation of Quasi P-wave velocity with angle for a range of water saturations and the patch parameters q in the presence of fractures. On the left is zero wave frequency; On the middle is ω_0' wave frequency; On the right is $100\omega_0'$ wave frequency. 70

5.8 The variation of Quasi P-wave velocity with water saturation for a range of frequencies and the patch parameters q in the presence of fractures. Propagation is along the fracture normal. 71

5.9 The variation of (a) shear modulus and (b) SWS with water saturation for a range of q values at the reference frequency ω_0. The red curves represent the case with relative permeability effects; The blue curves represent the case given by equation 5.3 without relative permeability effects. 72

5.10 Model fit to the SWS trend measured by Amalokwu et al. (2014). (a) Misfits between data and model predictions at various combinations of ω_0' and q. The location of the minimum misfit is labelled with white circle; (b) Best fitting curve to the measured SWS. 76

5.11 Fitting curves for P-wave moduli varying with water saturation measured by Amalokwu et al. (2015). 76

5.12 P- and S-wave velocities for the whole range of brine saturation measured from the Brine-CO_2 flow-through test in fractured sandstone. Solid and empty symbols indicate drainage and imbibition conditions, respectively. . 78

5.13 (a) The characteristic frequencies of the Brine-CO_2 saturated sample; (b) The Brooks-Corey relative permeability model with $\lambda_{B-C} = \frac{1}{6}$. 79

5.14 Model fit to P-wave velocities varying with brine saturation measured by Falcon-Suarez et al. (2019). 80

5.15 Model fit to S-wave velocities varying with brine saturation measured by Falcon-Suarez et al. (2019). The red symbols indicate the faster S_1 wave data, and the blue symbols indicate the slower S_2 wave data. 80

5.16 Model fit to SWS varying with brine saturation measured by Falcon-Suarez et al. (2019). 81

6.1 Azimuthal AVO responses at an interface separated by VTI shale and HTI sand for a range of Thomsen's parameters. (a) The azimuth is 0 degree; (b) The azimuth is 90 degrees. 94

6.2 The influence of fracture length to frequency-dependent anisotropy. (a) Shear-wave anisotropy as a function of frequency for various fracture sizes. The propagation is 75 degrees to the fracture normal. (b) P-wave reflectivity as a function of fracture size for various frequencies. The angle of incidence is 45 degrees and the propagation is perpendicular to fractures. 95

6.3 (a) The variation of P-P reflectivity with angle of incidence and azimuth from the top of sand for a range of Thomsen's parameters of the VTI shale; (b) The variation of reflection coefficient with angle of incidence at 0-degree azimuth; (c) The variation of reflection coefficient with angle of incidence at 90-degree azimuth; (d) The variation of reflection coefficient with azimuth at 30-degree angle; (e) The variation of reflection coefficient with azimuth at 30-degree angle. The HTI sand is frequency independent. 96

6.4 The variation of P-P reflectivity with angle of incidence and azimuth at the interface separated by VTI shale and frequency-dependent HTI sand for a range of frequencies at (a) 10 Hz (b) 50 HZ and (c) 90 Hz. 97

6.5 The frequency-dependent AVO curves and phase variations from acquisition perpendicular to fractures (zero azimuth) for (a) the isotropic shale case with $\epsilon = 0; \delta = 0$; (b) the VTI shale case with $\epsilon = 0.1; \delta = -0.1$; (c) the VTI shale case with $\epsilon = 0.1; \delta = 0.1$. 98

6.6 The pre-stack angle domain seismic traces from acquisition perpendicular to fractures (zero azimuth) for (a) the frequency-independent HTI sand overlaid by VTI shale and (b) the frequency-dependent HTI sand overlaid by VTI shale. Various Thomsen's parameters are used to characterize the VTI shale. The red line represents the location of the interface. 99

6.7 The frequency-dependent variation of top sand reflectivities and phases with azimuth at 50-degree angle of incidence for (a) the isotropic shale case with $\epsilon = 0; \delta = 0$; (b) the VTI shale case with $\epsilon = 0.1; \delta = -0.1$; (c) the VTI shale case with $\epsilon = 0.1; \delta = 0.1$. 100

6.8 The azimuth domain seismic traces from acquisition at 50-degree angle of incidence for (a) the frequency-independent HTI sand overlaid by VTI shale and (b) the frequency-dependent HTI sand overlaid by VTI shale. Various Thomsen's parameters are used to characterize the VTI shale. The first and second horizons represent the top and base sand reflections, respectively. 101

6.9 The amplitude picking of azimuth-domain seismic traces for (a) the elastic case and (b) the frequency-dependent case. The overlying VTI shale is characterized by $\epsilon = 0.1; \delta = -0.1$. The angle of incidence is 50 degrees. Curves represent the reflection coefficients. Squares represent the picked amplitudes. 101

6.10 The variation of traveltime residual with azimuth for the seismic traces shown in Figure 6.8b ($\epsilon = 0.1; \delta = -0.1$). The blue line indicates the residual for the elastic case. The red circle represents the residual for the frequency-dependent case. 102

6.11 Synthetic angle- and azimuth-domain seismic data for (a) the micro-scale crack case and (b) the meso-scale fracture case. For the angle-domain data, the acquisition is at zero azimuth. For the azimuth-domain data, the angle of incidence is fixed at 50 degrees. 104

6.12 Marginal distribution of the posterior probability for water saturation, fracture density, and fracture length, respectively. (a) The microcrack case with true fracture length 1 mm; (b) The large-scale fracture case with true fracture length 1 m. 105

6.13 The estimation of water saturation and fracture length based on the fracture density being determined as 0.05. (a) The microcrack case; (b) The large-scale fracture case. The true fracture length and water saturation is marked with white circle. 105

List of Tables

4.1 Parameters of a porous rock saturated by water and supercritical CO_2. . . 51

5.1 Common parameters for modelling experimental data used by Amalokwu et al. (2014) and this work. The use of White's mixing law is replaced with the consistent squirt-patchy model in this work. 75

5.2 Parameters used for modelling the measurements by Falcon-Suarez et al. (2019). 79

6.1 The modified Class I model of Rutherford and Williams (1989) characterized by Thomsen's parameters and the squirt-patchy model in this work. . 93

Chapter 1

Introduction

Subsurface reservoirs are made up of porous rocks with multiple fluids (e.g., oil and gas) occupying the pore space. The presence of fractures, the most abundant geological features in the Earth's crust, can significantly influence permeability and flow of fluid in a reservoir (Nelson, 2001; Narr et al., 2006). Describing fracture systems is therefore a key problem in various applications including the production of hydrocarbons and potable groundwater (Berkowitz, 2002; Engelder et al., 2009) and monitoring geological storage of CO_2 (Iding and Ringrose, 2010).

Fractures can be characterized through a range of methods, from description of outcrops, observations of core or borehole logs, to interpretation of seismic data (Liu and Martinez, 2012). A proper characterization of fractured reservoir often requires the integration of all these methods with data measured at various scales. Fractures are generally aligned by the Earth's stress field and so have the effect of introducing anisotropy in otherwise uniform media. Hence, from a geophysical perspective, the most commonly used method for fracture characterization is seismic anisotropy which quantifies the dependence of seismic attributes on the direction of wave propagation (Thomsen, 1986). Such directional dependence has a direct link to the azimuthal distribution of fractures (Tsvankin et al., 2010), and is also influenced by the properties of the saturating fluids (Mukerji and Mavko, 1994; Bandyopadhyay, 2009; Huang et al., 2015). An accurate description of fractured rocks therefore requires the understanding of fluid effects on seismic anisotropy.

In a fractured medium, perhaps the most famous phenomenon resulting from anisotropy is S-wave splitting (SWS), which occurs when a polarized S-wave enters the anisotropic medium and splits into two S-waves with orthogonal polarizations and different velocities. The faster S-wave tends to polarize along the fracture orientation, and the velocity difference between the two split waves leads to a time delay that can be measured for estimating the density of the fractures (Crampin, 1985). Measurement of SWS is often performed using Alford rotation (Alford, 1986) which transforms S-wave data into two principal sections containing the fast and slow modes. It has been successfully applied to laboratory experiments (Sondergeld and Rai, 1992) and near-offset VSP data (Lynn et al., 1999) for the detection of fractures.

Observations of SWS in the field often show a dependence on seismic wave frequency. Marson-Pidgeon and Savage (1997) observed a decrease in SWS with increasing frequency of teleseismic waves. Chesnokov et al. (2001) also presented frequency-dependent SWS in VSP data. The phenomenon that propagation velocity changes with frequency is referred to as dispersion, which is often accomplished with attenuation of the wave amplitude. Frequency-dependent anisotropy (FDA) can be caused by wave-induced fluid flow (Chapman, 2003) or scattering effects over rough fractures (Pyrak-Nolte and Nolte, 1992). Baird et al. (2013) discussed the relative importance of these effects and concluded that the most plausible explanation for FDA in seismic data is the presence of pore fluids associated with a mechanism known as 'squirt flow', which occurs when microscale fluid pressure gradients induced by variations in local pore geometry cannot be relaxed over a wave cycle (Dvorkin et al., 1995). In a fractured reservoir, it is believed that the scale length of the fractures plays a key role in affecting the squirt-related seismic dispersion (Chapman, 2003).

Increasing attention has recently been paid to the squirt effect in a fractured rock on frequency-dependent SWS that could potentially be analysed to provide information about fracture size, fluid saturation, and fluid mobility. This includes laboratory measurements of SWS in fluid saturated rocks (Tillotson et al., 2011; Amalokwu et al., 2014), fracture and fluid discriminations from field data analysis (Maultzsch et al., 2003a; Al-

Harrasi et al., 2011), and theoretical descriptions of frequency-dependent anisotropic behaviours (Chapman, 2003; Chapman et al., 2003). Apart from SWS, anisotropic P-waves have also gained enormous attention as they are of higher quality and form the majority of data acquired from seismic exploration (Lynn et al., 1995, 1999). Fracture parameters can be extracted from P-wave data through the analysis of azimuthal NMO velocity (Grechka and Tsvankin, 1998), interval traveltime (Li, 1999) and azimuthal amplitude variations (Rueger and Tsvankin, 1997). Conventionally, in a reservoir with aligned vertical fractures, P-wave reflections are known to vary with both offset and azimuth in a way that is sensitive to the orientation and density of fractures (Rüger, 1998) but insensitive to the size of fractures (Liu et al., 2000). It is therefore a challenge to discriminate between microcrack- and fault-induced anisotropy from seismic reflections. During the past decade, a lot of authors have studied the importance of dispersion on producing a frequency-dependent reflection coefficient that could potentially be analysed for the estimation of fluid saturation (Chapman et al., 2006; Odebeatu et al., 2006; Wu et al., 2014; Jin et al., 2017; Liu et al., 2018). This technique should in principle be extendible to the anisotropic case for a more accurate fracture characterization considering that fracture sizes have a controlling effect on squirt dispersion. However, no adequate attempt has been made within current literature, and the impact of saturation and fracture related dispersion on azimuthal P-wave reflections, as well as that on SWS, still appears to be poorly understood.

This is partly due to the fact that current theories of frequency-dependent anisotropy are limited to the single fluid assumption, even though almost all reservoirs are partially saturated by more than one fluid. In the absence of fractures, partial saturation effects on the isotropic medium have indeed been studied by a number of authors both theoretically and experimentally (White, 1975; Dutta and Odé, 1979; Murphy, 1982; Lebedev et al., 2009). Among these studies, it is accepted that dispersion and attenuation are highly influenced by a mechanism called ‘patchy saturation’, which occurs when unequilibrated fluid pressure due to saturation heterogeneities at a coarse scale leads to a stiffening in the elastic properties. Squirt dispersion and patchy saturation have previously been considered

separately. A recent advance by Papageorgiou and Chapman (2017) have addressed these two mechanisms in a consistent theory, which emphasises the importance of combined effects from squirt flow, patchy saturation, and relative permeability on P-wave dispersion and attenuation. In the presence of fractures, in order to improve our understanding of partial saturation effects on seismic anisotropy, Amalokwu et al. (2014) conducted ultrasonic measurements of SWS in a synthetic silica-cemented sandstone saturated by water and air. Restricted by the lack of suitable rock physics theory for describing dispersion in partially saturated fractured medium, they combined two existing models to give some insight into the measured SWS behaviours, and concluded that both patchy saturation and squirt dispersion are important for explaining saturation effects on seismic anisotropy. It is therefore of high demand to develop a theory that incorporates coupled squirt and patchy mechanisms for a convenient and accurate quantification of partial saturation effects on frequency-dependent anisotropy.

In this thesis I derive a model that calculates frequency-dependent anisotropic moduli of a fractured rock saturated with two immiscible fluids. This is done by extending the theory of Papageorgiou and Chapman (2017) to the anisotropic case where the multi-fluid flow depends not only on squirt and patchy mechanisms, but also on the relative permeability of each fluid phase according to Darcy's law. Patchy saturation is considered arising from uneven fluid pressures, which are quantified by a non-dimensional parameter that captures pore scale capillary effects. Studies of relative permeability have shown that mixed fluid can be less mobile than corresponding single phase saturation (Brooks and Corey, 1964), and this can result in a low characteristic frequency where dispersion occurs. These effects could significantly affect the behaviour of frequency-dependent anisotropy with respect to changing water saturation, with a potential prediction of unexpected non-monotonic variations of both SWS and azimuthal P-wave velocities. I test the unified theory against laboratory observations of both SWS and P-wave anisotropy in synthetic sandstones saturated by multiphase fluid systems of water/air (Amalokwu et al., 2014, 2015) and brine/CO_2 (Falcon-Suarez et al., 2019), and show that both squirt and patch mechanisms are required to explain experimental data. I also investigate the

potential use of the theory to study fluid effects on azimuthal P-wave reflections from a partially saturated reservoir, and develop a forward modelling technique that can be used to estimate fluid saturation as well as to differentiate between large-scale and micro-scale fractures.

I begin the thesis by reviewing seismic anisotropy and fundamental theories of poroelasticity. Chapter 2 introduces basic concepts of anisotropy and effective medium theories for fracture characterization. Both classic and recent advances on P- and S-wave anisotropy are reviewed. Chapter 3 begins with introducing fundamental Biot-Gassmann theory of poroelasticity for quantifying fluid saturated porous medium. Various subsequent theories incorporating velocity dispersion and attenuation are also presented, with a focus on frequency-dependent anisotropy and partial saturation effects.

In Chapter 4, I give mathematical derivation of my unified model calculating frequency-dependent anisotropy in partially saturated rock. The derivation involves solving a set of multi-fluid exchange equations modified from Darcy's law, in which the effects of patchy saturation and relative permeability are incorporated. I show that patchy saturation (quantified by a non-dimensional constant q) acts as a weighting parameter of the effective fluid bulk modulus. Fluid mobility can be significantly reduced by both patchy saturation and relative permeability, leading to stronger dispersion in partially saturated rocks compared to the fully saturated case.

Based on the derived theory, I investigate the partial saturation effects on frequency-dependent P- and S-wave anisotropies in Chapter 5. The theory predicts unexpected non-monotonic variations of SWS and azimuthal P-wave velocities with respect to changing water saturation due to the coupled effects of patchy saturation and relative permeability on lowering the fluid mobility. I also use the theory to interpret experimental data of saturation effects on frequency-dependent anisotropy measured by Amalokwu et al. (2014), Amalokwu et al. (2015) and Falcon-Suarez et al. (2019), and discuss the importance of considering both squirt and patchy mechanisms.

In Chapter 6, I study the effects of fluid and fracture induced dispersion on azimuthal P-wave reflections based on an HTI sand model overlaid by VTI shale. I show a modest

effect on the amplitude and large effect on the phase, the latter of which could be mistaken for azimuthal velocity variations. I present a Bayesian inversion based on a forward modelling technique aimed at recovering water saturation, fracture density and fracture length of the HTI sand. The results show potential of using seismic dispersion in azimuthal AVO analysis to discriminate large-scale fractures from micro-scale cracks.

Finally, I summarize the key results of this work in Chapter 7 along with a discussion and suggestions for future work.

Chapter 2

Review of seismic anisotropy

2.1 Overview

Seismic anisotropy is defined as the dependence of seismic attributes (e.g., velocity, amplitude, polarization) on the direction of wave propagation (Helbig, 1994). It arises from aligned heterogeneities at a scale smaller than seismic wavelength, and commonly exists in the subsurface with fractures, microcracks, and thin bedding of sedimentary layers (Tsvankin, 2001). The consideration of anisotropy may therefore benefit the characterization of fractures and formations of a reservoir. The link between measured seismic anisotropy and fracture properties can be established through equivalent medium theory, which considers the wavelength to be long so that the heterogeneous fractured rock can be represented as a homogeneous medium with equivalent anisotropic properties (Schoenberg, 1980; Hudson, 1980, 1981; Thomsen, 1995).

Although anisotropy widely exists in the subsurface of the earth (Crampin et al., 1984) and its theoretical foundation had been developed back to the 19th century (Green, 1848), no adequate attention was paid to the practical importance in exploration until a few decades ago. This is partly because of the complexity in describing the wave motion in anisotropic media (Helbig, 1994), and the limitation of 2D seismic surveys in the past failing to provide data with wide offset and azimuthal coverage to contain anisotropic information. It was suggested by Gupta (1974) and Crampin (1978, 1985) that the presence of parallel cracks could lead to observable anisotropic effects, from which the orientation

and density of the cracks could in principle be detected through a properly designed experiment. Their discovery turned out to be of significant importance since the cracks in a reservoir are preferentially lined up with a vertical plane, leading to azimuthal anisotropy which could become a key tool for reservoir characterization. With the developments of wider offset and azimuthal coverage of 3D surveys and applications of multi-component data (Li, 1997; Lynn et al., 1999; Gaiser et al., 2001; MacBeth, 2002; Olofsson et al., 2003; Wang et al., 2007; Hardage et al., 2011) as well as practical simplifications to complicated theory (Thomsen, 1986; Tsvankin, 1997a; Rüger, 1998) in recent years, the study of seismic anisotropy for fracture characterization has become manageable and active.

The most common model to describe anisotropy is the transverse isotropy (TI), which can be subdivided into transverse isotropy with a horizontal axis of symmetry (HTI) and transverse isotropy with a vertical axis of symmetry (VTI). HTI may describe vertical penny-shaped cracks from an isotropic background and VTI may correspond to horizontally layered formations. When the reservoir contains aligned vertical fractures, HTI is often used as the simplest model for describing azimuthal anisotropy. In the case where fractures occur in a finely layered background, e.g., natural fractures in a shale formation, it is appropriate to use a lower symmetry system called orthorhombic, which is a combination of HTI and VTI (Bakulin et al., 2000b). A more detailed description of the symmetry system is provided in section 2.3. For each symmetry class, the anisotropic medium can be explicitly represented by its stiffness matrix containing independent constants c_{ij}. Although these constants play an important role in forward modelling, it is not straightforward to associate them with seismic attributes for a practical application. Thomsen (1986) introduced an alternative notation for the TI system, which allows us to characterize the magnitude of anisotropy by using the symmetry-direction P- and S-wave velocities as well as three dimensionless parameters.

One of the most successful methods of using seismic anisotropy for fracture characterization is S-wave splitting (SWS), which occurs when a polarized S-wave splits into two S-waves with different polarizations and velocities as it propagates through an anisotropic medium. The polarization of the faster S-wave is parallel to the fractures. The velocity

difference between two split S-waves leads to a time delay which can be measured for estimating the density of the fractures (Crampin, 1985; Martin and Davis, 1987; Mueller, 1991). Although it is considered more reliable to describe fractures by using S-waves than P-waves, considerable studies depend on P-waves since they are of higher quality and are the basis of most seismic surveys (Lynn et al., 1995). A great deal of interest exists in analysing azimuthal variations of P-wave velocity and reflections in HTI media (Tsvankin, 1997b; Rüger, 1997, 1998; Grechka and Tsvankin, 1998). Techniques based on these methods will be further explained in sections 2.6 and 2.7.

2.2 Anisotropic form of Hooke's law

An anisotropic, linear elastic medium can be mathematically described through the stiffness tensor c_{ijkl}, which relates the stress σ_{ij} and strain ε_{kl} via Hooke's law:

$$\sigma_{ij} = c_{ijkl}\varepsilon_{kl} \tag{2.1}$$

where σ_{ij} denotes the elements of the stress tensor that defines the forces at an internal point of the deformable material, and ε_{kl} denotes the elements of the strain tensor that describes the corresponding distortion. The stiffness tensor c_{ijkl} consists of 81 components (fourth-rank tensor with i, j, k, l being 1, 2 or 3), the number of which are reduced to 21 because of the symmetry of stresses and strains, and a unique strain energy potential (Aki and Richards, 2002), i.e., $c_{ijkl} = c_{jikl} = c_{ijlk} = c_{jilk}$ and $c_{ijkl} = c_{klij}$.

In order to simplify the equations, the abbreviated Voigt notation is often used for the stress and strain to produce a six-element column vector rather than the nine-element matrix. The stiffness tensor is then reduced from four subscripts to two, leading to a new

form of Hooke's law (Tsvankin, 2001):

$$\begin{pmatrix} \sigma_1 \\ \sigma_2 \\ \sigma_3 \\ \sigma_4 \\ \sigma_5 \\ \sigma_6 \end{pmatrix} = \begin{pmatrix} c_{11} & c_{12} & c_{13} & c_{14} & c_{15} & c_{16} \\ c_{12} & c_{22} & c_{23} & c_{24} & c_{25} & c_{26} \\ c_{13} & c_{23} & c_{33} & c_{34} & c_{35} & c_{36} \\ c_{14} & c_{24} & c_{34} & c_{44} & c_{45} & c_{46} \\ c_{15} & c_{25} & c_{35} & c_{45} & c_{55} & c_{56} \\ c_{16} & c_{26} & c_{36} & c_{46} & c_{56} & c_{66} \end{pmatrix} \begin{pmatrix} \varepsilon_1 \\ \varepsilon_2 \\ \varepsilon_3 \\ \varepsilon_4 \\ \varepsilon_5 \\ \varepsilon_6 \end{pmatrix} \tag{2.2}$$

where the upper triangle of the Voigt stiffness matrix contains 21 constants, which correspond to the maximum number of independent components needed for describing any elastic homogeneous medium.

The number of elastic constants can be further reduced due to additional restrictions imposed by the symmetry of the medium. Isotropic materials have the highest symmetry with every plane being a plane of symmetry. Only two independent constants, namely the Lamé parameters λ and μ, are required to describe the isotropic medium. The stiffness matrix in this case has the form (Helbig, 1994)

$$\begin{pmatrix} \lambda + 2\mu & \lambda & \lambda & 0 & 0 & 0 \\ \lambda & \lambda + 2\mu & \lambda & 0 & 0 & 0 \\ \lambda & \lambda & \lambda + 2\mu & 0 & 0 & 0 \\ 0 & 0 & 0 & \mu & 0 & 0 \\ 0 & 0 & 0 & 0 & \mu & 0 \\ 0 & 0 & 0 & 0 & 0 & \mu \end{pmatrix} \tag{2.3}$$

and the original form of Hooke's law given by equation 2.1 can be simplified as

$$\sigma_{ij} = \lambda \delta_{ij} \varepsilon_{\alpha\alpha} + 2\mu \varepsilon_{ij} \tag{2.4}$$

where $\varepsilon_{\alpha\alpha}$ is the volumetric strain (sum over repeated index), and δ_{ij} is the Kronecker

parameter:

$$\delta_{ij} = \begin{cases} 1 & i = j \\ 0 & i \neq j \end{cases} . \tag{2.5}$$

At the other end, materials with lowest symmetry are called triclinic media where there is no rotational symmetry except the trivial one of 180°. A full set of 21 constants are required to describe triclinic anisotropy. Symmetry systems between these two ends include hexagonal, orthorhombic, and monoclinic anisotropies, which are characterized by specific structures of the stiffness matrix, with the number of independent elements increasing for lower symmetry systems (Tsvankin, 2001).

2.3 Anisotropic symmetry system

Hexagonal anisotropy, also known as transverse isotropy (TI), is the most common anisotropic model in exploration seismology (Tsvankin, 2001). It has a single axis of rotational symmetry. The transverse isotropy with a vertical symmetry axis (VTI), which may correspond to horizontally layered formations in figure 2.1a, is the simplest anisotropic symmetry that commonly exists in sedimentary rocks. By rotating the symmetry axis from vertical to horizontal, as illustrated in figure 2.1b, a horizontal transverse isotropy (HTI) is produced. HTI can be considered as a medium with parallel vertical penny-shaped cracks added to an isotropic background, making it the simplest model of a formation with vertical fractures (Bakulin et al., 2000a).

The stiffness matrix of a TI medium consists of 5 independent constants. For VTI

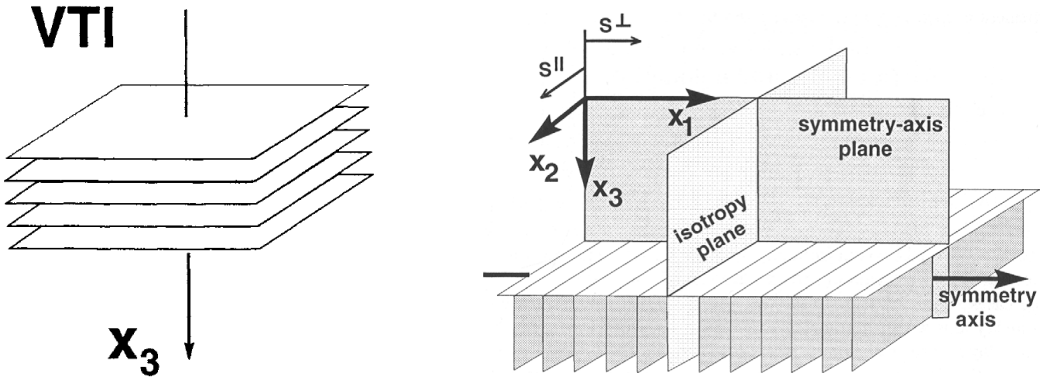

(a) (b)

Figure 2.1: (a) The VTI model; (b) The HTI model (from Tsvankin, 2001).

with the symmetry axis orients along in the x_3 axis, it has the form (Tsvankin, 2001):

$$\begin{pmatrix} c_{11} & c_{12} & c_{13} & 0 & 0 & 0 \\ c_{12} & c_{11} & c_{13} & 0 & 0 & 0 \\ c_{13} & c_{13} & c_{33} & 0 & 0 & 0 \\ 0 & 0 & 0 & c_{44} & 0 & 0 \\ 0 & 0 & 0 & 0 & c_{44} & 0 \\ 0 & 0 & 0 & 0 & 0 & c_{66} \end{pmatrix} \tag{2.6}$$

where $c_{66} = \frac{1}{2}(c_{11} - c_{12})$.

Rotating the symmetry axis from x_3 to x_1 gives the stiffness matrix of a HTI medium (Tsvankin, 2001):

$$\begin{pmatrix} c_{11} & c_{13} & c_{13} & 0 & 0 & 0 \\ c_{13} & c_{33} & c_{23} & 0 & 0 & 0 \\ c_{13} & c_{23} & c_{33} & 0 & 0 & 0 \\ 0 & 0 & 0 & c_{44} & 0 & 0 \\ 0 & 0 & 0 & 0 & c_{66} & 0 \\ 0 & 0 & 0 & 0 & 0 & c_{66} \end{pmatrix} \tag{2.7}$$

where $c_{44} = \frac{1}{2}(c_{33} - c_{23})$.

Combining the VTI and HTI leads to the orthorhombic anisotropy, which can be practically considered as a system with vertical fractures embedded in horizontally layered

formations (Bakulin et al., 2000b). Figure 2.2 displays the orthorhombic model that consists of 3 mutually orthogonal mirror planes of symmetry. Apart from the horizontal plane, the symmetry planes x_1-x_3 and x_2-x_3 are perpendicular and parallel to the strike of fractures, respectively.

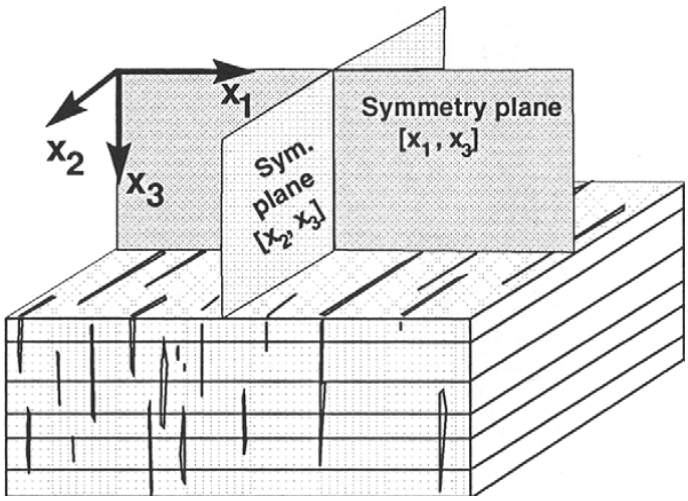

Figure 2.2: The orthorhombic anisotropy model (from Tsvankin, 2001).

Although the majority of studies on seismic anisotropy in sedimentary basins are based on the TI system (Sayers, 1994), the consideration of orthorhombic models becomes important when the media, in particular the shale formations, contain fractures that are smaller than the seismic wavelength. Aligning each of the symmetry plane with the Cartesian coordinate plane, the orthorhombic stiffness matrix can be expressed by 9 independent constants (Tsvankin, 2001):

$$\begin{pmatrix} c_{11} & c_{12} & c_{13} & 0 & 0 & 0 \\ c_{12} & c_{22} & c_{23} & 0 & 0 & 0 \\ c_{13} & c_{23} & c_{33} & 0 & 0 & 0 \\ 0 & 0 & 0 & c_{44} & 0 & 0 \\ 0 & 0 & 0 & 0 & c_{55} & 0 \\ 0 & 0 & 0 & 0 & 0 & c_{66} \end{pmatrix}. \tag{2.8}$$

Monoclinic media have only one single plane of mirror symmetry, and may represent materials containing two or more non-orthogonal sets of aligned fractures (Sayers, 1998; Bakulin et al., 2000c). In the special case of orthogonal fracture sets, the medium has

orthorhombic symmetry as described above. Up to 13 independent constants are required to characterize monoclinic anisotropy. Although the large number of parameters benefits a more accurate description, the complexity has restricted the application of such symmetry systems. As a result, most of current studies on seismic anisotropy focus on TI and orthorhombic models (Tsvankin, 2001; Liu and Martinez, 2012).

In this thesis, I base the studies of anisotropy mainly on the TI system, which supports 3 types of elastic wave modes with mutually orthogonal polarizations, i.e., the quasi-P wave whose polarization is almost in the propagation direction, the quasi S-wave whose polarization is perpendicular to the symmetry plane, and the pure S-wave whose polarization is parallel to the symmetry plane. If the wave propagate in a plane containing the symmetry axis, the phase velocities of these modes are expressed by (Tsvankin, 2001)

$$V_{qP} = \left(\frac{c_{11} \sin^2 \alpha + c_{33} \cos^2 \alpha + c_{44} + \sqrt{H}}{2\rho} \right)^{\frac{1}{2}} \tag{2.9}$$

$$V_{qS} = \left(\frac{c_{11} \sin^2 \alpha + c_{33} \cos^2 \alpha + c_{44} - \sqrt{H}}{2\rho} \right)^{\frac{1}{2}} \tag{2.10}$$

$$V_{pS} = \left(\frac{c_{66} \sin^2 \alpha + c_{44} \cos^2 \alpha}{\rho} \right)^{\frac{1}{2}} \tag{2.11}$$

where ρ is the density, α is the angle between wave propagation and the axis of symmetry (0° corresponds to propagating along the fracture normal), and the constant H is defined as

$$H = \left[(c_{11} - c_{44}) \sin^2 \alpha - (c_{33} - c_{44}) \cos^2 \alpha \right]^2 + (c_{13} + c_{44})^2 \sin^2 2\alpha. \tag{2.12}$$

2.4 Thomsen's parameters for VTI medium

Expressions of the anisotropic velocities given by equations 2.9, 2.10 and 2.11 are explicitly based on the elastic constants c_{ij}, which are too complicated to yield much insight into the anisotropic properties of the TI medium. In order to efficiently describe seismic anisotropy, Thomsen (1986) proposed an alternative notation based on the combinations of c_{ij}. Assuming a vertical axis of symmetry (VTI), the five independent elastic constants

are replaced by two vertical velocities V_{P0} and V_{S0}, and three non-dimensional parameters ϵ, δ and γ:

$$V_{P0} = \sqrt{\frac{c_{33}}{\rho}} \tag{2.13}$$

$$V_{S0} = \sqrt{\frac{c_{44}}{\rho}} \tag{2.14}$$

$$\epsilon = \frac{c_{11} - c_{33}}{2c_{33}} \tag{2.15}$$

$$\delta = \frac{(c_{13} + c_{44})^2 - (c_{33} - c_{44})^2}{2c_{33}(c_{33} - c_{44})} \tag{2.16}$$

$$\gamma = \frac{c_{66} - c_{44}}{2c_{44}}. \tag{2.17}$$

In the case of weak anisotropy, velocities of the three wave modes can be approximated using Thomsen's parameters through equations

$$V_P(\alpha) \approx V_{P0}\left(1 + \delta \sin^2\alpha \cos^2\alpha + \epsilon \sin^4\alpha\right) \tag{2.18}$$

$$V_{qS}(\alpha) \approx V_{S0}\left[1 + \left(\frac{V_{P0}}{V_{S0}}\right)^2 (\epsilon - \delta) \sin^2\alpha \cos^2\alpha\right] \tag{2.19}$$

$$V_{pS}(\alpha) \approx V_{S0}\left(1 + \gamma \sin^2\alpha\right). \tag{2.20}$$

At vertical incidence (zero degree), P-wave velocity is expressed as V_{P0} by equation 2.13, and quasi and pure S-waves have the same velocity that is defined as V_{S0}.

At horizontal incidence (90 degrees), P-wave velocity $V_P(90°)$ depends on V_{P0} and parameter ϵ through equation

$$V_P(90°) \approx V_{P0}\,(1 + \epsilon). \tag{2.21}$$

Parameter ϵ therefore defines P-wave anisotropy as it is approximately equal to the fractional difference between vertical and horizontal P-wave velocities.

Quasi and pure S-wave velocities $V_{qS}(90°)$ and $V_{pS}(90°)$ are expressed as

$$V_{qS}(90°) \approx V_{S0} \tag{2.22}$$

and

$$V_{pS}(90^\circ) \approx V_{S0}(1+\gamma). \tag{2.23}$$

Parameter γ can therefore be estimated from the fractional difference between vertical and horizontal pure S-wave velocities. It is noticed that pure S-wave has an elliptical wavefront according to equation 2.20, and γ hence represents the ellipticity of pure S-wave.

Away from vertical and horizontal directions, parameter δ begins to play a role in controlling the wavefront of quasi P-wave and quasi S-wave. Particularly, when $\delta = \epsilon$ quasi S-wave become angle independent and quasi P-wave has an elliptical wavefront with δ being its ellipticity.

In the special case where anisotropy reduces to isotropy, ϵ, δ and γ all reduce to zero.

2.5 Equivalent medium theory for fracture characterization

To build the link between anisotropic parameters and fracture properties, it is widely accepted to describe the fractured rock using the equivalent medium theory, which considers a heterogeneous medium with cracks or fractures that are much smaller than the seismic wavelength to be equivalent to a homogeneous medium which has the same overall anisotropic properties. The equivalent medium theory calculates the effective moduli or stiffness tensor of a rock in terms of the size, shape, inclusions and phases of its cracks or fractures. There are two popular types of equivalent medium approaches with different assumptions on fractures. One is the inclusion based model (Hudson, 1980, 1981) that treats the fractures or cracks as ellipsoidal voids embedded in an isotropic solid, and the other one is the linear slip model (Schoenberg, 1980; Schoenberg and Sayers, 1995) that considers fractures as planes of weakness with linear-slip boundary conditions.

Inclusion based model

The elastic response to applied stress of an ellipsoidal inclusion embedded in an infinite elastic solid has been derived by Eshelby (1957), based on which a number of equivalent medium models have been proposed to describe rocks containing 'penny-shaped' cracks (Walsh, 1965; O'Connell and Budiansky, 1974; Hudson, 1980, 1981; Xu, 1998; Chapman, 2003).

The model of Hudson (1980, 1981) has been one of the most popular models used for seismic fracture characterization both in industry and academia due to its simplicity and flexibility (Liu and Martinez, 2012). The theory assumes an elastic isotropic background medium fractured with idealized penny-shaped ellipsoidal cracks with small aspect ratio and crack density. The cracks are much smaller than the wavelength and are also isolated with respect to fluid flow. The effective moduli are expressed as

$$c_{ij}^{eff} = c_{ij}^{0} + c_{ij}^{1} + c_{ij}^{2} \tag{2.24}$$

where c_{ij}^{0} are the moduli of the isotropic background, and c_{ij}^{1} and c_{ij}^{2} are the first and second order corrections that depend on crack density, radius and aspect ratio. An important element from c_{ij}^{1} and c_{ij}^{2} is the crack density ε defined as

$$\varepsilon = \frac{N}{V}a^{3} = \frac{3\phi_{c}}{4\pi r} \tag{2.25}$$

where $\frac{N}{V}$ represents the number of cracks (N) per unit volume (V), a is the crack radius, ϕ_c is the volume fraction (porosity) of cracks, and r is the aspect ratio. Equation 2.25 demonstrates an ambiguity behind ε since the same crack density can be produced either by a medium with many small fractures or by one with a small number of large fractures. It was suggested by Cheng (1993) that the second-order correction might lead to the prediction of moduli beyond the formal limit, and better results would be obtained by using only the first-order expansion. In the case of saturated fractured rock, Hudson's model is restricted to very high frequency due to the assumption that cracks are isolated with respect to fluid flow. At low frequencies, Mavko and Mukerji (1995) suggested using Hudson's model to

calculate dry moduli and saturate them via a low-frequency approach by Brown and Korringa (1975). The validity of Hudson's model in predicting S-wave anisotropy has been tested by Ass'ad et al. (1992), which shows a good agreement between theoretical and experimental results if the crack density is low. Rathore et al. (1995) further conducted laboratory measurements of P- and S-wave anisotropy in a synthetic sandstone with controlled crack geometry. Results from the dry sample fit well with Hudson's model. In the case of saturated sample, however, Hudson's prediction severely mismatches angular variation of P-wave velocities. This can be explained by the effects of fluid transfer between cracks and the so-called equant pores (Thomsen, 1995), which are not considered in Hudson's original model. Subsequent studies by Hudson et al. (1996), Pointer et al. (2000) and Hudson et al. (2001) have included the communication of fluid between pores and cracks for a more accurate description of seismic anisotropy in fractured medium.

Linear slip model

Schoenberg (1980) introduced the linear slip model, which treats the fracture as an imperfect bonded interface between two elastic media. Across the interface, the displacement field shows discontinuity, while the stress traction remains continuous. The displacement discontinuity (or slip) is considered to be linearly related to the traction. This interface condition is the so-called linear-slip boundary condition which replaces the general condition of continuity. Based on the linear slip theory, the effective compliance (inverse of stiffness tensor) s^{eff}_{ijkl} is taken as the sum of the background compliance s^{0}_{ijkl} and an excess fracture compliance s^{1}_{ijkl}, i.e.,

$$s^{eff}_{ijkl} = s^{0}_{ijkl} + s^{1}_{ijkl} \tag{2.26}$$

from which the stiffness tensor is calculated to be

$$c^{eff}_{ijkl} = \left(s^{eff}_{ijkl}\right)^{-1}. \tag{2.27}$$

The linear slip model can be used to simulate a fracture system with a set of parallel fractures and of any anisotropy symmetry from triclinic to transversely isotropic (Schoen-

berg, 1983; Schoenberg and Douma, 1988). In the case of aligned flat microcracks, the linear slip model is consistent in form with the Hudson model, but has no formal restriction to fracture shape or small crack density. The equivalent medium theory provides direct links between fracture properties and elastic expressions of the fractured media, making it convenient to study fractures from seismic analysis.

2.6 S-wave splitting

When a polarized S-wave propagates through a TI medium, it splits into a quasi S-wave and a pure S-wave, the polarizations of which are mutually orthogonal. The velocity difference between quasi S-wave and pure S-wave leads to SWS, which can be defined as

$$SWS = \frac{V_{S_1} - V_{S_2}}{V_{S_1}} \tag{2.28}$$

where V_{S_1} is the faster S-wave velocity and V_{S_2} is the slower velocity.

Crampin (1985) investigated the role of SWS in evaluating the orientation of fractures based on synthetic modelling. Lynn and Thomsen (1986) first reported SWS in the field by observing a mis-tie at the intersection of two SH cross-sections, demonstrating that S-waves travelling with different polarizations in the vertically fractured zone have different velocities. In the presence of azimuthal anisotropy, Alford (1986) developed a rotation operator that can be used to separate two orthogonally polarized S1 and S2-waves. Martin and Davis (1987) conducted a field survey exploring the feasibility of measuring and utilizing S-wave polarization and splitting to estimate orientation and intensity of subsurface fractures. Mueller (1991) interpreted the multicomponent S-wave seismic in the Austin Chalk for the prediction of lateral fracture intensity variation. SWS has since became the focus of studies on fracture characterization, with techniques based on equivalent medium theory being powerful tools for extracting fracture properties from observed anisotropy (Liu et al., 2000).

In recent years, it has been reported that SWS observed in the field often shows a dependence on seismic frequency (Marson-Pidgeon and Savage, 1997; Chesnokov et al.,

2001; Maultzsch et al., 2003a; Liu et al., 2003; Al-Harrasi et al., 2011), which has not been accounted for in classic equivalent medium theories. Liu et al. (2003) have discussed two most likely mechanisms giving rise to frequency-dependent anisotropy, i.e., seismic scattering in media with aligned heterogeneities (Chesnokov et al., 2001) and wave-induced fluid flow in fractured rocks (Chapman, 2003). Baird et al. (2013) have investigated the relative importance of these two mechanisms in explaining frequency-dependent SWS from a microseismic dataset, suggesting that the scattering effect may only become important at high frequencies and the fluid flow appears to be the most plausible mechanism for seismic application.

A number of recent studies have considered such fluid effects on modelling FDA in fractured rocks (Hudson et al., 1996, 2001; Van der Kolk et al., 2001; Pointer et al., 2000; Chapman, 2003; Gurevich, 2003; Carcione et al., 2013; Galvin and Gurevich, 2015; Milani et al., 2016). Chapman (2003) suggested that FDA can be controlled by the fluid mobility and the size of fractures, and hence can be used to handle the main limitation of conventional effective medium theories which predict no fracture-size dependence (Chapman et al., 2003). Maultzsch et al. (2003a) and Al-Harrasi et al. (2011) have analysed frequency-dependent SWS in VSP and microseismic data respectively, demonstrating the potential use of FDA for the estimation of fracture size. SWS is also sensitive to the saturating fluid type in a fractured rock as the fluid compressibility affects S-wave propagation (Brown and Korringa, 1975). The fluid-dependence of SWS has therefore been intensively studied as a potential fluid indicator in fractured rocks (Van der Kolk et al., 2001; Qian et al., 2007; Tillotson et al., 2011; Amalokwu et al., 2014).

2.7 Azimuthal P-wave anisotropy

In seismic exploration, the variation in P-wave reflection amplitude with offset (the distance between shotpoint and receiver, or equivalently the angle of incidence) can be analysed for the detection of lithology and fluid content in rocks above and below the reflector. Such Amplitude-Versus-Offset technique is known as AVO, which is conventionally based on analytic expressions for the plane P-wave reflection coefficients at the interface

between two isotropic media (Tsvankin, 2001). Expressions for the reflection coefficients can be achieved by solving the Zoeppritz equations (Zoeppritz, 1919). In the presence of vertically aligned fractures (e.g., HTI medium), the amplitude of reflected P-wave not only depends on the angle of incidence, but also changes with the azimuthal direction of acquisition. The azimuthal variation of AVO has been practically and theoretically studied by a vast literature as a useful tool for the characterization of fracture properties (e.g., Lynn et al., 1995; Rüger, 1997; Sayers and Rickett, 1997; Rüger, 1998; Jenner, 2002; Hall and Kendall, 2003; Hunt et al., 2010; Yang et al., 2015). The explicit solution of reflection coefficient in anisotropic media as a function of incidence and azimuth angles is provided by Schoenberg and Protázio (1992).

For the convenience of practical application, it is common to approximate Zoeppritz equations as the original form is too complicated to directly give any physical insight into rock properties of interest. Shuey (1985) simplified the isotropic P-wave reflection coefficient as a function of angle of incidence θ using only two terms:

$$R_{PP}(\theta) = A + B\sin^2\theta \tag{2.29}$$

where the intercept A represents the normal-incidence reflectivity that is determined by the contrast of acoustic impedances (product of density and P-wave velocity) between upper and lower media, and the gradient B depends on the Poisson's ratio that is influenced by the pore fluid (Gregory, 1976; Domenico, 1977; Ostrander, 1984; Foster et al., 2010). AVO has therefore been used as an effective fluid indicator. It can be categorized into four classes depending on the values of A and B. Considering a gas sand encased within shale, positive A corresponds to Class I AVO where the sand has higher acoustic impedance than the encasing shale. Class II AVO has minimal impedance contrast. A is therefore close to zero and can either be positive or negative. Class III sand has lower acoustic impedance than the encasing shale, leading to a negative A value. All of the three classes have negative gradients B (Rutherford and Williams, 1989). Class IV sand also has a lower acoustic impedance (negative A), but the gradient B becomes positive in this case (Castagna and Swan, 1997).

In the presence of HTI anisotropy, Rüger (1998) gave a Shuey-style approximation to the azimuthal P-wave reflection coefficient, and found that the AVO gradient could vary as a function of the squared cosine of the azimuthal angle. The study assumes small contrasts between the elastic parameters across the interface and weak anisotropy. For small angles of incidence, the equation is written as

$$R_{PP}(\theta, \varphi) = A + \left(B^{iso} + B^{ani} \cos^2(\varphi - \varphi^{sym})\right) \sin^2 \theta \tag{2.30}$$

where φ is the azimuthal angle of acquisition, φ^{sym} is the direction of the symmetry axis plane, B^{iso} is the isotropic gradient, and B^{ani} is an anisotropic parameter that depends on Thomsen's parameters. The equation relates reflection coefficients with anisotropic parameters, providing physical insight into the AVO signatures for the interpretation of fracture density.

Schoenberg and Sayers (1995) proposed the use of 'fracture system compliance tensor' Z to describe the fracture sets. Based on their study, Sayers and Rickett (1997) numerically investigated the AVO response from a fractured gas sand reservoir encased within shale, and concluded that the azimuthal variation only become significant at large offsets. It is also suggested that fractures have the strongest azimuthal effect on the Class I model where the sand has higher acoustic impedance than the overlying shale.

Chapter 3

Review of poroelasticity

3.1 Biot-Gassmann theory of poroelasticity

Poroelasticity is known as the study of the interaction between fluid flow and solids deformation of a fluid saturated porous medium. In the field of rock physics, theories of poroelasticity link seismic responses with geological properties of interest, allowing a quantitative description of the elastic behaviour of the subsurface through models incorporating rock properties such as porosity, fractures, fluid phase and saturation. The most fundamental theory is given by Gassmann (1951), which considers that the fluid saturated porous rock consists of three components: the mineral that makes up the rock, the dry frame with connected network of pores, and the fluid that fills the pore space. The theory assumes the rock being homogeneous and the fluid within the pore space having perfect pressure communication (Wang, 2001). This would correspond to the seismic wave frequency being sufficiently low such that the fluid has enough time to flow to reach pressure equilibration. It essentially models static interaction between the fluid and solid phases, and has been widely used for estimating the impact of changing saturation on low-frequency seismic response.

Gassmann's equations describe the effect of fluid substitution on isotropic seismic properties by calculating the bulk and shear moduli of the saturated porous rock from mixing the known moduli of its three components via the following expressions (Mavko

et al., 2009):

$$K_{sat} = K_{dry} + \frac{\left(1 - \frac{K_{dry}}{K_m}\right)^2}{\frac{\phi}{K_f} + \frac{1-\phi}{K_m} - \frac{K_{dry}}{{K_m}^2}} \tag{3.1}$$

and

$$\mu_{sat} = \mu_{dry} \tag{3.2}$$

where K_{sat} is the effective bulk modulus of the saturated rock, K_{dry} is the effective bulk modulus of the dry rock frame, K_f is the fluid bulk modulus, K_m is the bulk modulus of the rock matrix, ϕ refers to porosity, and μ_{sat} and μ_{dry} are shear moduli for the saturated rock and the dry rock frame respectively. Equations 3.2 implies that the shear modulus of the saturated rock is independent of fluid.

The isotropic P-wave velocity V_P and S-wave velocity V_S can therefore be related to the moduli through

$$V_P = \sqrt{\frac{K_{sat} + \frac{4}{3}\mu_{sat}}{\rho}} \tag{3.3}$$

and

$$V_S = \sqrt{\frac{\mu_{sat}}{\rho}} \tag{3.4}$$

where ρ is density of the saturated rock.

Gassmann's theory is developed under the low frequency assumption that the stress-induced fluid pressure is equal throughout the pore space. At finite frequency, mechanism known as wave-induced fluid flow (WIFF) arises as a passing wave causes pressure gradients within the pore fluid. This results in relative motion between the solid and fluid phases until pressure equilibration is reached, leading to velocity dispersion and attenuation (Müller et al., 2010). WIFF can occur at various length scales, ranging from macroscopic scale to microscopic scale, depending on the length scale of pressure gradients.

Macroscopic flow, or global flow, results from pressure gradients between peaks and troughs of the passing wave. Velocity dispersion and attenuation at such wavelength scale has been addressed by Biot's theory of dynamic poroelasticity (Biot, 1956), which predicts frequency-dependent P- and S-wave velocities of saturated rocks based on their dry conditions. Biot (1956) defined a critical frequency f_c describing the frequency regime

where dispersion occurs as

$$f_c = \frac{\eta\phi}{2\pi\rho_f\kappa} \tag{3.5}$$

where ϕ is the porosity, κ is the rock permeability, and η and ρ_f are the viscosity and density of the fluid, respectively. For most rocks, the Biot critical frequency is about 100 KHz or higher (Müller et al., 2010). For frequencies lower than $\frac{f_c}{10}$ (White, 1983), Biot's theory is consistent with Gassmann's theory. As frequency increases, the theory predicts an increase of velocity and the existence of a second slow P-wave apart from conventional P- and S-waves. Plona (1980) and Kelder and Smeulders (1997) have successfully observed the existence of the slow P-wave, which supports the validity of Biot's theory. Shapiro et al. (2002) have investigated potential use of the slow P-wave for the estimation of permeability. A wide range of models describing velocity dispersion and attenuation in fluid saturated rocks have been derived based on Biot's theory (White, 1975; Dutta and Odé, 1979; Dutta and Seriff, 1979; Gurevich and Lopatnikov, 1995; Carcione et al., 2000; Johnson, 2001; Pride and Berryman, 2003; Müller and Gurevich, 2005; Toms et al., 2007).

Biot-Gassmann theory predicts that S-wave in saturated porous rocks always travels slower than in dry rock for that the shear modulus remains unchanged in saturated rock while the density increases (King, 2005). In an ultrasonic experiment, King (1966), however, has observed S-wave velocities in brine- and kerosene-saturated rocks higher than dry rock measurements. Most laboratory experiments (Winkler, 1985; Wang and Nur, 1990; King et al., 2000; King and Marsden, 2002) also show that Biot's theory generally underestimates the level of dispersion and attenuation. In addition, Biot's theory predicts that velocity decreases with increasing viscosity, which is in contradiction to experimental results (Jones, 1986; Batzle et al., 2006). These concerns have led to increasing attention on the importance of microscopic WIFF, or squirt flow, on an accurate explanation of velocity dispersion and attenuation.

3.2 Squirt flow

Apart from the wavelength-scale global flow, a passing wave can also create grain-scale local flow, or the so-called squirt flow as named by Mavko and Nur (1975). Squirt flow arises due to the heterogeneity of the rock's pore space, which generally consists of stiff pores and compliant microcracks. When a seismic wave squeezes such pore space, the soft cracks compress greater than the stiff pores, resulting in a local pressure gradient that drives the fluid to flow from crack to pore. In the case of low frequency, there is sufficient time for any pressure gradient to equilibrate, and the rock can be effectively described by Gassmann's theory. At high frequencies, however, the pressure gradient has insufficient time to relax, and the rock appears stiffer than it is in relaxed condition, leading to higher velocities.

In comparison to Biot's theory, the squirt mechanism predicts much higher level of dispersion and attenuation, and has been supported by laboratory measurements on fluid saturated rocks over a wide frequency range (Winkler, 1985; Sams et al., 1997; King and Marsden, 2002; Adelinet et al., 2010). The characteristic frequency of the squirt theory is derived to be proportional to the ratio of permeability over viscosity, rather than the ratio of viscosity over permeability as in the Biot critical frequency. This leads to velocities increasing with fluid viscosity which is in agreement with laboratory measurements (Jones, 1986; Batzle et al., 2006).

Various models have been proposed to account for squirt-related dispersion and attenuation in fluid saturated rocks. Mavko and Jizba (1991) derived a squirt theory that aims at calculating velocities at very high frequencies. Dvorkin et al. (1995) later extended the Mavko-Jizba model to allow the calculation of dispersion and attenuation at all frequencies. Dvorkin and Nur (1993) combined the Biot and squirt-flow mechanisms to derive a unified Biot-Squirt (BISQ) model. However, the BISQ model is not consistent with Gassmann's theory at low frequencies. Chapman et al. (2002) proposed a microstructural squirt theory that agrees with both Gassmann's equations at low frequency and the squirt-related dispersion at higher frequencies. The theory assumes an idealised microstructure consisting of soft thin cracks and stiff spherical pores. During the passage of a seismic

wave, the induced pore-scale fluid pressure gradients lead to fluid exchange between pores and cracks, as well as between cracks of different orientations. Within their approach, the effective bulk modulus K_{eff} and shear modulus μ_{eff} are calculated to be frequency dependent through equations (Jin et al., 2017):

$$\begin{aligned} K_{eff}(\omega) = \lambda + \frac{2}{3}\mu - \frac{4}{3}\varepsilon\frac{\left(\lambda+\frac{2}{3}\mu\right)^2(\lambda+2\mu)}{\mu(\lambda+\mu)} - \phi\frac{\left(\lambda+\frac{2}{3}\mu\right)(\lambda+2\mu)}{4\mu} \\ +\varepsilon\left[\frac{4\left(\lambda+\frac{2}{3}\mu\right)^2(\lambda+2\mu)}{3\mu(\lambda+\mu)} + 4\pi r\left(\lambda+\frac{2}{3}\mu\right)\right]A(\omega) \\ +\phi\frac{9\left(\lambda+\frac{2}{3}\mu\right)(\lambda+2\mu)}{4\mu}B(\omega) \end{aligned} \tag{3.6}$$

and

$$\begin{aligned} \mu_{eff}(\omega) = \mu - \frac{16}{45}\varepsilon\frac{1}{1+K_c}\frac{\mu(\lambda+2\mu)}{3\lambda+4\mu}\left(K_c + \frac{1}{1+i\omega\tau}\right) \\ -\frac{32}{45}\varepsilon\frac{\mu(\lambda+2\mu)}{3\lambda+4\mu} - \phi\frac{15\mu(\lambda+2\mu)}{9\lambda+14\mu} \end{aligned} \tag{3.7}$$

where ω is the angular frequency, μ and λ are the shear modulus and the Lamé parameter of the mineral matrix. ε is the crack density, r is the crack aspect ratio, ϕ is the total porosity, and τ is a timescale parameter that controls the frequency range of dispersion. $A(\omega)$ and $B(\omega)$ are frequency-dependent constants defined by

$$A(\omega) = \frac{\frac{i\omega\tau}{3(1+K_c)} - \gamma' i\omega\tau + \frac{1}{\gamma}(1+i\omega\gamma\tau)\left[\frac{1}{3(1+K_c)} + \gamma'\right]}{1 + i\omega\tau + \frac{1}{\gamma}(1+i\omega\gamma\tau)} \tag{3.8}$$

and

$$B(\omega) = \frac{(1+i\omega\tau)\left[\frac{1}{3(1+K_c)} + \gamma'\right] - i\omega\tau\left[\frac{1}{3(1+K_c)} - \gamma'\right]}{1 + i\omega\gamma\tau + \gamma(1+i\omega\tau)} \tag{3.9}$$

where γ and γ' are non-dimensional parameters expressed as

$$\gamma = \frac{9\phi(\lambda+\mu)\left(1+K_p\right)}{16\varepsilon(\lambda+2\mu)(1+K_c)} \tag{3.10}$$

and

$$\gamma' = \gamma \frac{\lambda + 2\mu}{(3\lambda + 2\mu)\left(1 + K_p\right)}. \tag{3.11}$$

K_c and K_p are the crack-space and pore-space compressibility parameters that are related with the fluid bulk modulus K_f through equations

$$K_c = \frac{\pi\mu\,(\lambda + \mu)\,r}{K_f\,(\lambda + 2\mu)} \tag{3.12}$$

and

$$K_p = \frac{4\mu}{3K_f}. \tag{3.13}$$

The timescale parameter τ is proportional to fluid viscosity and inversely proportional to the permeability. It therefore depends on the fluid mobility that is defined as the ratio of permeability to fluid viscosity.

The quality factor Q, which measures the rate of energy loss, for P- and S-waves can be calculated from the real and imaginary parts of the complex moduli through equations (Chapman et al., 2006)

$$Q_P = \frac{-Re\left(K_{eff} + \frac{4}{3}\mu_{eff}\right)}{Im\left(K_{eff} + \frac{4}{3}\mu_{eff}\right)} \tag{3.14}$$

and

$$Q_S = \frac{-Re\left(\mu_{eff}\right)}{Im\left(\mu_{eff}\right)}. \tag{3.15}$$

3.3 Frequency-dependent anisotropy

The consideration of WIFF within the pore space of a rock has benefited the development of rock physics theories for the description of seismic dispersion and attenuation. However, this feature was typically ignored in the classic equivalent medium theories of relating fractures to anisotropic properties (Hudson, 1981; Schoenberg, 1980; Liu et al., 2000). Abundant evidence exists that seismic anisotropy is also frequency dependent due to the effects of fluid flow in rocks containing aligned fractures (Liu et al., 2003; Maultzsch et al., 2003a; Liu et al., 2006; Al-Harrasi et al., 2011). Considerable atten-

tion has therefore been paid to relating seismic anisotropy with fluid-induced dispersion and attenuation. Thomsen (1995) recognized the importance of dispersion to the interpretation of seismic anisotropy by allowing fluid transfer between fractures and equant porosity. Later authors (e.g., Hudson et al., 1996; Pointer et al., 2000) also attempted to include WIFF into conventional inclusion-based equivalent medium theories. However, none of these theories can adequately model the variation of anisotropy with frequency at low seismic frequency range (Liu et al., 2003). Van der Kolk et al. (2001) investigated the effects of fluid on shear-wave anisotropy by developing an equivalent medium theory that takes into account squirt flow between fractures and pores. Chapman (2003) argued that the effectiveness of a frequency-dependent anisotropic theory depends not only on the fracture scale, but also on the grain-scale fluid effects which are ignored by any of the models mentioned above.

Based on the Chapman et al. (2002) poroelastic theory of grain-scale squirt flow, Chapman (2003) proposed an anisotropic model by incorporating meso-scale penny-shaped fractures and taking into account the interactions between these two scales. The model assumes an isotropic background medium with additional contributions from the pore space including spherical pores, randomly oriented ellipsoidal microcracks, and aligned ellipsoidal fractures. The pores and microcracks are isotropic and have the size identified with the grain scale, while the aligned fractures are allowed to be larger than the grain-scale (i.e., meso-scale), but are still smaller than the seismic wavelength. The resulting medium is therefore transversely isotropic. Allowing fluid exchanges within the whole pore space, the frequency-dependent stiffness tensor is of the form:

$$c_{ijkl}(\omega) = c^0_{ijkl} - \phi_p c^1_{ijkl}(\omega) - \varepsilon_c c^2_{ijkl}(\omega) - \varepsilon_f c^3_{ijkl}(\omega) \tag{3.16}$$

where c^0_{ijkl} is the isotropic elastic tensor of the background specified by the Lamé parameters λ and μ, c^1_{ijkl}, c^2_{ijkl}, and c^3_{ijkl} are corrections associated with spherical pores, microcracks, and fractures, respectively. ω is the frequency, ϕ_p is the porosity of the spherical pores, ε_c is the microcrack density, and ε_f is the fracture density. These constants depend on fluid saturation, fracture properties, and two squirt-related timescale parameters τ_m and

τ_f as defined by Chapman (2003).

The derivation of this model is based on the interaction energy approach by Eshelby (1957), which results in its restriction to low porosity. The Lamé parameters λ and μ are meant to be derived from the velocities of the mineral matrix (i.e., non-porous rock). However, in practice these moduli would have to be determined from the background velocities due to the low porosity, meaning that the substantial errors are expected to occur. To avoid such restrictions for a practical application, Chapman et al. (2003) proposed a modified version of the model by assuming that the velocities V_p^0 and V_s^0 and density ρ^0 of the unfractured porous rock at a reference frequency f^0 are known. The corresponding moduli λ^0 and μ^0 are therefore derived as

$$\lambda^0 = \left(V_p^0\right)^2 \rho^0 - 2\mu^0 \tag{3.17}$$

and

$$\mu^0 = \left(V_s^0\right)^2 \rho^0. \tag{3.18}$$

A new set of moduli Λ and Υ are then defined as

$$\Lambda = \lambda^0 + \Phi_{c,p}\left(\lambda^0, \mu^0, f^0\right) \tag{3.19}$$

and

$$\Upsilon = \mu^0 + \Phi_{c,p}\left(\lambda^0, \mu^0, f^0\right) \tag{3.20}$$

where $\Phi_{c,p}$ represents perturbations due to microcracks and pores. Both Λ and Υ can be achieved from practical measurements of V_p^0 and V_s^0, and therefore represent reference constants. The modified frequency-dependent elastic tensor is calculated as (Chapman et al., 2003)

$$c_{ijkl}(\omega) = c^0_{ijkl}(\Lambda, \Upsilon) - \phi_p c^1_{ijkl}\left(\lambda^0, \mu^0, \omega\right) - \varepsilon_c c^2_{ijkl}\left(\lambda^0, \mu^0, \omega\right) - \varepsilon_f c^3_{ijkl}\left(\lambda^0, \mu^0, \omega\right) \tag{3.21}$$

where $c^0_{ijkl}(\Lambda, \Upsilon)$ is the isotropic stiffness tensor with moduli Λ and Υ at measurement

frequency f^0. The other correction terms are consistent with those in equation 3.16, except that they are now related to the practical Lamé parameters λ^0 and μ^0 rather than the original λ and μ of the mineral matrix.

The Chapman (2003) model was extended by Chapman (2009) to the case of two meso-scale fracture sets with different orientations and connectivities. The elastic constants of these inclusion-based models were derived based on the theoretical framework of Eshelby (1957), which strictly speaking is only valid for dilute pore concentrations (low porosity) and penny-shaped fractures of finite size. Jakobsen et al. (2003) proposed a more general model using the T-matrix approach, which allows for non-dilute concentrations of fractures and pores of any size and aspect ratio. It has been numerically shown by Agersborg et al. (2007) that the Chapman (2003) model is a special case of the T-matrix approach. Jakobsen and Chapman (2009) further investigated both approaches by proposing a unified model that takes into account both Biot flow and squirt flow.

Apart from the inclusion-based effective medium theories, another commonly used approach to modelling fractures in fluid saturated porous medium is to consider the effects of fractures as a perturbation with respect to the isotropic background in the context of Biot's theory of poroelasticity (Gurevich et al., 2009). As such, one does not have to specify individual shapes of grains or pores. Brajanovski et al. (2005) proposed a theory that models fractures as very thin and highly porous layers embedded in a porous background using the Schoenberg (1980) linear-slip approach. Galvin and Gurevich (2009) proposed to model fractures as thin circular cracks (penny-shaped fractures) in a poroelastic background. Both theories allowed for WIFF between pores and fractures to account for velocity dispersion and attenuation. Brajanovski et al. (2006) analysed the frequency-dependence of P-wave attenuation based on the model of Brajanovski et al. (2005), and demonstrated that three different frequency regimes of attenuation could occur in periodically stratified media. Similar results have also been reported by Pride et al. (2004) and Müller and Rothert (2006). The Brajanovski et al. (2005) approach was also used by Carcione et al. (2013) to explicitly derive the frequency-dependent stiffness tensor of the equivalent TI medium for studying anisotropic dispersion and attenuation. A similar

method for calculating the stiffness tensor was presented by Galvin and Gurevich (2015), in which the theory of Galvin and Gurevich (2009) was employed for modelling fluid-saturated porous medium with aligned fractures.

The effective medium approaches are limited to simple geometries and non-interacting fractures, and thus WIFF between connected fractures have not been considered in any of the studies mentioned above. To overcome this problem, numerical simulations based on Biot (1941) theory of quasi-static poroelasticity have been widely applied to quantifying WIFF effects in complex fractured media. Rubino et al. (2013) and Rubino et al. (2014) emphasized the importance of WIFF in the presence of fracture connectivity through the use of a numerical upscaling procedure (Rubino et al., 2009) that allows for estimating P-wave attenuation. Quintal et al. (2014) further investigated the sensitivity of S-wave attenuation to fracture connectivity using a numerical approach presented by Quintal et al. (2011). Rubino et al. (2016) extended the approach of Rubino et al. (2009) to the case of anisotropy, and Rubino et al. (2017) have accordingly explored the potential impact of connected fractures on seismic anisotropy by demonstrating a significant reduction of both P- and S-wave anisotropies with increasing degree of fracture connectivity. The effects of intrinsic anisotropy from the background on anisotropic dispersion and attenuation of P- and S-waves have been investigated by Barbosa et al. (2017). A large number of recent papers have also employed numerical analysis to describe effective seismic properties in potentially more realistic fracture networks (Caspari et al., 2016; Barbosa et al., 2018; Hunziker et al., 2018).

Although numerical simulations can handle more complex fracture geometries, they are impractical for solving an inverse problem (Guo et al., 2017). Hence, the development of theoretical rock physics models remains an active and challenging focus for any practical application. Attempts of using frequency-dependent analysis based on effective medium theories for estimating fracture or fluid properties from seismic data have been presented by Maultzsch et al. (2003a), Liu et al. (2006), Al-Harrasi et al. (2011), Wu et al. (2014), Jin et al. (2017) and Liu et al. (2018).

3.4 Partial saturation effects

Squirt flow has traditionally been associated with single fluid saturation. However, almost all reservoirs in practice are partially saturated by two or more fluid phases. Effects of partial saturation on elastic wave properties have been studied both theoretically and experimentally throughout the years (White, 1975; Domenico, 1976; Dutta and Odé, 1979; Murphy, 1982, 1984; Knight et al., 1998; Lebedev et al., 2009; Rubino and Holliger, 2012; Tisato and Quintal, 2013; Amalokwu et al., 2014; Tisato et al., 2015; Papageorgiou and Chapman, 2015; Amalokwu et al., 2016; Papageorgiou et al., 2016; Papageorgiou and Chapman, 2017).

The quantitative description of partial saturation effects often requires the estimation of an effective bulk modulus of the multi-fluid mixture. In the case where the sand is saturated by uniformly distributed gas-brine mixture, Domenico (1976) explained laboratory measurements of P- and S-wave velocities using Gassmann's equations by assuming that the effective fluid bulk modulus K_f is the Reuss average of the constituent moduli K_w and K_g:

$$\frac{1}{K_{f,Reuss}} = \frac{S_w}{K_w} + \frac{1 - S_w}{K_g} \tag{3.22}$$

where S_w is water saturation. Equation 3.22 is also known as Wood's formula that is commonly applied for partial saturation conditions with homogeneous mixing of fluids. Later authors have constantly considered the use of Reuss average along with various rock physics theories to quantitatively characterize fluid contents in seismic exploration (e.g., Ecker et al., 1998, 2000; Han and Batzle, 2004; Wu et al., 2014; Ekanem et al., 2016; Chen and Zhang, 2017; Jin et al., 2017). A key assumption of these studies is that the fluids are uniformly mixed at a fine scale such that the pore pressure in each fluid phase has time to equilibrate during a wave cycle. This is often referred to as 'uniform saturation'.

In contrast, 'patchy saturation' occurs when unequilibrated fluid pressure due to saturation heterogeneities at a coarse scale leads to a stiffening in the elastic properties. The

scale length separating uniform and patchy saturations is given by

$$L_c \approx \sqrt{\frac{\kappa K_{fl}}{f \eta_{fl}}} \tag{3.23}$$

where f is the frequency, κ is the rock permeability, and η_{fl} and K_{fl} are the viscosity and bulk modulus of the most viscous fluid phase (Mavko and Mukerji, 1998a). Domenico (1976) showed that a heterogeneous distribution of gas-brine mixture might result in higher P-wave velocities compared to results measured at uniform saturations. Mavko and Mukerji (1998a) gave a simple patchy saturation model by using Gassmann's equations with the effective fluid modulus approximated as a Voigt average (volume-weighted) of the two fluid moduli:

$$K_{f,Voigt} = S_w K_w + (1 - S_w) K_g \tag{3.24}$$

and concluded that uniform and patchy saturations represent lower and upper bounds of seismic velocities at low frequencies.

Brie et al. (1995) introduced an empirical fluid mixing law that has been used to achieve better fits with laboratory data. Brie's law is expressed by

$$K_{f,Brie} = \left(K_w - K_g\right) {S_w}^e + K_g, \quad 1 < e < 40 \tag{3.25}$$

where e is an empirical constant that lies within $[1, 40]$.

Figure 3.1 demonstrates the effective bulk moduli of water-gas mixture calculated by the Reuss, Voigt and Brie averages. The Reuss and Voigt averages correspond to the isostress and isostrain conditions of the fluid mixture and so are the lower and upper bounds of the effective fluid moduli. For a typical empirical constant $e = 3$, Brie's law predicts that the effective fluid modulus would lie between the Voigt and Reuss bounds.

In a partially saturated rock, the unequilibrated pore pressures of saturation heterogeneities at scales larger than L_c give rise to fluid flow, leading to seismic dispersion and attenuation as seismic waves propagate through it. White (1975) quantified such frequency-dependent effects using a model consisting of spherical gas-filled pockets sur-

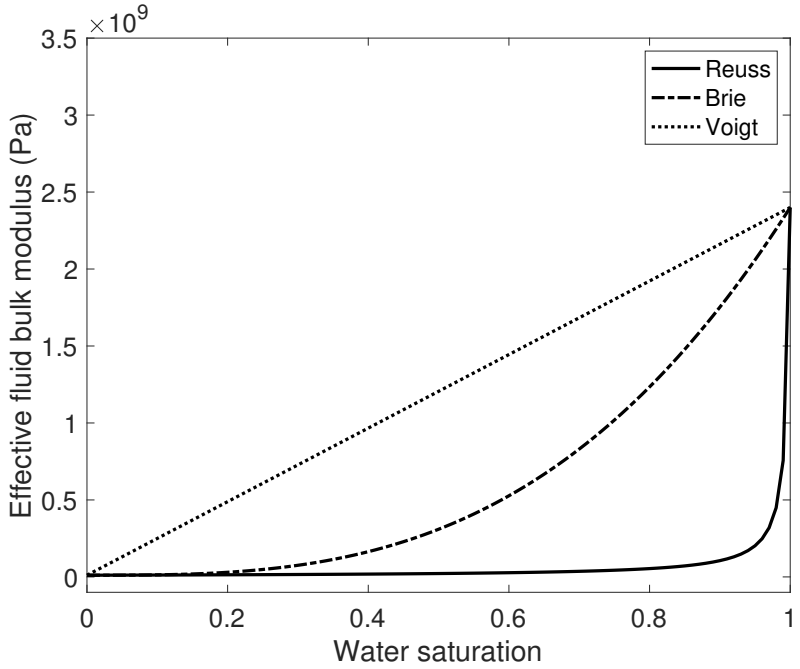

Figure 3.1: Effective bulk moduli of water-gas mixture calculated by the Reuss (equation 3.22), Voigt (equation 3.24) and Brie (equation 3.25 with $e = 3$) averages.

rounded by liquid. A number of following studies (e.g., Dutta and Odé, 1979; Dutta and Seriff, 1979; Norris, 1993; Carcione et al., 2003; Quintal et al., 2008) have discussed this 'bubble' effect on seismic wave propagation. Direct evidence of the link between measured elastic moduli and pore scale fluid distribution was provided by Lebedev et al. (2009). Patch related P- and S-wave dispersion and attenuation have been studied by Quintal et al. (2011) and Quintal et al. (2012) . A common feature of these models is that wave propagation induces a different average pressure in each of the saturating fluids.

Recently, Papageorgiou and Chapman (2017) have addressed squirt flow and patchy saturation effects in a consistent manner by deriving expressions for the bulk modulus-saturation relationships in partially saturated rocks. The theory is built on the basis of the Chapman et al. (2002) squirt model where they propose to saturate the pore space with two immiscible fluids. In the case of two immiscible fluids occupying the pore space, it is general that the pressure in one fluid phase will be different from that in the other phase. Such pressure difference across the interface between the two fluids is generally defined as capillary pressure (Wu, 2015).

Papageorgiou and Chapman (2017) proposed to use a non-dimensional parameter q to

allow for pressure variations between the saturating fluids, i.e.,

$$\Delta P_w = q\Delta P_g. \tag{3.26}$$

In contrast to the capillary pressure, which generally varies as a function of fluid saturation, the parameter q is only assumed to be a constant that quantifies fluid pressure unequilibration. Papageorgiou and Chapman (2017) suggest that it could be used to account for the so-called patchy saturation effects. The effective fluid bulk modulus K_f is derived as

$$\frac{1}{K_f} = \frac{S_w}{\tilde{q}K_w} + \frac{(1-S_w)\,q}{\tilde{q}K_g}, \quad \tilde{q} = S_w + q\,(1-S_w) \tag{3.27}$$

which is a Reuss average of the two fluid moduli K_w and K_g weighted by the patch parameter q, the value of which would affect the stiffness of the multi-fluid mixture.

The theory also adapts Darcy's law for the modelling of wave-induced fluid flow. Darcy's law states that the volumetric flux is proportionally related to the pressure gradient driving the flux via the fluid mobility, i.e.,

$$\partial_t Q_f = -A\frac{\kappa}{\eta}\partial_x P \tag{3.28}$$

where $\partial_t Q_f$ is the volumetric flow rate through cross-sectional area A, $\partial_x P$ is the fluid pressure gradient along flux direction x, and $\frac{\kappa}{\eta}$, the ratio of absolute rock permeability κ to fluid viscosity η, is defined as the fluid mobility.

When the porous rock is saturated by two immiscible fluids, Darcy's law is extended from single-phase flow to multiphase flow. The actual permeability of the porous rock should be replaced by the effective permeability to the individual fluid phase. For each fluid phase, the ratio of the effective permeability to the absolute permeability is defined as relative permeability. Although relative permeability can depend on a number of factors such as fluid saturation, wettability and pore size distribution, it is generally assumed only as a function of fluid saturation (Wu, 2015).

According to multiphase Darcy's law, the mobility of each fluid is scaled by the cor-

responding relative permeability via the following equations

$$\partial_t Q_w = -A\kappa_w \frac{\kappa}{\eta_w}\partial_x P_w; \quad \partial_t Q_g = -A\kappa_g \frac{\kappa}{\eta_g}\partial_x P_g \tag{3.29}$$

where η_w and η_g are the viscosities of water and gas, and κ_w and κ_g are the relative permeabilities of water and gas.

Considering this effect, Papageorgiou and Chapman (2017) derived the characteristic frequency ω_c in a partially saturated rock relative to its value ω_0 (given by $\frac{1}{\tau}$ in Chapman et al. (2002)) at full water saturation via

$$\frac{\omega_c}{\omega_0} = \frac{\eta_w}{\tilde{q}}\left(\frac{\kappa_w}{\eta_w} + q\frac{\kappa_g}{\eta_g}\right). \tag{3.30}$$

Papageorgiou and Chapman (2017) expressed the effective bulk modulus K_{eff} in a form similar to Chapman et al. (2002):

$$K_{eff}(\omega) = K_{dry} + 3\phi_c\left(1 + \frac{K_m}{\sigma_c}\right)K_m A(\omega) + 3\phi_p\left(1 + \frac{3K_m}{4\mu}\right)K_m B(\omega) \tag{3.31}$$

where ϕ_p is the pore porosity, ϕ_c is the crack porosity that is related with the crack density ε and aspect ratio r via $\phi_c = \frac{4}{3}\pi\varepsilon r$, and σ_c is defined by

$$\sigma_c = \frac{\pi\mu r}{2(1-\nu)} \tag{3.32}$$

where ν is the Poisson's ratio.

K_m is the mineral bulk modulus, and K_{dry} is the dry frame modulus given by

$$K_{dry} = K_m - K_m^2\left(\frac{9\phi_p}{4\mu}\frac{1-\nu}{1+\nu} + \frac{\phi_c}{\sigma_c}\right). \tag{3.33}$$

$A(\omega)$ and $B(\omega)$ are frequency-dependent constants defined as

$$A(\omega) = \frac{1 + \dfrac{i\omega\gamma}{\omega_c}}{\dfrac{3\,(1 + K_c)}{} + \gamma'}; \quad B(\omega) = \frac{\dfrac{1}{3\,(1 + K_c)} + \left(1 + \dfrac{i\omega}{\omega_c}\right)\gamma'}{1 + \left(1 + \dfrac{i\omega}{\omega_c}\right)\gamma} \tag{3.34}$$

where

$$\gamma = \frac{3\sigma_c\phi_p(1 + K_p)}{4\mu\phi_c(1 + K_c)}; \quad \gamma' = \frac{(1 - \nu)\gamma}{(1 + \nu)(1 + K_p)}. \tag{3.35}$$

Based on this theory, Papageorgiou and Chapman (2017) showed how P-wave dispersion and attenuation could be affected by patchy saturation and the relative permeability of each saturating fluid. Within current literature, however, it remains unclear what effects partial saturation would have on shear properties and frequency-dependent anisotropy, particularly on shear wave splitting which could significantly influence the characterization of fractures.

Chapter 4

Derivation of a squirt-patchy model

Abstract: In this chapter I derive a model that calculates anisotropic frequency-dependent elastic constants of a fractured rock saturated by two immiscible fluids. I do this by extending the theory of Papageorgiou and Chapman (2017) to the anisotropic case in which the fluid flow is affected by the relative mobilities of the saturating fluids. Patch effects arising from unequilibrated fluid pressures are also described by a non-dimensional parameter q which captures pore scale capillary effects. The effect of relative permeability is pronounced; fluid mobility can be lower in partially saturated rocks compared to the fully saturated case, leading to a lower characteristic frequency which could be potentially important in the seismic frequency range.

4.1 Introduction

Seismic wave propagation through fractured rocks is greatly influenced by their fracture system and fluid content. It is known that fractures can lead to frequency-dependent anisotropy, and one important mechanism accounting for such dispersion is 'squirt flow' arising from pressure gradients within the pore space of different compliances induced by passing seismic waves (Chapman, 2003). Most of current theories on frequency-dependent anisotropy have been limited to the single fluid assumption, despite the fact that almost all reservoirs are partially saturated. In the case of partial saturation, patchy saturation occurs when saturation heterogeneities at a coarse scale leads to a stiffening in

the elastic properties (Mavko and Mukerji, 1998a). Recently, Amalokwu et al. (2014) has carried out laboratory measurements of SWS in a partially saturated fractured rock, and has shown that both squirt and patchy effects are important in explaining the saturation effects on frequency-dependent anisotropy. More recently, Papageorgiou and Chapman (2017) have addressed squirt and patch effects in an isotropic theory by deriving expressions for the bulk modulus-saturation relationships in partially saturated rocks.

Within current theoretical approaches, there is a lack of suitable models describing how squirt and patch effects would affect seismic anisotropy in a partially saturated fractured rock. To address this issue, I derive frequency-dependent elastic constants of a fractured rock saturated with two immiscible fluids. Considering the effects of patchy saturation and relative permeability, I follow three steps to calculate the elastic constants of the fractured medium. First, I write a set of equations relating the fluid mass in each inclusion with the fluid pressure and the applied stress. Next, I describe the fluid mass exchange between inclusions based on Darcy's law where the relative permeability is incorporated. Solving the fluid exchange equations allows me to build a relationship between the pressure in each inclusion and the imposed stress field. Finally, I apply the equivalent medium theory to calculate the frequency-dependent elastic constants. This approach conveniently incorporates squirt flow, patchy saturation and the relative permeability effects into a unified model that allows us to study the partial saturation effects on frequency-dependent anisotropy. The elastic constants depend on the impacts of patchy saturation and the relative permeability of each fluid phase, which are responsible for lowering the characteristic frequency where dispersion occurs. Such lowering effect could lead to stronger dispersion at intermediate saturations compared to that at full saturations, which could be potentially important in the seismic frequency range.

4.2 Expression of fluid mass in an inclusion

I base the derivation on the poroelastic model of Chapman (2003), which consists of an isotropic collection of grain-scale pores and cracks with a set of meso-scale aligned fractures. Following Chapman (2003), I assume that the fracture has the same aspect ratio

as the crack. The radii of the fractures are larger than the grain size but smaller than the seismic wavelength. The cracks and pores are connected to c_1 other elements and the fractures are connected to c_2 elements. Cracks and pores are allowed to be connected with any kind of inclusion while fractures can only be connected with pores or cracks. It is also assumed that each crack or pore is connected to at most one fracture. I use superscripts $\odot$, $\ominus$ and $\dagger$ to represent pore, crack and fracture, and subscripts g and w to denote fluid types.

The fluid mass content in each inclusion can be represented by the following equations

$$m_w^{\odot} = S_w \rho_w^{\odot} \phi^{\odot}; \quad m_g^{\odot} = (1 - S_w) \rho_g^{\odot} \phi^{\odot} \tag{4.1}$$

$$m_w^{\ominus} = S_w \rho_w^{\ominus} \phi^{\ominus}; \quad m_g^{\ominus} = (1 - S_w) \rho_g^{\ominus} \phi^{\ominus} \tag{4.2}$$

$$m_w^{\dagger} = S_w \rho_w^{\dagger} \phi^{\dagger}; \quad m_g^{\dagger} = (1 - S_w) \rho_g^{\dagger} \phi^{\dagger} \tag{4.3}$$

where S_w is the saturation that is assumed equal in each inclusion. ρ_f is the fluid density which can be further estimated from its undisturbed density ρ_f^0, the fluid pressure P_f, and fluid compressibility K_f through

$$\rho_f \simeq \rho_f^0 \left(1 + \frac{P_f}{K_f}\right). \tag{4.4}$$

Assuming a unit volume of the rock, I use the void fraction (porosity) ϕ to represent the volume of each inclusion under the applied stress σ_{ii}. According to Zatsepin and Crampin (1997), these can be written as

$$\phi^{\odot} = \phi_0^{\odot} \left(1 - \frac{3(1-\nu)\sigma_{ii}}{4\mu(1+\nu)} + \frac{3P^{\odot}}{4\mu}\right) \tag{4.5}$$

$$\phi^{\ominus} = \phi_0^{\ominus} \left(1 - \frac{\sigma_i}{\sigma_c} + \frac{P^{\ominus}}{\sigma_c}\right) \tag{4.6}$$

$$\phi^{\dagger} = \phi_0^{\dagger} \left(1 - \frac{\sigma_f}{\sigma_c} + \frac{P^{\dagger}}{\sigma_c}\right) \tag{4.7}$$

where ϕ_0 is the unstressed inclusion volume, μ is the mineral shear modulus, ν is the Poisson's ratio, σ_i is the normal stress acting on the crack face, and σ_f is the normal stress

acting on the fracture face. σ_c is related to the aspect ratio r of the crack by equation

$$\sigma_c = \frac{\pi \mu r}{2\,(1-\nu)}. \tag{4.8}$$

$P^{\odot}$, $P^{\ominus}$ and $P^{\dagger}$ refer to the average pressures of the pore, crack and fracture. I also assume that the wave-induced fluid pressure may differ between the fluids in each inclusion due to capillary effects or saturation heterogeneities. Following Papageorgiou and Chapman (2017), I allow uneven fluid pressures in each inclusion by introducing a non-dimensional parameter q that proportionally relates the induced pressure of one fluid to the other, i.e.,

$$P_g = qP_w \tag{4.9}$$

where P_w and P_g represent pressures of these two fluids. It has been discussed by Papageorgiou and Chapman (2017) that q acts as a parameter that quantifies the variation of capillary pressure and should lie within $[q_0, 1]$ where $q_0 = \dfrac{K_g}{K_w}$. The fluid bulk modulus K_g is assumed to be smaller than K_w. $q = 1$ corresponds to the isostress condition in which the two fluids are mixed uniformly at a fine scale (i.e., uniform saturation). Values less than 1 represent pressure variation within fluids which could give rise to the so-called patchy saturation.

I now write the inclusion pressure as a weighted average of these two fluid pressures. Following Papageorgiou and Chapman (2017), I take water saturation as the weighting factor and give the following expressions

$$P^{\odot} = \tilde{q}P_w^{\odot}; \quad P^{\ominus} = \tilde{q}P_w^{\ominus}; \quad P^{\dagger} = \tilde{q}P_w^{\dagger} \tag{4.10}$$

where $\tilde{q} = S_w + q\,(1 - S_w)$.

By expanding equations 4.1, 4.2 and 4.3 and neglecting high order terms, I can write

the fluid mass in each inclusion in terms of the applied stress and fluid pressure as

$$\begin{aligned} m_w^{\odot} &= \frac{3}{4\mu} S_w \rho_w^0 \phi_0^{\odot} \left[\left(1 + \frac{4\mu}{3\tilde{q} K_w} \right) P^{\odot} - \frac{1-\nu}{1+\nu} \sigma_{ii} \right]; \\ m_g^{\odot} &= \frac{3}{4\mu} (1 - S_w) \rho_g^0 \phi_0^{\odot} \left[\left(1 + \frac{4\mu q}{3\tilde{q} K_g} \right) P^{\odot} - \frac{1-\nu}{1+\nu} \sigma_{ii} \right] \end{aligned} \tag{4.11}$$

$$\begin{aligned} m_w^{\ominus} &= \frac{1}{\sigma_c} S_w \rho_w^0 \phi_0^{\ominus} \left[\left(1 + \frac{\sigma_c}{\tilde{q} K_w} \right) P^{\ominus} - \sigma_i \right]; \\ m_g^{\ominus} &= \frac{1}{\sigma_c} (1 - S_w) \rho_g^0 \phi_0^{\ominus} \left[\left(1 + \frac{q\sigma_c}{\tilde{q} K_g} \right) P^{\ominus} - \sigma_i \right] \end{aligned} \tag{4.12}$$

$$\begin{aligned} m_w^{\dagger} &= \frac{1}{\sigma_c} S_w \rho_w^0 \phi_0^{\dagger} \left[\left(1 + \frac{\sigma_c}{\tilde{q} K_w} \right) P^{\dagger} - \sigma_f \right]; \\ m_g^{\dagger} &= \frac{1}{\sigma_c} (1 - S_w) \rho_g^0 \phi_0^{\dagger} \left[\left(1 + \frac{q\sigma_c}{\tilde{q} K_g} \right) P^{\dagger} - \sigma_f \right]. \end{aligned} \tag{4.13}$$

4.3 Fluid mass exchange based on Darcy's law

Darcy's law is often used to describe fluid flow. It states that the volumetric flux is proportionally related to the pressure gradient driving the flux via the fluid mobility, i.e.,

$$\partial_t Q_f = -A M_f \partial_x P \tag{4.14}$$

where $\partial_t Q_f$ is the volumetric flow rate through cross-sectional area A, $\partial_x P$ is the fluid pressure gradient along flux direction x, and M_f is the fluid mobility defined as the ratio of absolute rock permeability κ to fluid viscosity η, i.e.,

$$M_f = \frac{\kappa}{\eta}. \tag{4.15}$$

Based on equation 4.14, Chapman et al. (2002) described the single fluid mass exchange between inclusions using the following formula

$$\partial_t m^{\odot} = \frac{\rho^0}{g} (P^{\ominus} - P^{\odot}) = -\partial_t m^{\ominus} \tag{4.16}$$

by assuming that

$$\partial_t m \simeq \rho^0 \partial_t Q_f; \quad \partial_x P \simeq \frac{P_2 - P_1}{l}; \quad A \simeq l^2 \tag{4.17}$$

where l represents the length scale of the pore network. The single-fluid coefficient g is given as

$$\frac{1}{g} = l M_f. \tag{4.18}$$

Extending equation 4.16 to the anisotropic case, Chapman (2003) expressed the fluid mass exchange between grain-scale pores and cracks and meso-scale fractures using equations

$$\partial_t \left(m^{\ominus} - m^{\odot}\right) = \frac{c_1 \rho^0}{g} \left(P^{\odot} - P^{\ominus}\right); \quad \partial_t m^{\dagger} = \frac{c_2 \rho^0}{g} \left(E_P - P^{\dagger}\right) \tag{4.19}$$

where E_P is the expected pressure of the pore-crack system defined by Chapman (2003).

When the porous rock is saturated by two immiscible fluids, the mobility of each fluid is scaled by the corresponding relative permeability according to multiphase Darcy's law:

$$\partial_t Q_w = -A \kappa_w M_w \partial_x P_w; \quad \partial_t Q_g = -A \kappa_g M_g \partial_x P_g \tag{4.20}$$

where κ_w and κ_g are relative permeabilities of water and gas. M_w and M_g can be defined as the absolute mobilities of water and gas given by

$$M_w = \frac{\kappa}{\eta_w}; \quad M_g = \frac{\kappa}{\eta_g} \tag{4.21}$$

where η_w and η_g are viscosities of water and gas. The flow of each fluid would therefore depend on the effective mobility and pressure of the corresponding fluid.

The Darcy constants g_w and g_g for water and gas can then be written as

$$\frac{1}{g_w} = l \kappa_w M_w; \quad \frac{1}{g_g} = l \kappa_g M_g. \tag{4.22}$$

In an anisotropic medium, Maksimov and Dmitriev (2013) suggested that both the absolute and relative permeabilities can be anisotropic and thus a tensor representation of permeability should be employed. In this thesis, I only assume isotropic permeability for

simplicity.

I can then extend the single-fluid mass exchange equations to the two-fluid case, and describe each fluid flow between inclusions by the following equations:

$$\begin{aligned}
\partial_t \left(m_w^{\ominus} - m_w^{\odot}\right) &= \frac{c_1 \rho_w^0}{g_w} \left(P_w^{\odot} - P_w^{\ominus}\right) = \frac{c_1 \rho_w^0}{\tilde{q} g_w} \left(P^{\odot} - P^{\ominus}\right); \\
\partial_t \left(m_g^{\ominus} - m_g^{\odot}\right) &= \frac{c_1 \rho_g^0}{g_g} \left(P_g^{\odot} - P_g^{\ominus}\right) = \frac{q c_1 \rho_g^0}{\tilde{q} g_g} \left(P^{\odot} - P^{\ominus}\right); \\
\partial_t m_w^{\dagger} &= \frac{c_2 \rho_w^0}{g_w} \left(E_{P_w} - P_w^{\dagger}\right) = \frac{c_2 \rho_w^0}{\tilde{q} g_w} \left(E_P - P^{\dagger}\right); \\
\partial_t m_g^{\dagger} &= \frac{c_2 \rho_g^0}{g_g} \left(E_{P_g} - P_g^{\dagger}\right) = \frac{q c_2 \rho_g^0}{\tilde{q} g_g} \left(E_P - P^{\dagger}\right).
\end{aligned} \tag{4.23}$$

Substituting equations 4.11, 4.12 and 4.13 into euqations 4.23 yields

$$\begin{aligned}
\frac{\phi_0^{\ominus}}{\sigma_c} \partial_t \left[\left(1 + K_c\right) P^{\ominus} - \sigma_i\right] - \frac{3\phi_0^{\odot}}{4\mu} \partial_t \left[\left(1 + K_p\right) P^{\odot} - \frac{1 - \nu}{1 + \nu} \sigma_{ii}\right] &= \frac{c_1}{g} \left(P^{\odot} - P^{\ominus}\right); \\
\frac{\phi_0^{\dagger}}{\sigma_c} \partial_t \left[\left(1 + K_c\right) P^{\dagger} - \sigma_f\right] &= \frac{c_2}{g} \left(E_P - P^{\dagger}\right)
\end{aligned} \tag{4.24}$$

where K_c and K_p are related to the effective fluid compressibility K_f via

$$K_c = \frac{\sigma_c}{K_f}; \quad K_p = \frac{4\mu}{3K_f}. \tag{4.25}$$

K_f is derived as a Reuss average of the two fluid moduli weighted by q, i.e.,

$$\frac{1}{K_f} = \frac{S_w}{\tilde{q} K_w} + \frac{\left(1 - S_w\right) q}{\tilde{q} K_g}. \tag{4.26}$$

The Darcy constant $\frac{1}{g}$ given in equation 4.18 now depends on the effective mobility of the two-fluid mixture that is calculated as a weighted average of water mobility M_w and gas mobility M_g influenced by the relative permeability and the patch parameter q through the following equation

$$M_f = \frac{\kappa_w}{\tilde{q}} M_w + \frac{q \kappa_g}{\tilde{q}} M_g. \tag{4.27}$$

4.4 Solution of the elastic constants

Taking the Fourier transform of equations 4.24 and considering the conservation of mass throughout all elements, I have the solutions of pressures in each element:

$$\begin{aligned} P^{\odot}(\omega) &= D_1(\omega)\,\sigma_{ii} + D_2(\omega)\,\sigma_f; \\ P^{\ominus}(\omega) &= G_1(\omega)\,\sigma_i + G_2(\omega)\,\sigma_{ii} + G_3(\omega)\,\sigma_f; \\ P^{\dagger}(\omega) &= F_1(\omega)\,\sigma_{ii} + F_2(\omega)\,\sigma_f \end{aligned} \tag{4.28}$$

where $D_1(\omega)$, $D_2(\omega)$, $G_1(\omega)$, $G_2(\omega)$, $G_3(\omega)$, $F_1(\omega)$ and $F_2(\omega)$ are frequency-dependent parameters derived as

$$\begin{aligned} D_1 = &\left[(1-\iota)\gamma + \frac{(1-\iota)\beta}{1+\frac{i\omega}{\omega_f}} + \frac{1+\frac{i\omega\gamma}{\omega_m}}{1+\frac{i\omega}{\omega_m}}\left(\iota + \frac{\iota\beta}{1+\frac{i\omega}{\omega_f}}\right)\right]^{-1} \\ &\times\left[\frac{\iota}{3(1+K_c)} + (1-\iota)\gamma' - \frac{\frac{i\omega}{\omega_m}}{1+\frac{i\omega}{\omega_m}}\left(\frac{1}{3(1+K_c)} - \gamma'\right)\left(\iota + \frac{\iota\beta}{1+\frac{i\omega}{\omega_f}}\right)\right] \end{aligned} \tag{4.29}$$

$$D_2 = \left[(1-\iota)\gamma + \frac{(1-\iota)\beta}{1+\frac{i\omega}{\omega_f}} + \frac{1+\frac{i\omega\gamma}{\omega_m}}{1+\frac{i\omega}{\omega_m}}\left(\iota + \frac{\iota\beta}{1+\frac{i\omega}{\omega_f}}\right)\right]^{-1} \times \frac{\beta}{(1+K_c)(1+\frac{i\omega}{\omega_f})} \tag{4.30}$$

$$G_1 = \frac{\frac{i\omega}{\omega_m}}{(1+K_c)(1+\frac{i\omega}{\omega_m})} \tag{4.31}$$

$$G_2 = \frac{1+\frac{i\omega\gamma}{\omega_m}}{1+\frac{i\omega}{\omega_m}}D_1 - \frac{\frac{i\omega\gamma'}{\omega_m}}{1+\frac{i\omega}{\omega_m}} \tag{4.32}$$

$$G_3 = \frac{1+\frac{i\omega\gamma}{\omega_m}}{1+\frac{i\omega}{\omega_m}}D_2 \tag{4.33}$$

$$F_1 = \frac{1}{1+\frac{i\omega}{\omega_f}}\left[\frac{1+\frac{i\omega\gamma}{\omega_m}}{1+\frac{i\omega}{\omega_m}}\iota D_1 + (1-\iota)D_1 + \frac{\frac{i\omega\iota}{\omega_m}}{1+\frac{i\omega}{\omega_m}}\left(\frac{1}{3(1+K_c)} - \gamma'\right)\right] \tag{4.34}$$

$$F_2 = \frac{1}{1+\frac{i\omega}{\omega_f}}\left[\frac{\frac{i\omega}{\omega_f}}{1+K_c} + \frac{1+\frac{i\omega\gamma}{\omega_m}}{1+\frac{i\omega}{\omega_m}}\iota D_2 + (1-\iota)D_2\right] \tag{4.35}$$

where

$$\gamma = \frac{3\phi_0^{\odot}\sigma_c(1+K_p)}{4\mu\phi_0^{\ominus}(1+K_c)}; \quad \gamma' = \frac{(1-\nu)\gamma}{(1+\nu)(1+K_p)} \tag{4.36}$$

and

$$\iota = \frac{\phi_0^{\ominus}}{\phi_0^{\ominus} + r\phi_0^{\odot}}; \quad \beta = \frac{\iota\phi_0^{\dagger}}{\phi_0^{\ominus}}. \tag{4.37}$$

ω_m and ω_f are the micro-scale and fracture-scale characteristic frequencies given by

$$\omega_m = \frac{\omega_0 M_f}{M_w}; \quad \omega_f = \frac{\omega_0' M_f}{M_w} \tag{4.38}$$

where ω_0 and ω_0' are the values of ω_m and ω_f at full water saturation, and they are related via

$$\frac{\omega_m}{\omega_f} = \frac{\omega_0}{\omega_0'} = \frac{a_f}{\varsigma} \tag{4.39}$$

where ς is the grain size that is assumed to be identified with the radii a of the pore and cracks, and a_f is the radius of the fracture.

I further introduce notations

$$L_2 = \lambda^2 + \frac{4}{3}\lambda\mu + \frac{4}{5}\mu^2 \tag{4.40}$$

$$L_4 = \lambda^2 + \frac{4}{3}\lambda\mu + \frac{4}{15}\mu^2 \tag{4.41}$$

$$k = \lambda + \frac{2}{3}\mu. \tag{4.42}$$

With the relationship between the pressure in each inclusion and an imposed stress field being built, I can then follow Chapman (2003) to apply the interaction energy approach of Eshelby (1957) for the calculation of the effective elastic tensor. Note that the approach takes a first-order stiffness approximation and is valid for a dilute concentration of non-interacting inclusions. I use Cartesian coordinates in which the x_3 axis is aligned with the fracture normal direction. The resulting medium is therefore transversely

isotropic with vertical axis of symmetry. With the adoption of the Voigt notation, the five independent elastic constants are explicitly calculated as

$$\begin{aligned} c_{11} = (\lambda + 2\mu) - \phi_0^{\ominus}\left[\frac{L_2}{\sigma_c} + \frac{32}{15}\frac{(1-\nu)\mu}{(2-\nu)\pi r} - \left(\frac{L_2}{\sigma_c} + k\right)G_1 - \left(\frac{3k^2}{\sigma_c} + 3k\right)G_2 - \left(\frac{\lambda k}{\sigma_c} + \lambda\right)G_3\right] \\ -\phi_0^{\odot}\left[\frac{3}{4\mu}\frac{1-\nu}{1+\nu}\left(3\lambda^2 + 4\lambda\mu + \frac{36+20\nu}{7-5\nu}\mu^2\right) - \left(1 + \frac{3k}{4\mu}\right)(3kD_1 + \lambda D_2)\right] \\ -\phi_0^{\dagger}\left[\frac{\lambda^2}{\sigma_c} - 3k\left(\frac{\lambda}{\sigma_c} + 1\right)F_1 - \lambda\left(\frac{\lambda}{\sigma_c} + 1\right)F_2\right] \end{aligned} \tag{4.43}$$

$$\begin{aligned} c_{33} = (\lambda + 2\mu) - \phi_0^{\ominus}\left[\frac{L_2}{\sigma_c} + \frac{32}{15}\frac{(1-\nu)\mu}{(2-\nu)\pi r} - \left(\frac{L_2}{\sigma_c} + k\right)G_1 - \left(\frac{3k^2}{\sigma_c} + 3k\right)G_2 - \left(\frac{\lambda+2\mu}{\sigma_c}k + \lambda + 2\mu\right)G_3\right] \\ -\phi_0^{\odot}\left[\frac{3}{4\mu}\frac{1-\nu}{1+\nu}\left(3\lambda^2 + 4\lambda\mu + \frac{36+20\nu}{7-5\nu}\mu^2\right) - \left(1 + \frac{3k}{4\mu}\right)(3kD_1 + (\lambda+2\mu)D_2)\right] \\ -\phi_0^{\dagger}\left[\frac{(\lambda+2\mu)^2}{\sigma_c} - 3k\left(\frac{\lambda+2\mu}{\sigma_c} + 1\right)F_1 - (\lambda+2\mu)\left(\frac{\lambda+2\mu}{\sigma_c} + 1\right)F_2\right] \end{aligned} \tag{4.44}$$

$$c_{44} = \mu - \phi_0^{\ominus}\left[\frac{4}{15}\frac{\mu^2}{\sigma_c}(1 - G_1) + \frac{8}{5}\frac{(1-\nu)\mu}{(2-\nu)\pi r}\right] - 15\mu\phi_0^{\odot}\frac{1-\nu}{7-5\nu} - 4\mu\phi_0^{\dagger}\frac{1-\nu}{(2-\nu)\pi r} \tag{4.45}$$

$$\begin{aligned} c_{12} = \lambda - \phi_0^{\ominus}\left[\frac{L_4}{\sigma_c} - \frac{16}{15}\frac{(1-\nu)\mu}{(2-\nu)\pi r} - \left(\frac{L_4}{\sigma_c} + k\right)G_1 - \left(\frac{3k^2}{\sigma_c} + 3k\right)G_2 - \left(\frac{\lambda k}{\sigma_c} + \lambda\right)G_3\right] \\ -\phi_0^{\odot}\left[\frac{3}{4\mu}\frac{1-\nu}{1+\nu}\left(3\lambda^2 + 4\lambda\mu - \frac{4(1+5\nu)}{7-5\nu}\mu^2\right) - \left(1 + \frac{3k}{4\mu}\right)(3kD_1 + \lambda D_2)\right] \\ -\phi_0^{\dagger}\left[\frac{\lambda^2}{\sigma_c} - 3k\left(\frac{\lambda}{\sigma_c} + 1\right)F_1 - \lambda\left(\frac{\lambda}{\sigma_c} + 1\right)F_2\right] \end{aligned} \tag{4.46}$$

$$c_{13} = \lambda - \phi_0^{\ominus}\left[\frac{L_4}{\sigma_c} - \frac{16}{15}\frac{(1-\nu)\mu}{(2-\nu)\pi r} - \left(\frac{L_4}{\sigma_c} + k\right)G_1 - \left(\frac{3k^2}{\sigma_c} + 3k\right)G_2 - (\lambda+\mu)\left(\frac{k}{\sigma_c} + 1\right)G_3\right]$$
$$-\phi_0^{\odot}\left[\frac{3}{4\mu}\frac{1-\nu}{1+\nu}\left(3\lambda^2 + 4\lambda\mu - \frac{4(1+5\nu)}{7-5\nu}\mu^2\right) - \left(1 + \frac{3k}{4\mu}\right)(3kD_1 + (\lambda+\mu)D_2)\right]$$
$$-\phi_0^{\dagger}\left[\frac{\lambda(\lambda+2\mu)}{\sigma_c} - 3k\left(\frac{\lambda+\mu}{\sigma_c} + 1\right)F_1 - \left(\frac{\lambda(\lambda+2\mu)}{\sigma_c} + \lambda + \mu\right)F_2\right]. \tag{4.47}$$

c_{66} depends on c_{11} and c_{12} via

$$c_{66} = \frac{1}{2}(c_{11} - c_{12}) = \mu - \phi_0^{\ominus}\left[\frac{4}{15}\frac{\mu^2}{\sigma_c}(1 - G_1) + \frac{8}{5}\frac{(1-\nu)\mu}{(2-\nu)\pi r}\right] - 15\mu\phi_0^{\odot}\frac{1-\nu}{7-5\nu}. \tag{4.48}$$

The porosities of cracks and fractures $\phi_0^{\ominus}$, $\phi_0^{\dagger}$ can be further defined as more commonly used crack density $\varepsilon_0^{\ominus}$ and fracture density $\varepsilon_0^{\dagger}$ via the following equations:

$$\varepsilon_0^{\ominus} = \frac{N_c}{V}a^3 = \frac{3\phi_0^{\ominus}}{4\pi r}; \quad \varepsilon_0^{\dagger} = \frac{N_f}{V}{a_f}^3 = \frac{3\phi_0^{\dagger}}{4\pi r} \tag{4.49}$$

where $\frac{N_c}{V}$ and $\frac{N_c}{V}$ represent the number of cracks and fractures per unit volume.

The frequency-dependent elastic constants can be summarized in the following form:

$$c_{ij}(\omega) = c_{ij}^0 - \phi_0^{\odot}c_{ij}^1(\omega) - \varepsilon_0^{\ominus}c_{ij}^2(\omega) - \varepsilon_0^{\dagger}c_{ij}^3(\omega) \tag{4.50}$$

where c_{ij}^0 is the isotropic elastic tensor of the matrix specified by Lamé parameters λ and μ, c_{ij}^1, c_{ij}^2 and c_{ij}^3 are corrections associated with pores, microcracks and fractures, respectively, scaled by the porosity $\phi_0^{\odot}$, the crack density $\varepsilon_0^{\ominus}$ and the fracture density $\varepsilon_0^{\dagger}$.

4.5 The isotropic limit of the model

The model can be considered as an extension of previous theory to the anisotropic case, and should contain it as appropriate limits. In the absence of meso-scale fractures, fluid exchange only occurs between pores and cracks, reducing the model to the isotropic limit

that can be specified by the bulk and shear moduli. In that case, there will be no contribution from c_{ij}^3 in equation 4.50 as the fracture density $\varepsilon_0^\dagger$ can be set to zero. The bulk modulus is given by $c_{11} - \frac{4}{3}c_{44}$, which is calculated to be consistent with the one proposed by Papageorgiou and Chapman (2017), as expressed by equation 3.31.

The effective shear modulus is given by c_{44}, which is of the form

$$\mu_{eff}(\omega) = \mu - \frac{4}{15}\phi_0^\ominus \frac{1}{1+K_c}\frac{\mu^2}{\sigma_c}\left(K_c + \frac{1}{1+\dfrac{i\omega}{\omega_m}}\right) - \frac{8}{5}\phi_0^\ominus \frac{(1-\nu)\mu}{(2-\nu)\pi r} - 15\mu\phi_0^\odot \frac{1-\nu}{7-5\nu}. \quad (4.51)$$

The fluid dependence of shear modulus therefore relies on the effective mobility M_f and the effective fluid bulk modulus K_f. In the case of zero frequency, K_c and M_f cancel out and the result agrees with Gassmann's theory in which shear modulus is independent of fluid. At non-zero frequency, shear modulus would depend on both fluids through combined effects of the squirt flow mechanism, the relative permeability and the uneven fluid pressures.

4.6 Analysis of the model

In previous sections, I derive a model calculating frequency-dependent elastic constants of a fractured rock saturated by two immiscible fluids. In equation 4.50, the fracture and fluid properties are described by the frequency-dependent constants c_{ij}^1, c_{ij}^2 and c_{ij}^3, which are functions of the effective fluid bulk modulus and two characteristic frequencies associated with fluid flows taking place at grain and fracture scales respectively. The characteristic frequency (or relaxation time), which describes the frequency regime where dispersion occurs, is controlled by the length scale of the pore network and the effective fluid mobility.

Equation 4.26 suggests that the effective fluid bulk modulus K_f is a Reuss average of the two fluid moduli weighted by q, the value of which would therefore affect the stiffness of the effective fluid. The effective mobility M_f of the fluid mixture, given by equation 4.27, is a weighted average of the two fluid mobilities influenced by both q and

Table 4.1: Parameters of a porous rock saturated by water and supercritical CO_2.

Dry frame bulk modulus (Pa)	1.4×10^{10}	Dry frame shear modulus (Pa)	7.29×10^{9}
Mineral bulk modulus (Pa)	2.2×10^{10}	Mineral shear modulus (Pa)	9.31×10^{9}
Porosity	10%	Solid density (Kg/m^3)	2650
Crack density	0.02	Aspect ratio	1.0×10^{-4}
Fracture density	0.05	Fracture length (m)	0.1
Water viscosity (Pa.s)	6.0×10^{-4}	CO_2 viscosity (Pa.s)	2.1×10^{-5}
Water density (Kg/m^3)	1000	CO_2 density (Kg/m^3)	240
Water modulus (Pa)	2.4×10^{9}	CO_2modulus (Pa)	1.1×10^{7}

the relative permeability. As a result, the characteristic frequencies will not only depend on the fracture size, but also the effects of the relative permeability and uneven fluid pressures. To demonstrate such fluid effects, I consider a rock saturated by water and supercritical CO_2. The parameters given in Table 4.1, in which the bulk and shear moduli represent measurements in the absence of fractures.

Figure 4.1 shows the variation of K_f with water saturation at various values of the parameter q. As defined in equation 4.9, q lies within $[q_0, 1]$ where $q_0 = \dfrac{K_g}{K_w}$. $q = 1$ corresponds to the isostress condition in which the two fluids are mixed uniformly at a fine scale. Conditions where this isostress average is appropriate are generally referred to as uniform saturation. In this case, the effective fluid modulus given by equation 4.26 is simplified as a Reuss average

$$\frac{1}{K_f} = \frac{S_w}{K_w} + \frac{1 - S_w}{K_g} \tag{4.52}$$

which is known as the lower bound for the effective fluid.

The extreme value $q_0 = \dfrac{K_g}{K_w}$ corresponds to the isostrain condition where the effective fluid modulus now resembles the Voigt average

$$K_f = S_w K_w + (1 - S_w) K_g \tag{4.53}$$

which is generally referred to as the Voigt approximation to the patchy-saturation upper bound (Mavko and Mukerji, 1998a).

The theory conveniently expresses both lower (Reuss) and upper (Voigt) bounds of the effective fluid moduli via a single parameter q. Any q value between q_0 and 1 can

therefore be used to represent pressure variation within fluids which could give rise to patchy saturation effects. The results predicted by equation 4.26 are also similar to Brie's law as discussed by Papageorgiou et al. (2016).

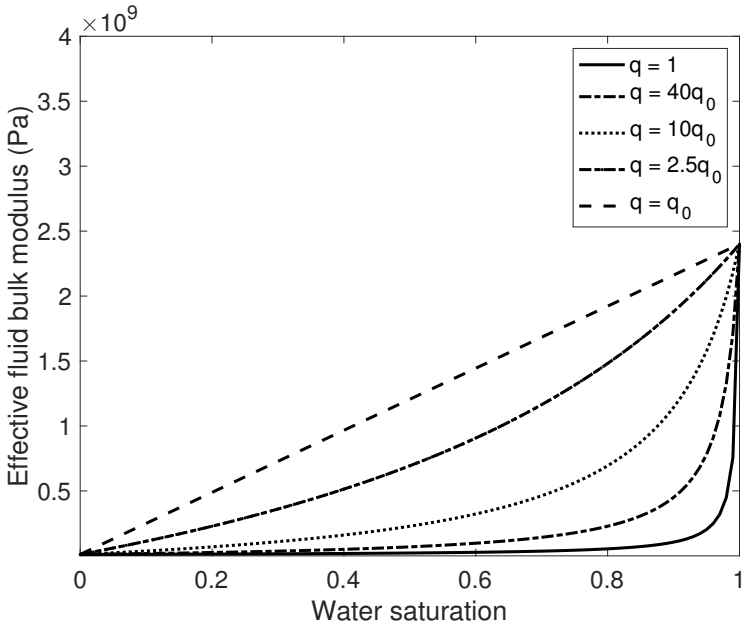

Figure 4.1: The variation of the effective fluid bulk modulus K_f, predicted by equation 4.26, with water saturation for various values of q.

My calculation shows that, in a partially saturated fractured rock, the grain-scale squirt frequency ω_m and the fracture-scale characteristic frequency ω_f are given by equation 4.38, which allows us to relate the multi-fluid characteristic frequencies with their values at full saturation. ω_m and ω_f also depend on the effective fluid mobility M_f that are affected by both patchy saturation and relative permeability according to equation 4.27. We should therefore expect a more complicated squirt flow behaviour than the singe fluid scenario.

The relative permeability of each fluid phase is often assumed as an increasing function of its saturation. From the perspective of conventional effective fluid approach (e.g., Amalokwu et al., 2014), the fluid mobility is simply averaged through an effective viscosity according to

$$M_f = \frac{1}{\tilde{q}} S_w M_w + \frac{q}{\tilde{q}} (1 - S_w) M_g \tag{4.54}$$

which leads to a linear relationship between relative permeability and fluid saturation:

$$\kappa_w = S_w; \quad \kappa_g = 1 - S_w. \tag{4.55}$$

Results from multi-phase flow in CO_2 storage reservoirs (Benson et al., 2013) show much lower values compared to such linear expression. Various relative permeability models have been proposed to explain laboratory measurements (e.g., Brooks-Corey model). In this section I seek the simplest model by considering the relative permeability as a symmetric power function of fluid saturation:

$$\kappa_w = S_w^n; \quad \kappa_g = (1 - S_w)^n \tag{4.56}$$

where the exponent n is no less than one.

Figures 4.2a and 4.2b show the curves for relative permeabilities of water and gas under various values of n. The corresponding characteristic frequencies are plotted against water saturation in Figure 4.3 where q is assumed to be $10q_0$. Taking the example of $n = 3$, the effect of q on the variation of characteristic frequency with water saturation is displayed in Figure 4.4.

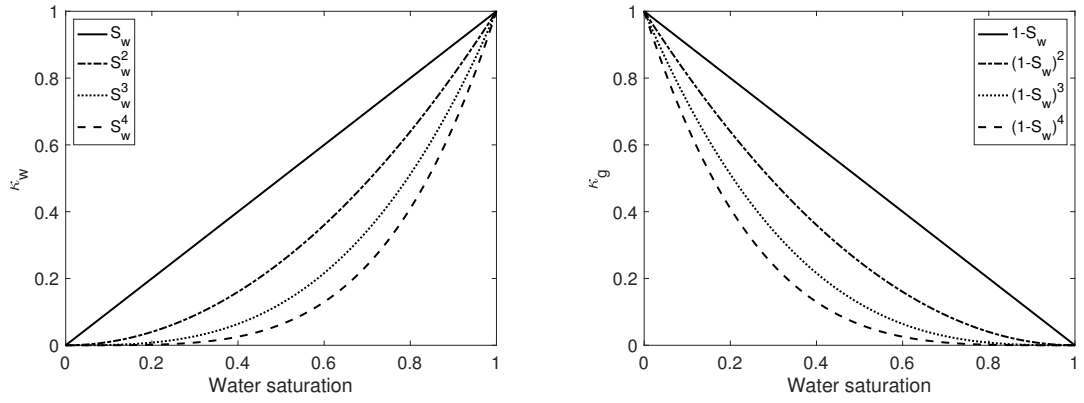

(a) (b)

Figure 4.2: The relative permeability model $\kappa_w = S_w^n; \kappa_g = (1 - S_w)^n$ under various values of n.

The difference between the grain-scale ω_m and the fracture-scale ω_f is dominated by the fracture size according to equation 4.39, which suggests that the ratio of these two

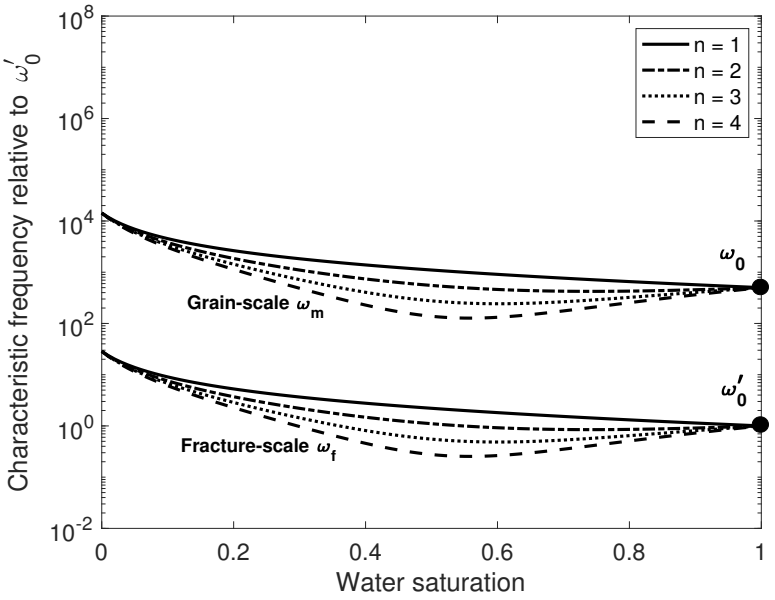

Figure 4.3: The variation of the grain-scale characteristic frequency ω_m and the fracture-scale characteristic frequency ω_f with water saturation for various values of n. The patch parameter q is assumed to be $10q_0$.

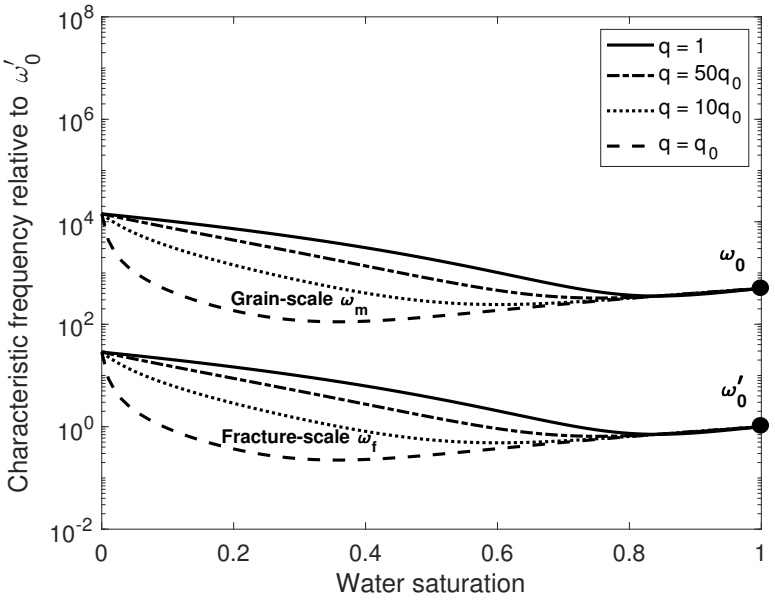

Figure 4.4: The variation of the grain-scale characteristic frequency ω_m and the fracture-scale characteristic frequency ω_f with water saturation for various values of the patch parameter q. The relative permeability model is chosen as $\kappa_w = S_w^3; \kappa_g = (1 - S_w)^3$.

frequencies $\frac{\omega_m}{\omega_f}$ stands for the fracture length normalized by the grain size, i.e., $\frac{a_f}{\varsigma}$. Since a_f is assumed to be larger than ς, the fracture related ω_f is smaller than the microcrack related ω_m. Possible physical explanation behind this is that for a larger fracture scale, one would expect relatively more fluid volume to move in and out of the fracture to reach pres-

sure equilibration, which requires more time and therefore leads to lower characteristic frequency.

In comparison to the single fluid case, the characteristic frequency in a partially saturated rock now depends on water saturation, the fluid patchiness and relative permeabilities through the effective mobility M_f. According to equation 4.38, a lower mobility proportionally leads to a lower characteristic frequency. This can be understood that fluids with lower mobility flow more slowly and would therefore require more time for the pressure gradients to relax, which in turn results in a lower characteristic frequency. Equation 4.27 shows that M_f is affected by the effects of relative permeability and patchy saturation, which tend to lower the characteristic frequency at intermediate saturations, leading to a value lower than the full saturation case as illustrated by Figures 4.3 and 4.4. This lowering effect would affect the variation of moduli with water saturation at a given frequency, complicating the behaviour of velocity dispersion in the partially saturated medium. In this model, both the two-fluid mixture and the fractures contribute to lowering the characteristic frequency, which could potentially lead to frequency-dependent anisotropy in the seismic frequency band.

4.7 Conclusion

In this chapter I derive expressions for the anisotropic frequency-dependent elastic constants in a fractured rock saturated by two immiscible fluids. These depend on the relative mobilities of the saturating fluids and the coupled impact of squirt and patch effects, which have typically been considered independently, on anisotropic seismic wave propagation. The effective fluid modulus is a Reuss average of the two fluid moduli weighted by the patch parameter q, the value of which would affect the stiffness of the two-fluid mixture. The effect of relative permeability is pronounced; fluid mobility can be lower in partially saturated rocks compared to the fully saturated case, and this can result in a lower characteristic frequency which could potentially lead to frequency-dependent anisotropy in the seismic frequency band.

Chapter 5

Partial saturation effects on frequency-dependent anisotropy

Abstract: In this chapter I use the squirt-patchy theory derived in Chapter 4 to examine the coupled patch and squirt effects on both P- and S-wave anisotropies in a fractured rock saturated with two immiscible fluids. I show non-monotonic variations of SWS and P-wave velocities with changing water saturation. This is due to the effects of relative permeability and patchy saturation on lowering the characteristic frequency at intermediate saturations, and may complicate attempts to invert fluid content from seismic data. While the squirt and patch effects on shear properties are weaker than that on bulk properties, the impact on SWS in fractured rocks is potentially significant. I use the theory to model recent experimental measurements of P- and S-wave anisotropies in partially saturated rocks, and conclude that both squirt and patch mechanisms are required for the analysis of saturation effects on frequency-dependent anisotropy.

5.1 Introduction

Frequency-dependent anisotropy has been widely used for characterizing the fractures in a reservoir. In Chapter 4, I have derived a theory that calculates frequency-dependent elastic constants in a fractured rock saturated by two immiscible fluids. The model incorporates combined effects of squirt flow, patchy saturation and relative permeabilities,

which jointly affect both effective bulk modulus and mobility of the two-fluid mixture in a complicated way. As a result, the characteristic frequency in partially saturated rock can be reduced to a value lower than that in full saturation case. Such effects could significantly affect the behaviours of frequency-dependent P- and S-wave anisotropies, which are to be investigated in this chapter.

Previously, Amalokwu et al. (2014) and Amalokwu et al. (2015) experimentally measured the water/air saturation effects on SWS and P-wave anisotropy. Due to the lack of suitable frequency-dependent anisotropic theory for elastic wave velocities in partially saturated rock, they combined two models together to give some insight into the possible mechanisms causing the observed results. In this chapter, I intend to test the derived theory against their laboratory data as well as new measurements on a brine/CO_2 saturated rock from Falcon-Suarez et al. (2019).

I organize the chapter as follows. I first briefly review the model derived in Chapter 4 for describing frequency-dependent anisotropy in a partially saturated rock. Based on the model, I carry out numerical studies to demonstrate the multi-fluid effects on the variation of frequency-dependent P- and S-wave anisotropy with water saturation. Finally, I use the model to explain laboratory data, and emphasise the requirement to include coupled squirt and patch mechanisms for the interpretation of saturation effects on frequency-dependent anisotropy.

5.2 Theory and methods

The model derived in Chapter 4 calculates anisotropic frequency-dependent elastic constants of a partially saturated fractured rock. The theory assumes a pore space consisting of an isotropic collection of grain-scale pores and cracks and a set of aligned meso-scale fractures. The radii of the fractures are larger than the grain size but smaller than the seismic wavelength. Assuming that the fracture normal direction is aligned with x_3-axis in the Cartesian coordinates, the resulting medium is transversely isotropic with vertical axis of symmetry (VTI). The theory assumes that the fractured rock is partially saturated with two immiscible fluids. During the passage of a seismic wave, squirt flow arises from

fluid pressure gradients between the inclusions with different compliances. Such fluid flow is affected by the relative mobilities of the saturating fluids. Within each inclusion, a non-dimensional parameter q is also used to quantify the unequilibrated fluid pressures that account for the so-called patchy saturation effects. Considering these effects, the anisotropic elastic constants are summarized by equation 4.50, which is a function of frequency-dependent elements associated with pores, cracks and fractures. The partial saturation effects depend on the effective bulk modulus of the two-fluid mixture (K_f by equation 4.26), the stiffness of which is affected by patchy saturation through the patch parameter q. Squirt flow in this model is described by two characteristic frequencies corresponding to grain-scale microcracks and meso-scale fractures (ω_m and ω_f by equation 4.38), which are proportionally related with the effective fluid mobility M_f that is influenced by the relative permeability and the patch parameter q.

Based on this theory, I study the effect of patchy saturation and squirt dispersion on wave propagation by considering a porous rock saturated by water and supercritical CO_2. Table 4.1 shows the parameters. The relative permeability model is approximated as

$$\kappa_w = S_w^3; \quad \kappa_{CO_2} = (1 - S_w)^2 \tag{5.1}$$

which largely fits the curves given by Benson et al. (2013) for brine-CO_2 saturated reservoirs. Two cases are investigated: the absence of fractures and the presence of fractures.

In the absence of meso-scale fractures, the grain-scale pores and randomly oriented cracks lead to an isotropic effective medium that can be specified by the bulk and shear moduli. In that case, Papageorgiou and Chapman (2017) have studied the partial saturation effects on P-wave velocity dispersion and attenuation. The S-wave velocity dispersion and attenuation can be calculated using

$$\frac{\rho}{\mu_{eff}(\omega)} = \frac{1}{V_S^2} + i\frac{1}{Q_S V_S^2} \tag{5.2}$$

where the shear modulus $\mu_{eff}(\omega)$ is given by equation 4.51, V_S and $1/Q_S$ are the S-wave velocity and attenuation at various frequencies ω relative to the grain-scale characteristic

frequency ω_o at full water saturation.

In the presence of aligned fractures, SWS occurs when a polarized S-wave splits into a quasi S-wave and a pure S-wave as it propagates through the TI medium. In this study SWS is quantified by $(V_{S_1} - V_{S_2})/V_{S_1}$ where V_{S_1} is the faster S-wave velocity and V_{S_2} is the slower velocity as expressed by equations 2.10 and 2.11. P-wave velocity also depends on the angle of propagation through equation 2.9.

5.3 Numerical example- the absence of fractures

In the absence of fractures, Papageorgiou and Chapman (2017) have studied squirt-patchy effects on P-wave dispersion and attenuation. Here I study these effects on shear properties. I first investigate the variation of shear moduli with water saturation for a range of the patch parameters q and frequencies in Figure 5.1. In the case of zero frequency (Figure 5.1b), the model agrees with Gassmann's theory which shows no dependence of shear modulus on fluid. At non-zero frequencies, shear modulus depends on fluid saturation and the patch parameter q. Since water has a higher bulk modulus and viscosity than gas, the effective fluid approach might expect increasing water saturation to lead to a stiffening effect for water-CO_2 mixtures. The results in Figure 5.1d suggest that this may not be true as I predict a non-monotonic variation of shear modulus with water saturation. This is due to the relative permeability effect that leads to a decrease in fluid mobility and a higher shear modulus for intermediate water saturations.

Figures 5.2 and 5.3 show the corresponding variations of S-wave velocities and attenuation with water saturation. S-wave velocities are seen to increase with frequency, while the maximum attenuation could occur at intermediate frequency. At zero frequency in Figure 5.2b, the results agree with Gassmann's theory in that S-wave velocity only decreases with water saturation due to the density effect and no attenuation is predicted (Figure 5.3b). This is consistent with Mavko and Mukerji (1998) where patchy saturation shows no effect on S-waves at low frequencies. At non-zero frequencies, patchy saturation could become important. For high (e.g., $100\omega_0$ in Figure 5.2f) frequencies, S-wave velocities at various values of q are slightly separated. For intermediate frequencies (e.g.,

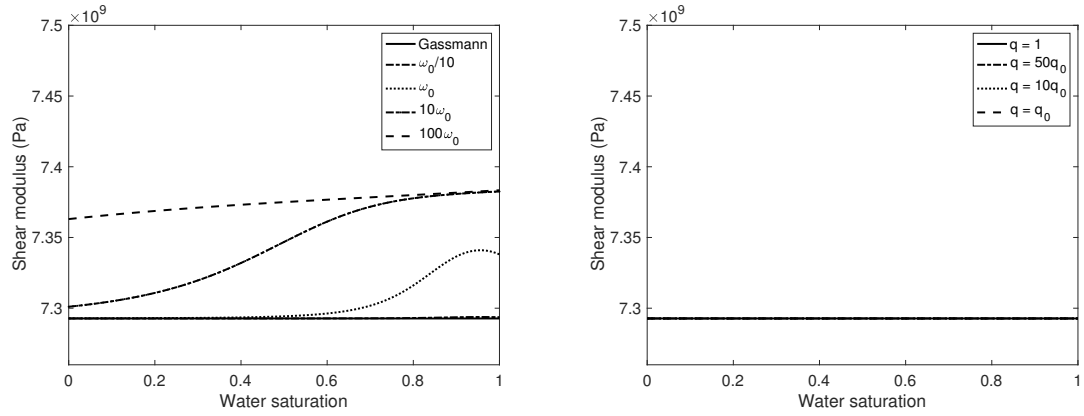

(a) $q = 1$ (b) $\omega = 0$

(c) $q = 10q_0$ (d) $\omega = \omega_0$

(e) $q = q_0$ (f) $\omega = 100\omega_0$

Figure 5.1: The variation of shear modulus with water saturation for a range of frequencies and the patch parameters q in the absence of fractures.

ω_0 in Figures 5.2d and 5.3d), the fluid dependence of S-wave velocity is clearly affected by q, and multiple attenuation peaks can be observed at various water saturations. I also notice that the dispersion and attenuation of S-wave is much weaker than that of P-wave compared to the values shown by Papageorgiou and Chapman (2017).

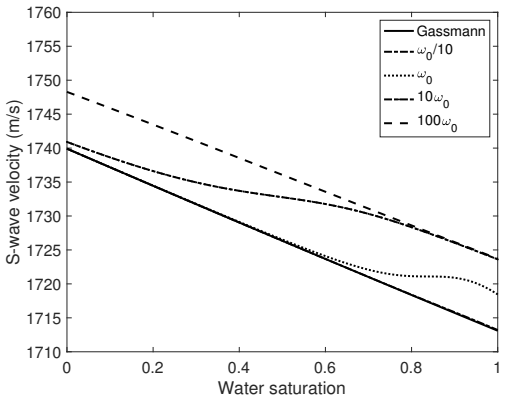

(a) $q = 1$

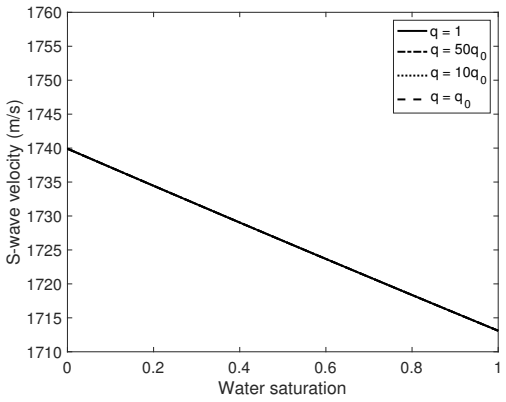

(b) $\omega = 0$

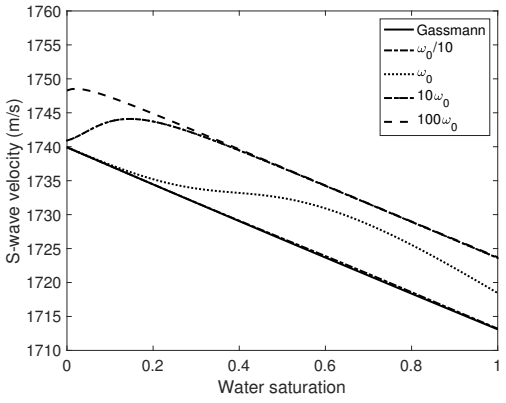

(c) $q = 10q_0$

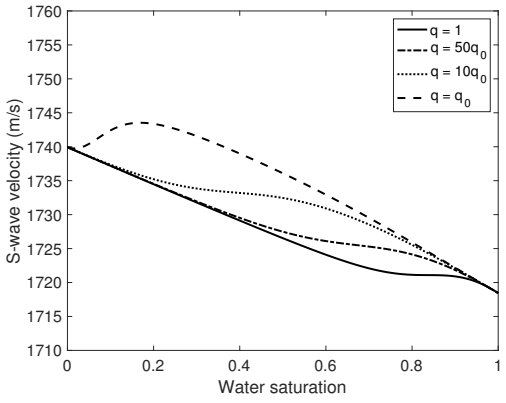

(d) $\omega = \omega_0$

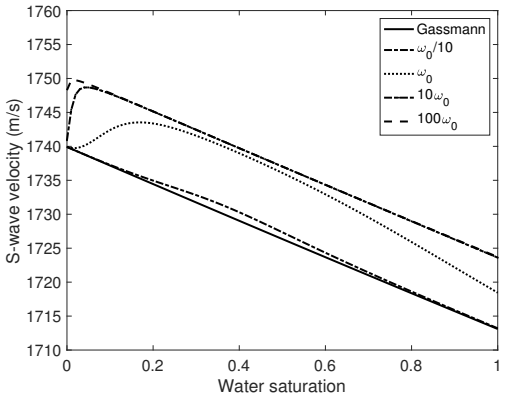

(e) $q = q_0$

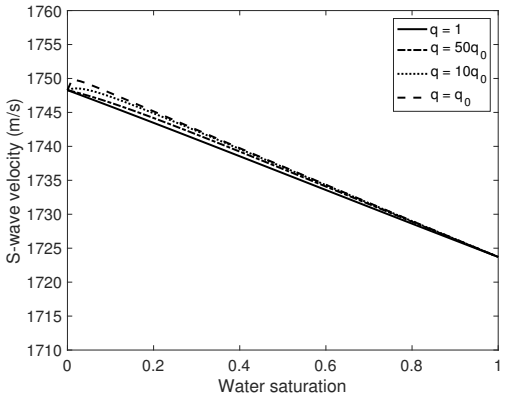

(f) $\omega = 100\omega_0$

Figure 5.2: The variation of S-wave velocity with water saturation for a range of frequencies and the patch parameters q in the absence of fractures.

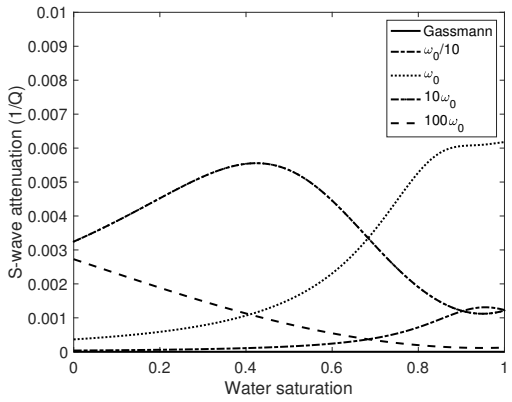

(a) $q = 1$

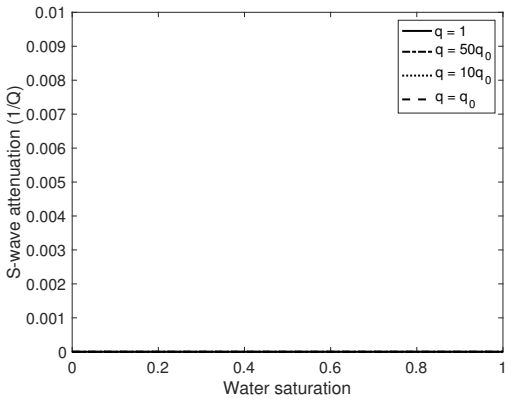

(b) $\omega = 0$

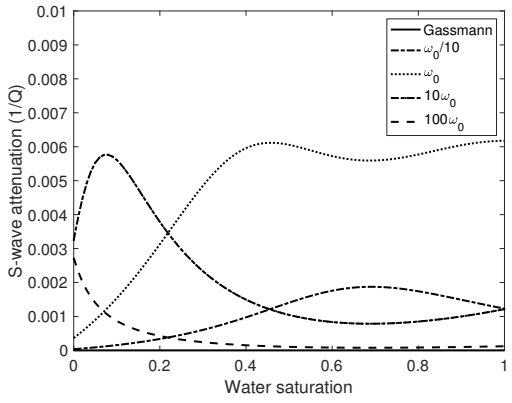

(c) $q = 10q_0$

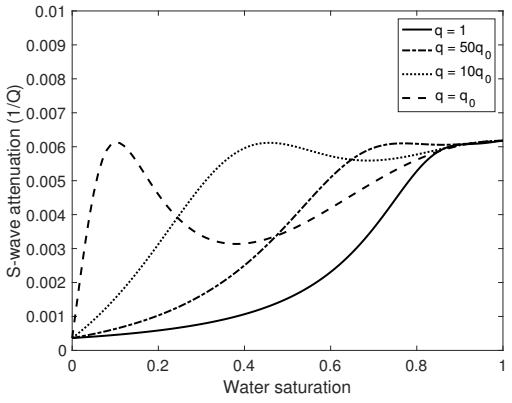

(d) $\omega = \omega_0$

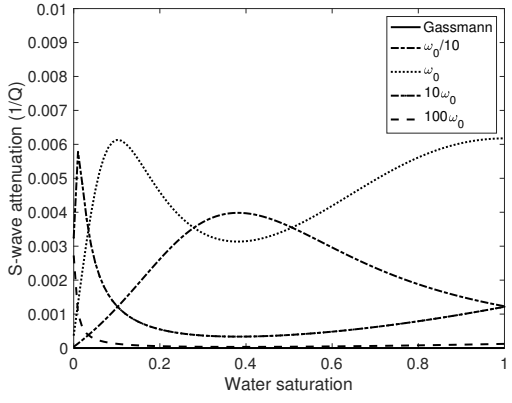

(e) $q = q_0$

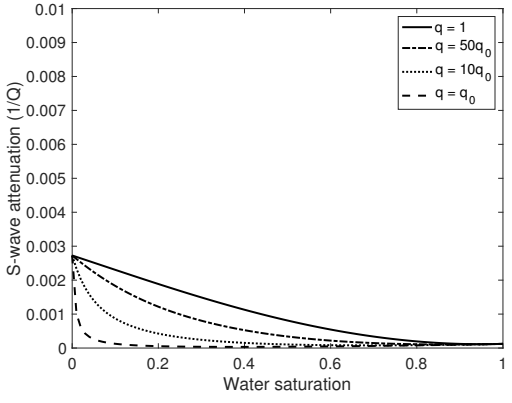

(f) $\omega = 100\omega_0$

Figure 5.3: The variation of S-wave attenuation with water saturation for a range of frequencies and the patch parameters q in the absence of fractures.

5.4 Numerical example- the presence of fractures

In the presence of aligned meso-scale fractures, the medium is expected to show frequency-dependent anisotropy. I now introduce a set of fractures with density 0.05 and length 10 cm. According to equation 4.39, the fracture related reference frequency ω_0' is much lower than ω_0 since the fracture length a_f is supposed to be much larger than the grain size ς. Therefore, in the anisotropic case I proceed the numerical analysis by using frequencies relative to ω_0'.

5.4.1 Saturation effects on S-wave anisotropy

Since quasi S-wave and pure S-wave travels at different velocities, S-wave splitting occurs when a polarized S-wave propagates through a TI medium. Figure 5.4 shows the variation of SWS with water saturation for a range of parameters q and frequencies. Propagation is at 70 degrees to the fracture normal. It is clear that SWS decreases with the increase of frequency. In the isotropic case (Figure 5.1b), I show that the shear modulus is unaffected by fluid at zero frequency. This is no longer the case for the anisotropic case where evident dependence of SWS on water saturation and the patch parameter q can be observed even at zero frequency (Figure 5.4b). Such fluid dependence arises from the compressibility effect of the water-CO_2 mixture as the Quasi-shear wave compresses the fractures. The magnitude of SWS also decreases with the increasing patchiness of two immiscible fluids. At zero frequency (Figure 5.4b), the uniform saturation case (i.e., $q = 1$) shows an abrupt drop of SWS as it approaches full water saturation. This may no longer be observed in the patchy saturation case since the variation curves could become smooth. At very high frequencies (e.g., $100\omega_0'$ Figure 5.4f), the results are reversed as the abrupt change occurs for the patchy saturation case near full CO_2 saturation. At intermediate frequencies (e.g., ω_0' Figure 5.4d), I show observable non-monotonic behaviour of SWS with respect to changes in water saturation. While SWS generally decreases with water saturation, it may start to increase with water saturation due to the impact of relative permeability and patch effects on lowering the characteristic frequency.

Figure 5.5 shows the variation of SWS with frequencies at different water saturations.

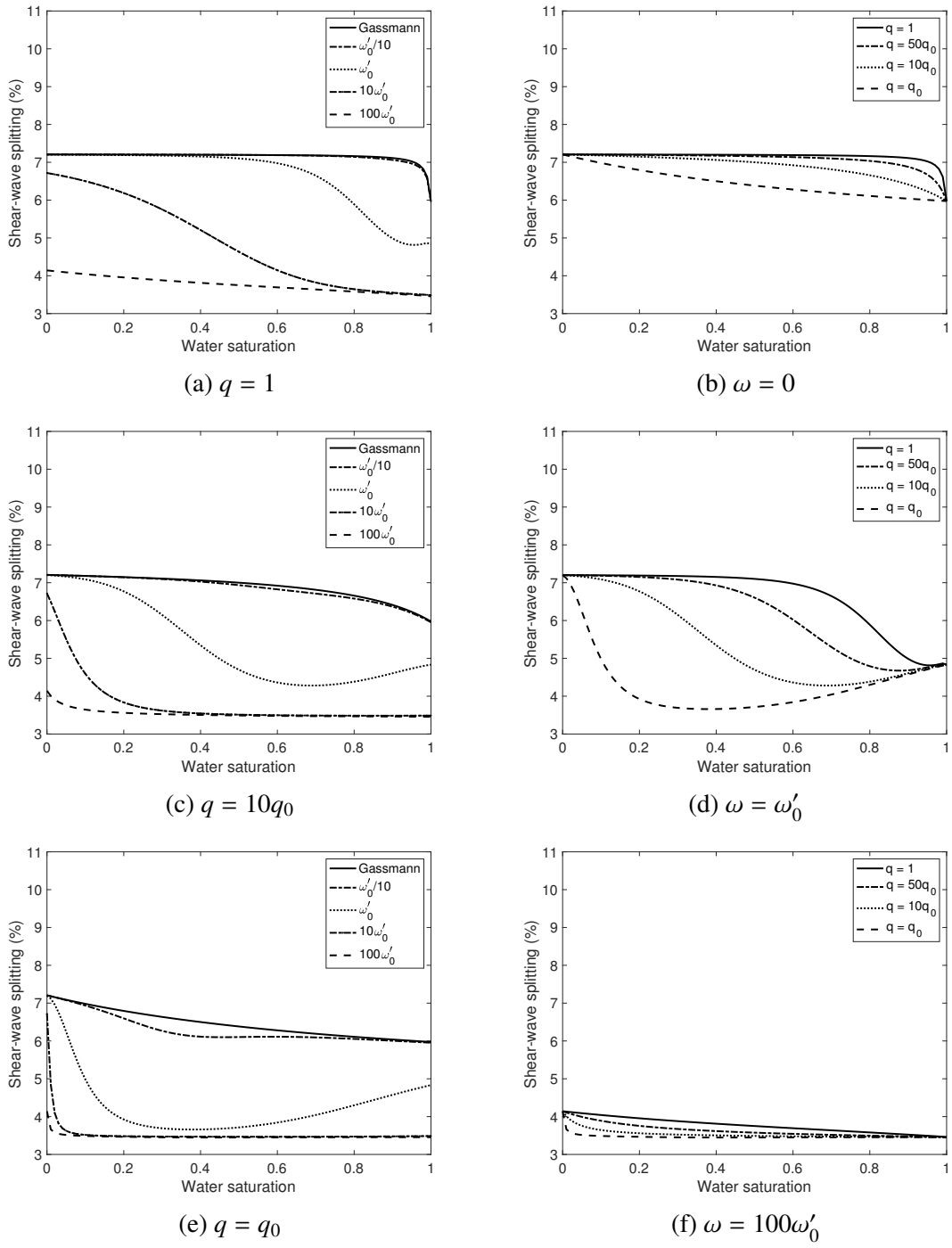

(a) $q = 1$ (b) $\omega = 0$

(c) $q = 10q_0$ (d) $\omega = \omega_0'$

(e) $q = q_0$ (f) $\omega = 100\omega_0'$

Figure 5.4: The variation of SWS with water saturation for a range of frequencies and the patch parameters q in the presence of fractures. Propagation is at 70 degrees to the fracture normal.

It is clear that SWS decreases with frequency. For the uniform saturation case, increasing water saturation generally results in a decreasing SWS. For the patchy saturation case, there can be certain points where SWS starts to increase with water saturation (e.g., at ω_0'). The presence of patchiness could also lead to a lower characteristic frequency where

the dispersion occurs. This effect has been more clearly explained in Figure 4.4 where the characteristic frequency depends on both water saturation and the patch parameter q. At intermediate water saturations, the characteristic frequency is more sensitive to q than it is at high or very low water saturations. As q goes lower, it is more likely that the characteristic frequency ω_f could sit below its value ω_0' at full water saturation.

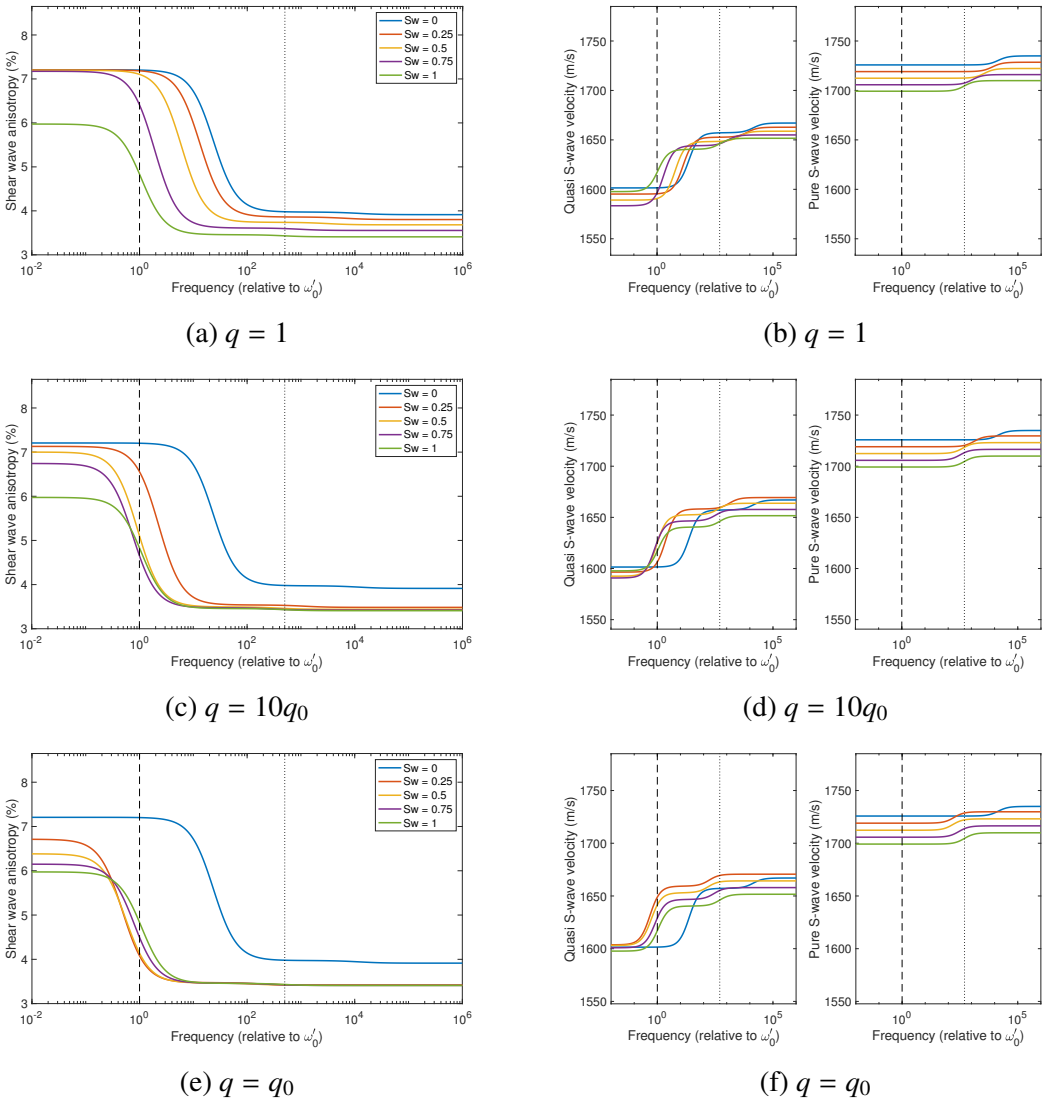

(a) $q = 1$ (b) $q = 1$

(c) $q = 10q_0$ (d) $q = 10q_0$

(e) $q = q_0$ (f) $q = q_0$

Figure 5.5: The variation of SWS, Quasi S-wave velocity and Pure S-wave velocity with frequency at various water saturations and q values. Propagation is at 70 degrees to the fracture normal. The dashed line represents the fracture-scale frequency ω_0', and the dotted line represents the grain-scale frequency ω_0.

5.4.2 Saturation effects on P-wave anisotropy

In section 5.4.1, I have studied the the effects of partial saturation on S-wave anisotropy in which a S-wave splits into quasi and pure S-waves as it travels through a TI medium. I show that the influence of relative permeability and patchy saturation on lowering the characteristic frequency at intermediate saturations could lead to non-monotonic behaviour of SWS with respect to changes in water saturation. Here I study how such effects could also affect P-wave anisotropy by considering the same porous rock which is saturated by water and supercritical CO_2. The parameters are given in Table 4.1. The velocity of quasi P-wave is calculated by equation 2.9.

Figure 5.6 shows the variation of qP-wave with frequency, with disperison occurs around two characteristic frequencies ω_m and ω_f. For propagation parallel to the fractures, Chapman (2003) showed that the qP-wave is unaffected by the presence of fractures below the characteristic frequency. This is still true for a partially saturated rock in the assumption of uniform saturation ($q = 1$), as shown in Figure 5.6a. The presence of patchy saturation (Figures 5.6b and 5.6c), however, leads to qP-wave dispersion around the characteristic frequency ω_f, and the water saturation effects become distinctive in comparison to the uniform saturation case. For propagation perpendicular to fractures, the patchy and squirt effects are more significant. Below the characteristic frequency ω_f, the qP-wave velocity is much lower than that for propagation parallel to fractures. At higher frequencies, the two velocities become identical at full water saturation, but show a slight difference at partial saturations. As the patch parameter q approaches the extreme value q_0, the qP-wave curves at partial saturations can go higher than that at full saturation, demonstrating a non-monotonic variation of qP-wave velocity with water saturation.

Figure 5.7 displays the angular variation of qP-wave velocity for a range of saturations and patch parameters q. At low or intermediate frequencies (e.g., $\omega = 0$, $\omega = \omega_0'$), qP-wave velocity increases with the increase of angle from 0 to 90 degrees. At very high frequencies (e.g., $\omega = 100\omega_0'$), the angular variation is relatively less great and could become non-monotonic. Patchy saturation also tends to amplify the velocity. The exact variation of qP-wave velocity with water saturation is displayed in Figure 5.8. Overall,

P-wave velocity increases with water saturation due to the stiffening effect of fluid mixture, but could also decrease with water saturation due to the effect of patchy saturation on lowering the characteristic frequency at intermediate water saturations. Such non-monotonic variation is demonstrated in Figure 5.8d where the frequency is at ω_0' and the patch parameter is set to be the extreme value q_0.

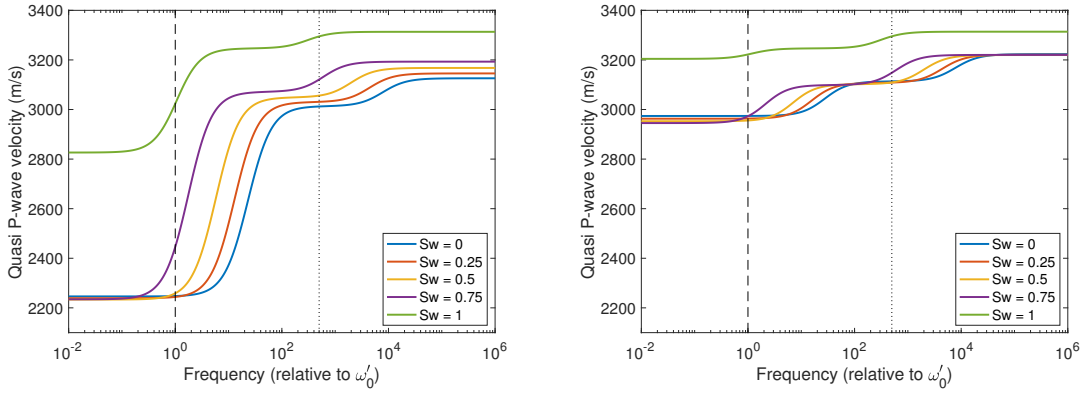

(a) $q = 1$

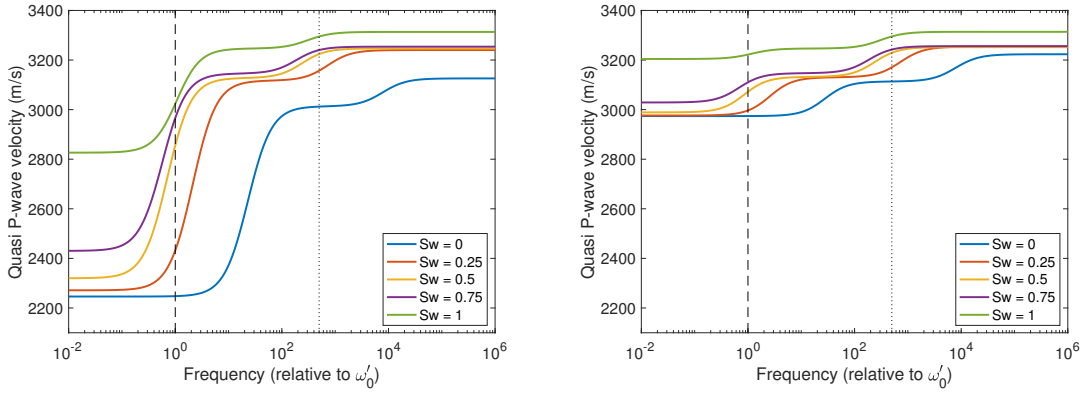

(b) $q = 10q_0$

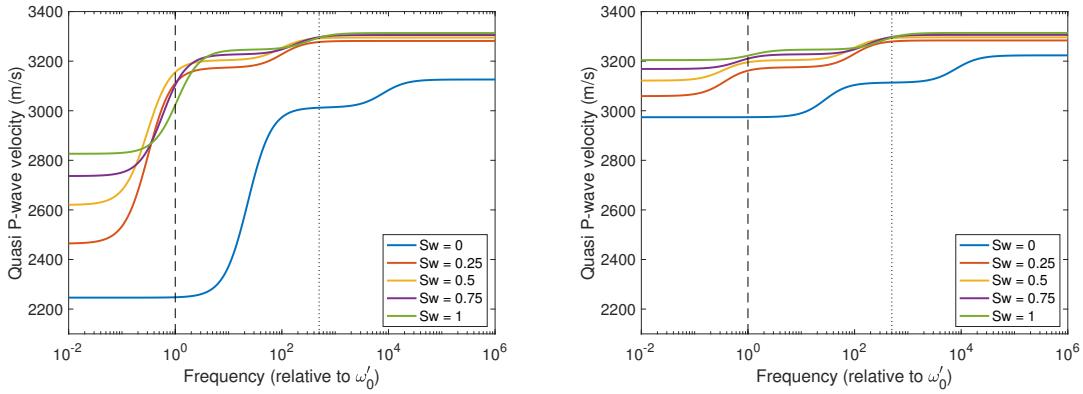

(c) $q = q_0$

Figure 5.6: The variation of Quasi P-wave velocity with frequency for a range of water saturations and the patch parameters q in the presence of fractures. On the left is propagation normal to fractures. On the right is propagation parallel to fractures.

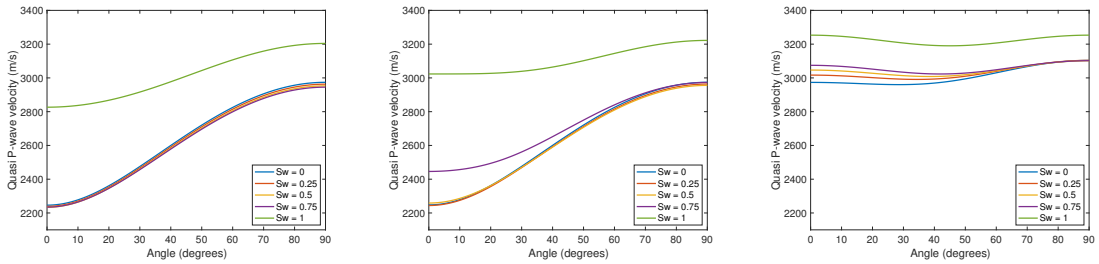

(a) $q = 1$. left: $\omega = 0$; middle: $\omega = \omega_0'$; right: $\omega = 100\omega_0'$

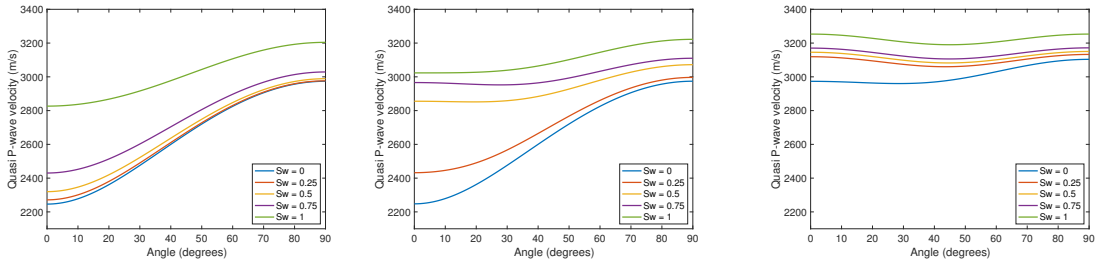

(b) $q = 10q_0$. left: $\omega = 0$; middle: $\omega = \omega_0'$; right: $\omega = 100\omega_0'$

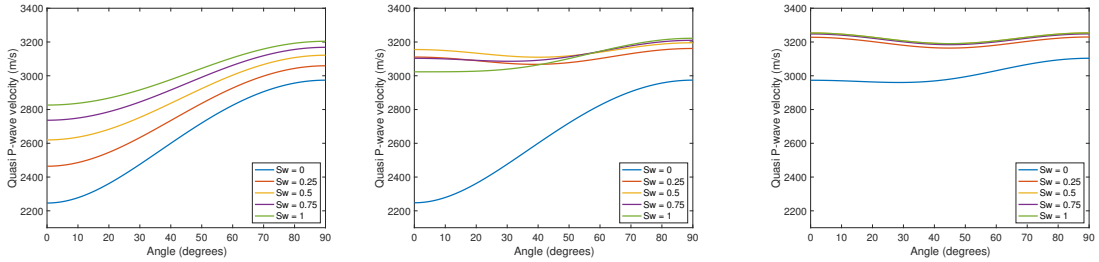

(c) $q = q_0$. left: $\omega = 0$; middle: $\omega = \omega_0'$; right: $\omega = 100\omega_0'$

Figure 5.7: The variation of Quasi P-wave velocity with angle for a range of water saturations and the patch parameters q in the presence of fractures. On the left is zero wave frequency; On the middle is ω_0' wave frequency; On the right is $100\omega_0'$ wave frequency.

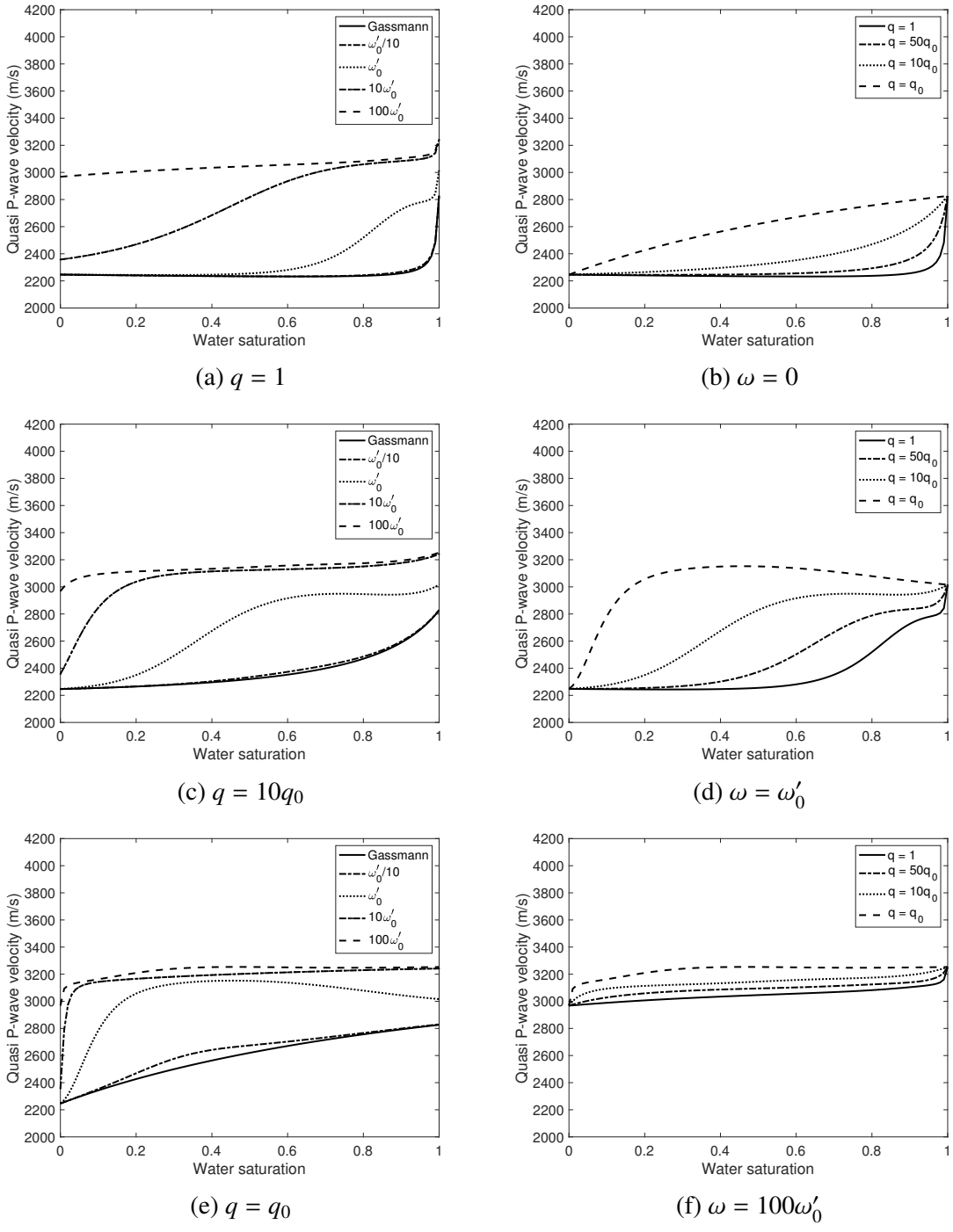

(a) $q = 1$ (b) $\omega = 0$

(c) $q = 10q_0$ (d) $\omega = \omega_0'$

(e) $q = q_0$ (f) $\omega = 100\omega_0'$

Figure 5.8: The variation of Quasi P-wave velocity with water saturation for a range of frequencies and the patch parameters q in the presence of fractures. Propagation is along the fracture normal.

5.5 The impact of relative permeability

In place of defining an explicit relative permeability model, I could alternately define a class of effective fluid models where fluid mobility is simply averaged (through an effective viscosity, in a generalization of the Amalokwu et al. (2014) approach) according to

$$M_f = \frac{1}{\tilde{q}} S_w M_w + \frac{q}{\tilde{q}} (1 - S_w) M_g. \tag{5.3}$$

Figure 5.9 compares the results from such an approach to those from the relative permeability model. In the case where the relative permeability effect is ignored, increasing water saturation would mainly lead to a stiffening effect that results in a monotonic increase in shear modulus and a decrease in SWS. Considering relative permeability, the effective fluid mobility would be lowered at intermediate saturations, leading to a lower characteristic frequency that gives rise to stronger dispersion on the elastic moduli. This leads to non-monotonic variations with respect to fluid saturation, and implies that inversion problem for monitoring fluid saturation from frequency-dependent anisotropy could be non-unique when relative permeability effects are important.

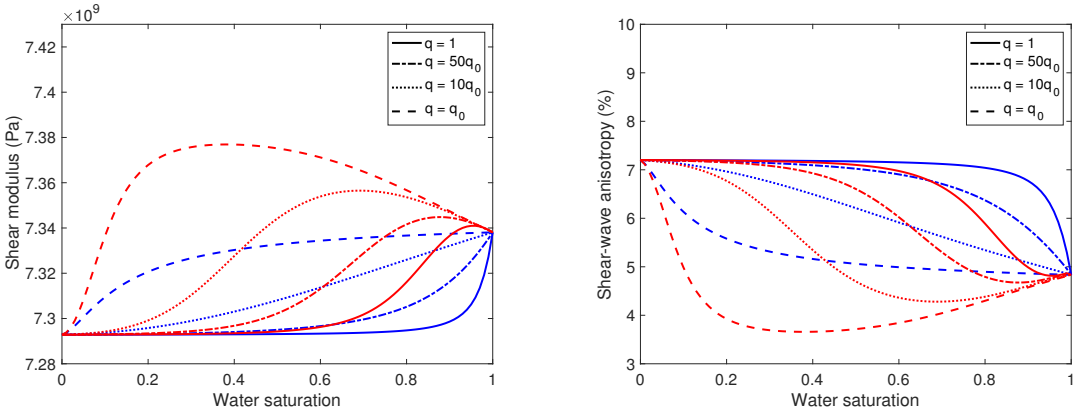

(a) (b)

Figure 5.9: The variation of (a) shear modulus and (b) SWS with water saturation for a range of q values at the reference frequency ω_0. The red curves represent the case with relative permeability effects; The blue curves represent the case given by equation 5.3 without relative permeability effects.

In my earlier derivation, I used the same relative permeability model for the grain-scale pores and cracks and meso-scale fractures, which results in the ratio of two charac-

teristic frequencies $\frac{\omega_m}{\omega_f}$ being the normalized fracture size (see equation 4.39). Such relationship has previously been used as the basis for estimating fracture size from frequency-dependent seismic data (Maultzsch et al., 2003a). Recently, it has been suggested that the presence of fractures in a water-gas saturated rock could significantly affect the relative permeability behaviours (Lu et al., 2016). Laboratory measurement by Falcon-Suarez et al. (2018) also shows that fractures tend to significantly reduce relative permeabilities of the brine-CO_2 system. It would therefore be ambiguous to relate fracture size with the $\frac{\omega_m}{\omega_f}$ ratio. Such effect was neglected in this thesis as I only choose a single relative permeability model for all inclusions. The potential impact of such fracture related relative permeability variations within the model could be addressed in the future by considering alternative relative permeability models such as the Brooks–Corey model.

5.6 Modelling experimental results

Controlled laboratory experiments on samples with well-defined physical or structural properties are often carried out for the development or validation of theoretical models. In order to improve the understanding of partial saturation effects on frequency-dependent anisotropy, a number of laboratory measurements have been conducted on synthetic silica-cemented sandstones containing aligned penny-shaped fractures (Amalokwu et al., 2014, 2015; Falcon-Suarez et al., 2019). These samples were manufactured at the National Oceanography Centre, Southampton (NOCS). They were made from a mixture of sand, kaolinite and sodium silicate gel following the method of Tillotson et al. (2012). Penny-shaped voids were created by arranging a pre-determined number of aluminium discs (leached out using acid after the rock solidifies) of 2 mm diameter and 0.2 mm thickness on successive 4 mm layers of sand mixture (Amalokwu et al., 2014). Fracture density, size and aspect ratio were then determined from X-ray CT scan images. The petrophysical properties of the synthetic sample are provided in Tillotson et al. (2012). In the following sections, I model these experimental results of partial saturation effects on P- and S-wave anisotropy using the derived squirt-patchy theory.

5.6.1 Case one: water/air saturations

Amalokwu et al. (2014) investigated the effects of water/air saturation on SWS through experimental measurements on the synthetic sandstone containing fractures aligned at 45 degrees to the fracture normal. The measured results show SWS being fairly constant between $S_w = 0 - 0.7$, and decreasing as it approaches full water saturation. Amalokwu et al. (2014) combined the partial saturation model of White (1975) and the single-fluid squirt model of Chapman (2003) to explain this saturation dependence, and discussed the importance of wave-induced fluid flow mechanisms due to the presence of partial liquid/gas saturation and fractures.

Here I attempt to model their experimental results by using my unified squirt-patchy theory. According to equation 4.50, the stiffness tensor consists of the isotropic $c^0(\lambda, \mu)$ of the matrix and additional corrections associated with c^1, c^2, c^3 from pores, microcracks and fractures. These require an estimation of the grain moduli λ and μ, which have to be fitted to achieve agreement with background velocities. Chapman et al. (2003) pointed out the inconvenience of specifying these moduli, and proposed to estimate the Lamé parameters λ^0 and μ^0 assuming that V_P^0, V_S^0, ρ^0 at some frequency f_0 are known from the isotropic unfractured rock, i.e.,

$$\lambda^0 = V_P^{0^2}\rho^0 - 2\mu^0; \quad \mu^0 = V_S^{0^2}\rho^0. \tag{5.4}$$

The practical version of the model can then be written as

$$c_{ij}(\omega) = c_{ij}^0(\Lambda, \Upsilon, \omega) - \phi_0^{\odot} c_{ij}^1\left(\lambda^0, \mu^0, \omega\right) - \varepsilon_0^{\ominus} c_{ij}^2\left(\lambda^0, \mu^0, \omega\right) - \varepsilon_0^{\dagger} c_{ij}^3\left(\lambda^0, \mu^0, \omega\right) \tag{5.5}$$

where the reference constants Λ and Υ are given by

$$\Lambda = \lambda^0 + \Phi_{c,p}\left(\lambda^0, \mu^0, f_0\right); \quad \Upsilon = \mu^0 + \Phi_{c,p}\left(\lambda^0, \mu^0, f_0\right) \tag{5.6}$$

where $\Phi_{c,p}$ representing perturbations from microcracks and pores.

Figure 5.10 shows the fitting model for SWS at 45 degrees to fracture normal. The

Table 5.1: Common parameters for modelling experimental data used by Amalokwu et al. (2014) and this work. The use of White's mixing law is replaced with the consistent squirt-patchy model in this work.

V_P^0 (m/s)	3250	Porosity (unfractured)	30.43%
V_S^0 (m/s)	2200	Crack density	0
ρ_0 (Kg/m^3)	1800	Aspect ratio	0.088
Measurement frequency (kHz)	650	Solid density (Kg/m^3)	2590
Fracture density	0.0298	Fracture length (m)	0.005
Water viscosity (Pa.s)	1.0×10^{-3}	Air viscosity (Pa.s)	2.0×10^{-5}
Water density (Kg/m^3)	1000	Air density (Kg/m^3)	1.2
Water modulus (Pa)	2.25×10^9	Air modulus (Pa)	1.0×10^5

modelling parameters are displayed in Table 5.1, which are inferred from Amalokwu et al. (2014) and Amalokwu et al. (2016). By matching measurements on the unfractured sample and SWS on the fractured rock at dry condition, I use the reference parameters $V_P^0 = 3250$ m/s, $V_S^0 = 2200$ m/s and $\rho^0 = 1800$ Kg/m^3 to derive the Lamé parameters as $\lambda^0 = 1.59$ GPa and $\mu^0 = 8.71$ GPa. In the case of high porosity, crack density can be set to zero as has been shown by Chapman et al. (2003). I then scan through the combinations of the characteristic frequency ω_0' at full water saturation and the non-dimensional parameter q to calculate the L_2 norm (misfit) of the errors between the data and the model predictions. From Figure 5.10a, the minimum misfit is achieved by taking $\omega/\omega_0' = 0.45$ and $q = 0.004$, respectively. The corresponding relaxation time is $1.7 \times 10^{-8} s$, which is close to the value given by Amalokwu et al. (2014). The intermediate value of q suggests contribution from patch effects. Figure 5.10b shows the best fitting curve. The decreasing SWS trend observed by Amalokwu et al. (2014) can therefore be well modelled using my theory by considering the coupling of squirt and patchy mechanisms.

Amalokwu et al. (2015) continued to measure water/air saturation effects on P-wave anisotropy using octagonal samples synthesized by Tillotson et al. (2014), the manufacturing process of which is essentially the same to that by Tillotson et al. (2012). X-ray CT scan image shows that the fracture density is 0.0314 ± 0.0059, the mean fracture radius is 2.91 ± 0.06 mm, and the total porosity is 33%. Similarly, I follow the modelling scheme shown above to achieve a good fitting with P-wave measurements taken at 0°, 45° and 90° to fracture normal. Figure 5.11 displays the fitting results of P-wave moduli changing

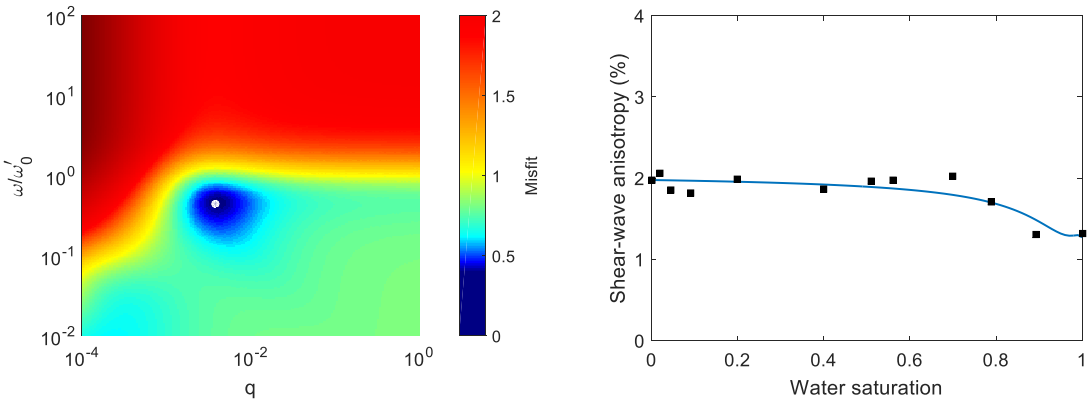

(a) (b)

Figure 5.10: Model fit to the SWS trend measured by Amalokwu et al. (2014). (a) Misfits between data and model predictions at various combinations of ω_0' and q. The location of the minimum misfit is labelled with white circle; (b) Best fitting curve to the measured SWS.

with water saturation. The crack density has to be as high as 0.16 in this case to account for dispersion close to full saturation. ω/ω_0' and q are determined as 0.29 and 0.0002. This again indicates coupled squirt and patchy effects.

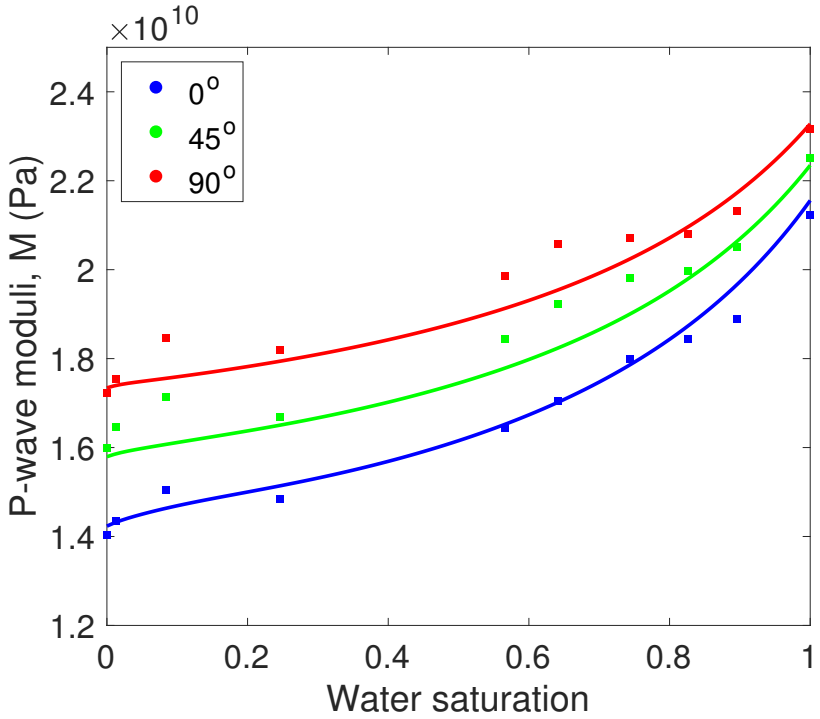

Figure 5.11: Fitting curves for P-wave moduli varying with water saturation measured by Amalokwu et al. (2015).

5.6.2 Case two: brine/CO_2 saturations

In order to understand the effects of fractures and fluid during and after CO_2 injection in fractured CCS reservoir, Falcon-Suarez et al. (2019) performed a Brine-CO_2 flow-through (BCFT) test on the synthetic sample used by Amalokwu et al. (2014) under realistic geological conditions of confining (40 MPa) and pore (10 MPa) pressure. The BCFT procedure was described by Falcon-Suarez et al. (2017), which in this experiment contains a drainage stage with brine/CO_2 flow increasing from $100:0$ to $0:100$ by steps of 20% followed by an imbibition stage where the original brine was forced to flow back. The maximum CO_2 saturation achieved in the BCFT is below 60% due to the capillary effects of the wetting phase (brine). This is in agreement with most of the previous water-CO_2 drainage tests in sandstones (Burnside and Naylor, 2014). Figure 5.12 shows the results of P- and S-wave velocities varying with the change of brine saturation. The injection of CO_2 into a fully saturated rock generally leads to a decrease in P-wave velocity due to the fluid stiffening effect (Domenico, 1976). In this experiment they show an increase which is in contrast to conventional understanding of saturation effects. From the perspective of the squirt-patchy theory derived in Chapter 4, such non-monotonic variation could be explained by the strong dispersion resulted from the effects of patchy saturation and low fluid mobility on lowing the characteristic frequencies. The experiment also shows fairly constant S-wave velocities, demonstrating minimal dispersion effects on shear properties.

I now use the squirt-patchy theory to interpret these experimental results. I intend to model the P- and S-wave results simultaneously. Chapman (2003) has shown that the quasi S-wave is more sensitive to dispersion than the pure S-wave, and could be either the fast (S_1) or the slow (S_2) wave depending on the frequency. I notice that the measured S_2 wave velocities are slightly decreasing with brine saturation due to the density effect and shows minimal dispersion. In contrast, the S_1 wave shows a slight increase with saturation, demonstrating a potential dispersion effect. I therefore assume that the faster S_1 wave is the quasi S-wave and the slower S_2 wave is the pure S-wave. The measurement frequency in this case should be higher than the fracture-scale characteristic frequency, which means that there is merely contribution from the fracture-induced dispersion. I

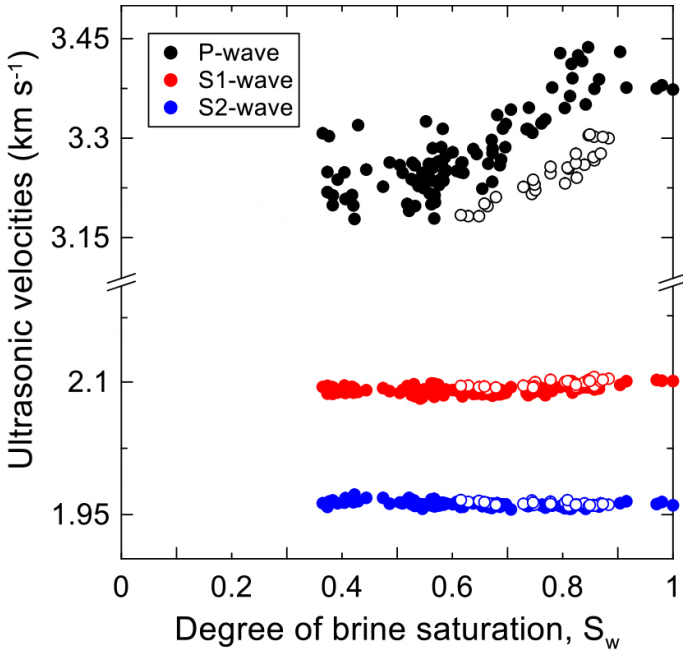

Figure 5.12: P- and S-wave velocities for the whole range of brine saturation measured from the Brine-CO_2 flow-through test in fractured sandstone. Solid and empty symbols indicate drainage and imbibition conditions, respectively.

therefore set the ratio between the two characteristic frequencies as $\frac{\omega_m}{\omega_f} = 1000$. I also notice a strong stiffening of P-wave velocities at around 80% brine saturation, which could be a result of the effect of relative permeability and patchy saturation on reducing the characteristic frequencies. To account for such effect, I choose to use the Brooks-Corey relative permeability model (Brooks and Corey, 1964) with λ_{B-C} being determined as $\frac{1}{6}$. The residual water saturation is set to be zero for simplification. The patch parameter is chosen as $q = 2q_0$. The measurement frequency could therefore be within a range close to the micro-scale characteristic frequency ω_0, as is illustrated by the shaded area in Figure 5.13a.

Due to the lack of measurements on isotropic unfractured sample, I choose to estimate the grain moduli λ and μ by fitting the P-, S_1- and S_2-wave velocities simultaneously using the squirt-patchy theory in which the measurement frequency is constrained close to ω_0 such that the quasi S-wave is the faster S_1 wave and the pure S-wave is the slower S_2 wave. By applying a least-square algorithm to fit velocities at full saturations for the BCFT measurements, I invert λ and μ as 13.1 GPa and 21.9 Gpa. The fracture density and crack density are determined as 0.04 and 0.015, respectively. Although the synthetic sandstone

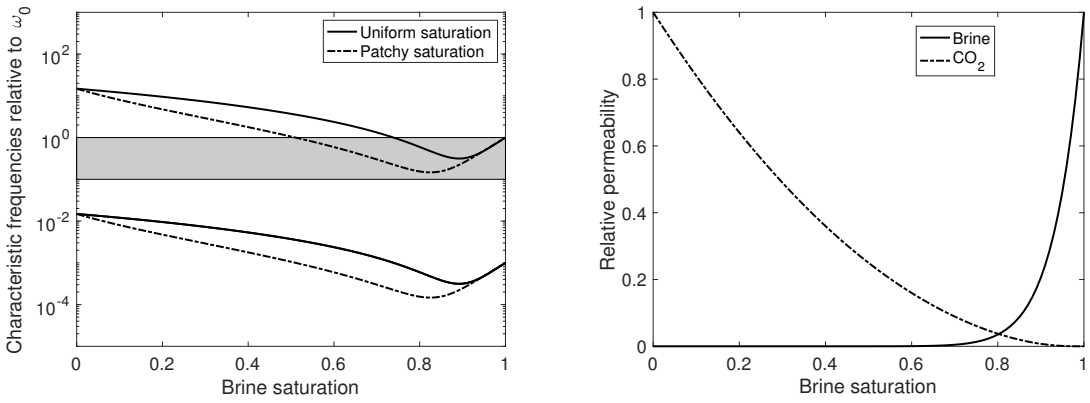

(a) (b)

Figure 5.13: (a) The characteristic frequencies of the Brine-CO_2 saturated sample; (b) The Brooks-Corey relative permeability model with $\lambda_{B-C} = \frac{1}{6}$.

Table 5.2: Parameters used for modelling the measurements by Falcon-Suarez et al. (2019).

λ (Pa)	1.31×10^{10}	Porosity	27.3%
μ (Pa)	2.19×10^{10}	Crack density	0.015
Measurement frequency (kHz)	600	Solid density (Kg/m^3)	2590
Fracture density	0.04	Aspect ratio	10^{-4}
Brine viscosity (Pa.s)	1.2×10^{-3}	CO_2 viscosity (Pa.s)	8.1×10^{-5}
Brine density (Kg/m^3)	1050	CO_2 density (Kg/m^3)	800
Brine modulus (Pa)	2.4×10^9	CO_2 modulus (Pa)	0.2×10^9

is the same as used by Amalokwu et al. (2014), I notice that the porosity is measured by Falcon-Suarez et al. (2019) as 27.3%, which is different to that used by Amalokwu et al. (2014). This could be a result of repeated sample preparation and pressure cycling. A full list of petrophysical parameters used for the modelling are provided in Table 5.2.

Figure 5.14 shows the fitted model to the P-wave velocities at various frequencies relative to ω_0. The solid curve denotes fitting results based on the uniform saturation assumption, which shows a proper agreement with the imbibition results but clearly underestimates velocities from the drainage tests. A good fit to the drainage results can be achieved with the consideration of patchy saturation. Particularly, the velocity jump at around 80% brine saturation can be well explained by the effects of patchy saturation and relative permeability effects on giving rise to a stronger dispersion. Figures 5.15 and 5.16 are the fitting results to the S_1 and S_2 velocities and the corresponding SWS. Within the specified micro-scale frequency range, the squirt-patchy theory predicts that the shear

properties are much less sensitive to fluid saturation compared to P-waves. This is fairly supported by the laboratory measurements.

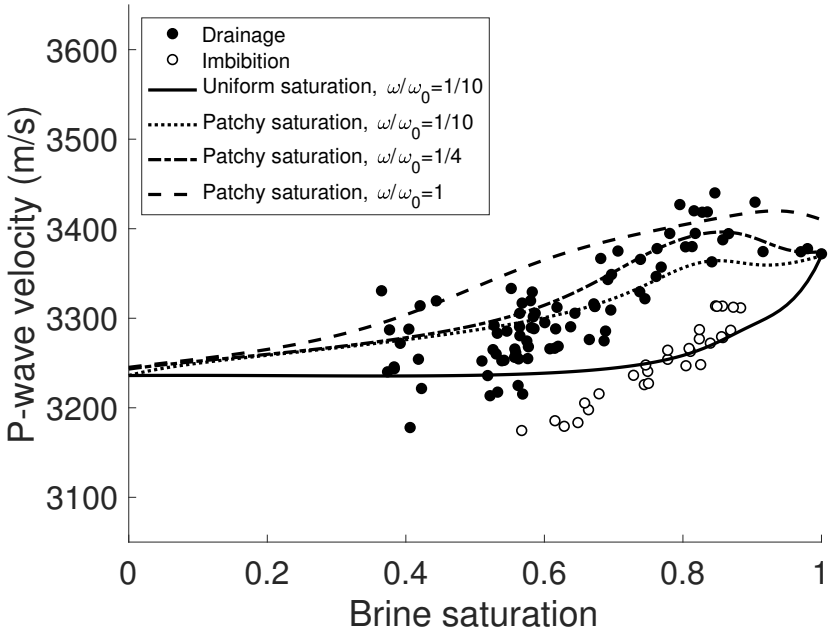

Figure 5.14: Model fit to P-wave velocities varying with brine saturation measured by Falcon-Suarez et al. (2019).

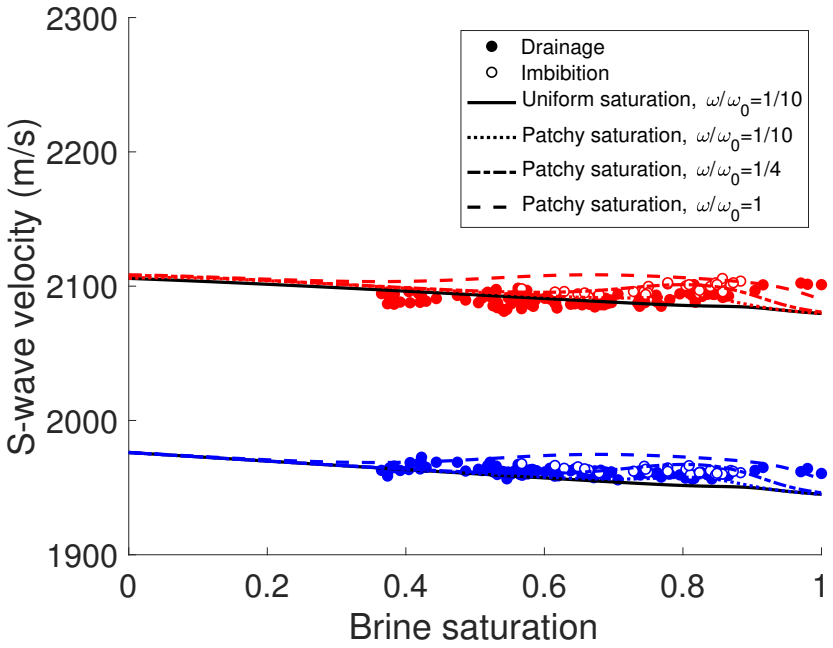

Figure 5.15: Model fit to S-wave velocities varying with brine saturation measured by Falcon-Suarez et al. (2019). The red symbols indicate the faster S_1 wave data, and the blue symbols indicate the slower S_2 wave data.

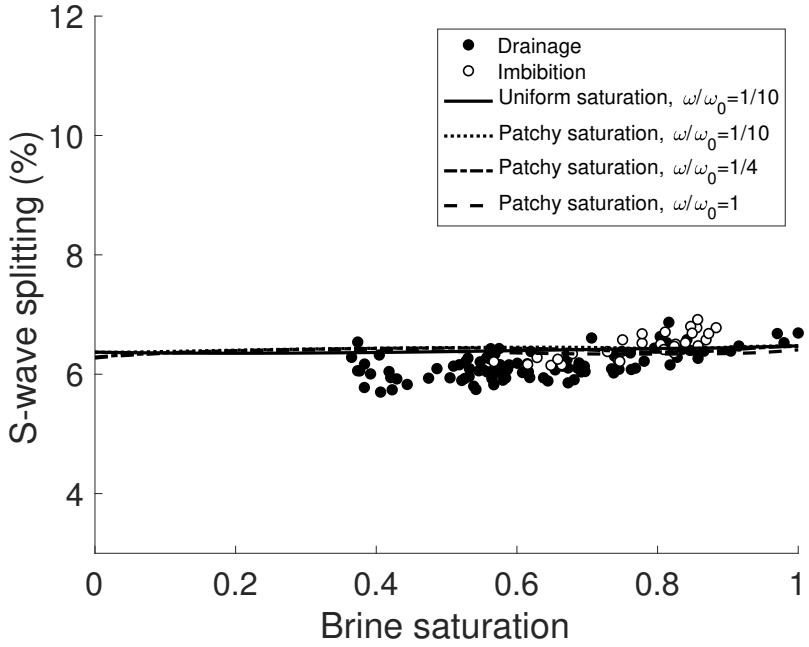

Figure 5.16: Model fit to SWS varying with brine saturation measured by Falcon-Suarez et al. (2019).

5.7 Conclusion

I have shown how P- and S-wave properties of a fractured rock saturated with two immiscible fluids can be influenced by coupled squirt and patch effects. The effects of relative permeability could lead to non-monotonic behaviour of shear properties and P-wave velocities with respect to changes in water saturation, which may complicate the inversion of fluid content from seismic data. While the squirt and patch effects on shear properties are weaker than that on bulk properties, the impact on SWS in fractured rocks is potentially significant. Patchy saturation tends to reduce SWS due to its effect on lowering the characteristic frequency at intermediate saturations. The theory conveniently models recent experimental data, emphasising the requirement to include coupled squirt and patch mechanisms for the analysis of saturation effects on frequency-dependent anisotropy.

Chapter 6

Frequency-dependent azimuthal effects on P-wave reflections

Abstract: Seismic anisotropy has widely been used for the characterization of fractures in a reservoir. Recent work has demonstrated the effect of seismic dispersion on producing a frequency-dependent reflection coefficient, which can be important in fracture characterization since large fractures often lead to frequency-dependent anisotropy. In this chapter, I use the squirt-patchy theory derived in Chapter 4 to examine the impact of anisotropic dispersion on P-wave reflections based on an HTI sand model overlaid by VTI shale. Although VTI in the overburden does not lead to azimuthal anisotropy, its effect on angle dependence could significantly affect the azimuthal AVO responses at far offsets. I show a modest effect on the amplitude and large effect on the phase, the latter of which could even be mistaken for azimuthal velocity variations. I present a Bayesian inversion based on a forward modelling technique aimed at recovering water saturation, fracture density and fracture length of a HTI sand. The results show potential of using frequency-dependent azimuthal AVO for the discrimination of large-scale fractures from micro-scale cracks.

6.1 Introduction

The detection of fractures in a reservoir is of great interest because fracturing can significantly affect fluid flow during hydrocarbon production. Studies on the variation of P-wave reflectivity with azimuth and offset have gained much attention since it can be analysed to determine the orientation and density of fractures (e.g., Lynn et al., 1995; Rüger, 1998; Hall and Kendall, 2003). However, the estimation of fracture sizes from P-wave reflection remains to be a challenge since conventional seismic anisotropy is considered insensitive to the fracture length (Hudson, 1981; Liu et al., 2000).

It is known that the presence of fractures in a reservoir often leads to frequency-dependent anisotropy (FDA), which has been observed by Marson-Pidgeon and Savage (1997), Chesnokov et al. (2001) and Al-Harrasi et al. (2011). A vast literature also exits on the development of rock physics theories that describe such fracture-induced dispersion (e.g., Chapman, 2003; Gurevich, 2003; Brajanovski et al., 2005; Liu et al., 2006; Chapman, 2009; Jakobsen and Chapman, 2009; Guo et al., 2017; Collet and Gurevich, 2016). During the past decade, increasing attention has been paid to the potential effect of frequency-dependence on reservoir characterization, suggesting a frequency-dependent reflection coefficient that could be potentially important (Chapman et al., 2006; Odebeatu et al., 2006; Ren et al., 2009; Innanen, 2011; Liu et al., 2018). Particularly, the attention has been focused on the detection of fluid saturation. Wu et al. (2014) proposed a method to estimate gas saturation from pre-stack seismic data in a partially saturated sand based on frequency-dependent reflectivity and rock physics theory. Jin et al. (2017) extended the method to a thin-layer case by incorporating frequency-dependent reflectivity into convolutional modelling, which allows them to synthesize forward seismic traces from well logs and investigate the effects of seismic dispersion on waveforms. These studies assumed the absence of fractures and therefore are limited to isotropic reservoirs.

In the presence of fractures, the use of anisotropic dispersion has shown potential for accurately characterizing fracture properties. A majority of studies take advantage of shear-wave splitting (e.g., Maultzsch et al., 2003a; Al-Harrasi et al., 2011) and attenuation (Chapman, 2003; Chichinina et al., 2006; Liu et al., 2007; Wang et al., 2015; Ekanem

et al., 2016), while less attention has been paid to the impact of FDA on azimuthal P-wave reflections. Ali and Jakobsen (2011) studied the influence of multiple fracture sets on frequency-dependent P-wave velocities. Ali and Jakobsen (2014) investigated the potential use of frequency-dependent azimuthal P-wave reflection data for the determination of effective permeability in a fractured reservoir. However, these studies mentioned above as well as most of current theories have been limited to the single fluid assumption, despite the fact that almost all reservoirs are partially saturated. Considering these issues, in this Chapter I investigate the impact of partial saturation on anisotropic P-wave dispersion using the theory derived in Chapter 4, which quantitatively describes the coupled squirt and patch effects on FDA in a fractured rock saturated by two immiscible fluids. I also study how such effects influence azimuthal P-wave reflections, as deviations from the elastic assumption could potentially affect the interpretation of seismic data and the accuracy of fracture characterization.

In this Chapter, I develop a convolutional FDA modelling by extending the method of Jin et al. (2017) to anisotropic case and investigate the influence of FDA on azimuthal P-wave reflection based on an HTI sand model overlaid by an elastic shale. The results suggest that the main impact of FDA is on azimuthal phase, and the presence of transverse isotropy with vertical symmetry axis (VTI) in the overlying shale could significantly affect the azimuthal behaviour of frequency-dependent AVO responses. Recognizing the impact of seismic dispersion in fractured media could potentially help differentiate between large-scale and micro-scale fractures.

I start by introducing the calculation of frequency-dependent reflection coefficient in partially saturated rock with aligned fractures modelled by the derived squirt-patchy theory. I then review the convolutional modelling generalized by Jin et al. (2017) for the computation of synthetic seismic traces. I base the frequency-dependent azimuthal AVO study on the Class I model of Rutherford and Williams (1989) where I consider the overlying shale being either isotropic or anisotropic (VTI). Phase variations with both incidence and azimuth angles are particularly investigated. Finally, I consider a model-based Bayesian inversion to recover the water saturation, fracture density, and fracture length of

the dispersive target. The results show potential of using pre-stack reflection data to recover water saturation and to differentiate between large-scale and micro-scale fractures.

6.2 Theory and methods

6.2.1 Calculation of reflection coefficients in anisotropic media

The exact calculation of the amplitudes of reflected and transmitted plane waves from both incident P- and S-waves at an interface between two elastic media is given by Zoeppritz equations. The presence of dispersion and anisotropy in the media suggests that the reflectivity can be frequency dependent. In this study, the reflection coefficient is calculated by incorporating the derived squirt-patchy theory into Zoeppritz equations generalized by Schoenberg and Protázio (1992).

Assuming the anisotropic medium has a horizontal plane of symmetry parallel to the $x_1 - x_2$ plane (i.e., the medium is at least monoclinic), let $x_3 = 0$ be the horizontal interface between two half spaces. In order to study the wave propagation, it is necessary to calculate the vertical and horizontal slowness, as well as the polarizations of the ray. To simplify the problem from the perspective of Snell's law, the horizontal components of slowness are assumed to be real and constant in all layers, which may correspond to flat sequences and the source being placed in an elastic layer. Let the incident wave in the upper elastic medium be specified with angle of incidence θ and azimuth ϕ, the direction of propagation can be expressed as

$$\mathbf{n} = \begin{bmatrix} \sin\theta\cos\phi \\ \sin\theta\sin\phi \\ \cos\theta \end{bmatrix}. \tag{6.1}$$

The slowness ξ of this incident wave is calculated to be

$$\xi = \sqrt{\frac{\rho}{\chi}} \tag{6.2}$$

where ρ is the density of the rock, and χ is taken as the real part of the smallest eigenvalue of the matrix $c_{ijkl}n_in_k$ (Chapman and Liu, 2003). The slowness vector is then given by

$$\mathbf{s} = \xi\mathbf{n}. \tag{6.3}$$

The horizontal slowness s_1 (in the x_1 direction) and s_2 (in the x_2 direction) are therefore

$$s_1 = \xi\sin\theta\cos\phi; \quad s_2 = \xi\sin\theta\sin\phi. \tag{6.4}$$

Keeping s_1 and s_2 constant for all waves interacting at the interface, the next steps are to calculate the vertical slowness and polarizations of the ray, which can be determined from the frequency-dependent elastic moduli by solving the equations of motion.

In the general three dimensional case, the displacement of the harmonic plane wave of unit amplitude can be written as

$$\boldsymbol{u} = \begin{bmatrix} e_1 \\ e_2 \\ e_3 \end{bmatrix} \exp i\omega\left(s_1x_1 + s_2x_2 + s_3x_3 - t\right) \tag{6.5}$$

where e_1, e_2 and e_3 represent polarizations, and s_3 is vertical slowness.

Tsvankin (2001) gave the analytic description of plane waves in the form of

$$\rho\frac{\partial^2 u_i}{\partial t^2} = c_{ijkl}\frac{\partial^2 u_k}{\partial x_j \partial x_l} \tag{6.6}$$

where ρ is the density, u is the displacement, and c_{ijkl} represents the elastic stiffness tensor.

Substituting equation 6.5 into equation 6.6 gives

$$\rho u_i = \Gamma_{ik}u_k \tag{6.7}$$

where $\Gamma_{ik} = c_{ijkl}s_ls_j$ is defined as Christoffel matrix. It is clear that Christoffel matrix plays the role of linking elastic moduli with horizontal and vertical slowness.

Equation 6.7 can be rewritten as

$$(\rho\delta_{ik} - \Gamma_{ik})\, u_k = 0 \tag{6.8}$$

by introducing the Kronecker parameter, which is expressed as

$$\delta_{ik} = \begin{cases} 1 & i = k \\ 0 & i \neq k \end{cases} . \tag{6.9}$$

The relationship between the vertical slowness s_3 and elastic moduli $c_{ijkl}(\omega)$ can therefore be obtained by solving the equation

$$|\rho\delta_{ik} - \Gamma_{ik}| = 0 \tag{6.10}$$

of which the eigenvalues are squared solutions of vertical slowness s_{3_p}, s_{3_s} and s_{3_t} for quasi-P wave, the first arriving quasi-S wave, and the last arriving quasi-S wave respectively, and the associated eigenvectors are corresponding polarizations $\boldsymbol{e_p}$, $\boldsymbol{e_s}$ and $\boldsymbol{e_t}$.

As the waves propagate through the horizontal interface $x_3 = 0$, there are two boundary conditions that must be obeyed. The first one is the continuity of displacement, and the second one is the continuity of traction.

According to the solution of wave equation, the displacement field in the upper layer

can be written as

$$\begin{aligned}\begin{bmatrix} v_1 \\ v_2 \\ v_3 \end{bmatrix} = i_p \begin{bmatrix} e_{p_1} \\ e_{p_2} \\ e_{p_3} \end{bmatrix} \exp i\omega s_{3_p} x_3 + r_p \begin{bmatrix} e_{p_1} \\ e_{p_2} \\ -e_{p_3} \end{bmatrix} \exp -i\omega s_{3_p} x_3 \\ + i_s \begin{bmatrix} e_{s_1} \\ e_{s_2} \\ e_{s_3} \end{bmatrix} \exp i\omega s_{3_s} x_3 + r_s \begin{bmatrix} e_{s_1} \\ e_{s_2} \\ -e_{s_3} \end{bmatrix} \exp -i\omega s_{3_s} x_3 \\ + i_t \begin{bmatrix} e_{t_1} \\ e_{t_2} \\ e_{t_3} \end{bmatrix} \exp i\omega s_{3_t} x_3 + r_t \begin{bmatrix} e_{t_1} \\ e_{t_2} \\ -e_{t_3} \end{bmatrix} \exp -i\omega s_{3_t} x_3 \end{aligned} \tag{6.11}$$

where i_p, r_p, i_s, r_s, i_t, and r_t are amplitudes of the incident quasi-P wave, reflected quasi-P wave, incident fast quasi-S wave, reflected fast quasi-S wave, incident slow quasi-S wave, and reflected slow quasi-S wave respectively. In the case where there is only incident P-wave, i_s and i_t can be set to be zero.

The lower medium only has transmitted waves, hence the displacement field is written as

$$\begin{bmatrix} v'_1 \\ v'_2 \\ v'_3 \end{bmatrix} = t_p \begin{bmatrix} e'_{p_1} \\ e'_{p_2} \\ e'_{p_3} \end{bmatrix} \exp i\omega s'_{3_p} x_3 + t_s \begin{bmatrix} e'_{s_1} \\ e'_{s_2} \\ e'_{s_3} \end{bmatrix} \exp i\omega s'_{3_s} x_3 + t_t \begin{bmatrix} e'_{t_1} \\ e'_{t_2} \\ e'_{t_3} \end{bmatrix} \exp i\omega s'_{3_t} x_3 \tag{6.12}$$

where t_p, t_s and t_t are amplitudes of the transmitted quasi-P, fast quasi-S and slow quasi-S waves, and all other primed parameters have the same meanings as the normal ones in equation 6.11.

The stress traction is defined by

$$T_i = \sigma_{ij} \hat{n}_j \tag{6.13}$$

where $\hat{n}_j$ is the unit normal vector of the surface that the traction acts on, and σ_{ij} is the stress tensor. By expending equation 6.13, the traction on the horizontal plane (i.e.,

constant x_3 plane) can be written as

$$\mathbf{T} = \begin{bmatrix} \sigma_{11} & \sigma_{12} & \sigma_{13} \\ \sigma_{21} & \sigma_{22} & \sigma_{23} \\ \sigma_{31} & \sigma_{32} & \sigma_{33} \end{bmatrix} \begin{bmatrix} 0 \\ 0 \\ 1 \end{bmatrix} = \begin{bmatrix} \sigma_{13} \\ \sigma_{23} \\ \sigma_{33} \end{bmatrix} \tag{6.14}$$

where n_1 and n_2 are zero (because traction is on the constant x_3 plane), and n_3 has to be one. Equation 6.14 can be further simplified as

$$\mathbf{T} = \begin{bmatrix} \sigma_{13} \\ \sigma_{23} \\ \sigma_{33} \end{bmatrix} = \begin{bmatrix} \sigma_5 \\ \sigma_4 \\ \sigma_3 \end{bmatrix} \tag{6.15}$$

where σ_{13}, σ_{23} and σ_{33} are rewritten as σ_5, σ_4 and σ_3 according to the abbreviated Voigt notation (Auld, 1990). Similarly, the traction field in the lower medium is

$$\mathbf{T}' = \begin{bmatrix} \sigma'_5 \\ \sigma'_4 \\ \sigma'_3 \end{bmatrix} \tag{6.16}$$

with primed parameters.

According to Hooke's law, the stress σ_{ij} is proportional to the strain ε_{kl}, which can be further related to the displacement v_i by equations

$$\sigma_{ij} = c_{ijkl}\varepsilon_{kl}, \varepsilon_{kl} = \frac{1}{2}\left(v_{k,l} + v_{l,k}\right) \tag{6.17}$$

where the comma , denotes partial derivative. Hence, the traction fields can also be written in a similar form as equation 6.11 and 6.12 from the above stress-strain-displacement relationship.

To simplify the displacement and traction fields as matrix forms, Schoenberg and

Protázio (1992) introduced two impedance matrices as

$$\mathbf{X} = \begin{bmatrix} e_{p_1} & e_{s_1} & e_{t_1} \\ e_{p_2} & e_{s_2} & e_{t_2} \\ -\left(c_{13}e_{p_1} + c_{36}e_{p_2}\right)s_1 & -\left(c_{13}e_{s_1} + c_{36}e_{s_2}\right)s_1 & -\left(c_{13}e_{t_1} + c_{36}e_{t_2}\right)s_1 \\ -\left(c_{23}e_{p_2} + c_{36}e_{p_1}\right)s_2 & -\left(c_{23}e_{s_2} + c_{36}e_{s_1}\right)s_2 & -\left(c_{23}e_{t_2} + c_{36}e_{t_1}\right)s_2 \\ -c_{33}s_{3_p}e_{p_3} & -c_{33}s_{3_s}e_{s_3} & -c_{33}s_{3_t}e_{t_3} \end{bmatrix} \tag{6.18}$$

and

$$\mathbf{Y} = \begin{bmatrix} -\left(c_{55}s_1 + c_{45}s_2\right)e_{p_3} & -\left(c_{55}s_1 + c_{45}s_2\right)e_{s_3} & -\left(c_{55}s_1 + c_{45}s_2\right)e_{t_3} \\ -\left(c_{55}e_{p_1} + c_{45}e_{p_2}\right)s_{3_p} & -\left(c_{55}e_{s_1} + c_{45}e_{s_2}\right)s_{3_s} & -\left(c_{55}e_{t_1} + c_{45}e_{t_2}\right)s_{3_t} \\ -\left(c_{45}s_1 + c_{44}s_2\right)e_{p_3} & -\left(c_{45}s_1 + c_{44}s_2\right)e_{s_3} & -\left(c_{45}s_1 + c_{44}s_2\right)e_{t_3} \\ -\left(c_{45}e_{p_1} + c_{44}e_{p_2}\right)s_{3_p} & -\left(c_{45}e_{s_1} + c_{44}e_{s_2}\right)s_{3_s} & -\left(c_{45}e_{t_1} + c_{44}e_{t_2}\right)s_{3_t} \\ e_{p_3} & e_{s_3} & e_{t_3} \end{bmatrix} \tag{6.19}$$

where c_{ij} are the elastic moduli with abbreviated Voigt notation which can be estimated from the squirt-patchy model given by equation 4.50.

Let the upper layer be characterized by impedance matrices $\mathbf{X}$ and $\mathbf{Y}$, and the lower layer be associated with $\mathbf{X}'$ and $\mathbf{Y}'$, which have the same forms as equations 6.18 and 6.19 but with the elements being primed parameters, the frequency-dependent reflection matrix is calculated to be

$$\mathbf{R} = \left(\mathbf{Y}'^{-1}\mathbf{Y} + \mathbf{X}'^{-1}\mathbf{X}\right)^{-1}\left(\mathbf{Y}'^{-1}\mathbf{Y} - \mathbf{X}'^{-1}\mathbf{X}\right) = \begin{bmatrix} R_{PP} & R_{SP} & R_{TP} \\ R_{PS} & R_{SS} & R_{TS} \\ R_{PT} & R_{ST} & R_{TT} \end{bmatrix}. \tag{6.20}$$

The P-to-P reflection coefficient at frequency ω is given by R_{PP} from the solution of

equation 6.20. In this case, the P-to-P reflection coefficient is frequency dependent and complex.

6.2.2 Forward modelling of seismic reflections in anisotropic dispersive media

In section 6.2.1, the frequency-dependence of the reflection coefficients is modelled by using the squirt-patchy theory derived in Chapter 4 that calculates frequency-dependent elastic constants. Jin et al. (2017) proposed a method to incorporate frequency-dependent reflectivity into convolutional modelling for the calculation of synthetic angle-domain seismic traces. Following Jin et al. (2017), I model the single-interface seismic traces in the angle- and azimuth- time domain according to the equation

$$x(\theta, \phi, t) = \mathscr{F}^{-1}\left[W(\omega) R(\theta, \phi, \omega)\right] \tag{6.21}$$

where $W(\omega)$ is the source wavelet $w(t)$ in frequency domain, $R(\theta, \phi, \omega)$ is the frequency-dependent reflection coefficient at the interface, and $\mathscr{F}^{-1}$ denotes the inverse Fourier transform.

6.3 Frequency-dependent azimuthal AVO

I now study the effect of FDA on azimuthal P-wave reflection by considering the Class I example of Rutherford and Williams (1989). Table 6.1 displays the parameters for the model, which consists of a gas sand reservoir overlaid by shale. The sand is saturated by the same fluids (i.e., water and supercritical CO_2) in Table 4.1. The velocities represent the measurements from the unfractured rock. I choose this model because Sayers and Rickett (1997) showed that the fractures have the strongest effect when the sand has higher acoustic impedance than the overlying shale. They investigated the azimuthal variation of AVO response based on this model by introducing anisotropy in the sand while assuming the shale being isotropic. They characterized the fractures by using the normal

and tangential compliances Z_N and Z_T (Schoenberg and Sayers, 1995), which allowed the calculation of frequency-independent reflectivity parallel and perpendicular to the strike of fractures. The results suggested that the effect of fractures on the top sand reflection only becomes noticeable at very large angles.

Table 6.1: The modified Class I model of Rutherford and Williams (1989) characterized by Thomsen's parameters and the squirt-patchy model in this work.

<table>
<tr><td rowspan="2">Layers</td><td rowspan="2">V_P (m/s)</td><td rowspan="2">V_S (m/s)</td><td rowspan="2">Density (Kg/m^3)</td><td rowspan="2">Elasticity</td><td colspan="4">Models</td></tr>
<tr><td colspan="4">Thomsen's parameters (VTI)</td></tr>
<tr><td rowspan="2">Shale</td><td rowspan="2">3300</td><td rowspan="2">1700</td><td rowspan="2">2350</td><td rowspan="2">Elastic</td><td colspan="2">$\epsilon = 0.1$</td><td colspan="2">(a) $\delta = 0.1$
(b) $\delta = -0.1$</td></tr>
<tr><td rowspan="3">Sand</td><td rowspan="3">4200</td><td rowspan="3">2700</td><td rowspan="3">2490</td><td rowspan="3">(a) Elastic
(b) Dispersive</td><td colspan="4">Squirt-patchy model (HTI)</td></tr>
<tr><td>Porosity</td><td>Crack density</td><td>Fracture density</td><td>Fracture length (m)</td></tr>
<tr><td>10%</td><td>0.1</td><td>0.05</td><td>1</td></tr>
</table>

In reality, shale often shows intrinsic anisotropy due to preferentially alignment of clay particles. It is also known that the presence of large fractures in a reservoir often leads to FDA. Under these circumstances, I consider scenarios where the elastic shale is transversely isotropic with vertical axis of symmetry (VTI) and the dispersive sand has vertically aligned fractures which show transverse isotropy with horizontal axis of symmetry (HTI). I use Thomsen's parameters ϵ and δ to characterize the VTI shale and use the squirt-patchy model to describe frequency-dependence of the HTI sand. Figure 6.1 shows the effects of VTI in the overlying shale on elastic azimuthal AVO curves under various Thomsen's parameters. Both shale and sand are assumed to be elastic. The blue solid curves represent the results for the isotropic overlying shale, which are consistent with Sayers and Rickett (1997). In the following studies, I characterize the VTI shale by using two sets of Thomsen's parameters $\epsilon = 0.1; \delta = 0.1$ and $\epsilon = 0.1; \delta = -0.1$ respectively and compare to the results based on the isotropic shale assumption.

The approach of calculating reflection coefficient from Zoeppritz equations and the squirt-patchy theory allows the parameterisation of fracture density and fracture length. In current literature (e.g., Chapman, 2003), the timescale parameter τ was used as 2×10^{-5}, which corresponds to a characteristic frequency $\omega_0 = 5\times10^4$ Hz. Assuming the grain size $\varsigma = 2 \times 10^{-4}$ m and the fracture size $a_f = 1$ m, the fracture-scale characteristic frequency

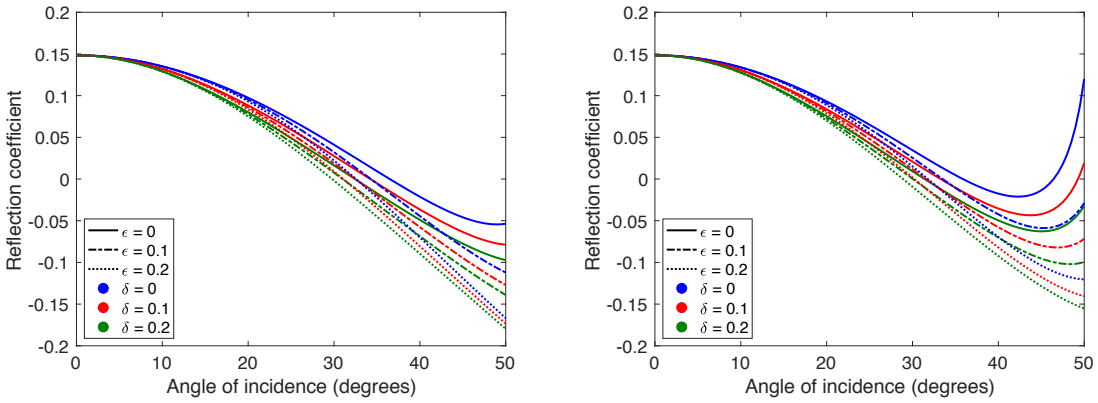

(a) 0-degree azimuth (b) 90-degree azimuth

Figure 6.1: Azimuthal AVO responses at an interface separated by VTI shale and HTI sand for a range of Thomsen's parameters. (a) The azimuth is 0 degree; (b) The azimuth is 90 degrees.

$\omega_0{}'$ is calculated as 10 Hz. I would therefore expect velocity dispersion to occur within the seismic frequency range in the presence of large fractures. The squirt-patchy theory also suggests that the fracture length plays an important role in controlling the range where dispersion occurs. Figure 6.2 demonstrates this effect on frequency-dependent P-wave reflection by varying the fracture length in the sand from 0.1 mm to 10 m. The P-wave reflection is calculated at the incidence angle of 45 degrees and azimuth of 0 degree. For grain-scale microcracks (e.g., 1 mm), there is no dispersion in the seismic frequency range, and the fractured gas sand is equivalent to the elastic medium considered by Sayers and Rickett (1997). For large-scale fractures (e.g., 1 m), the gas sand exhibits strong FDA in the seismic frequency range.

To demonstrate the azimuthal dependence of P-wave reflections, I first consider the case where the fractured sand is elastic (i.e., the frequency-independent micro-scale crack case). Figure 6.3 displays the influence of VTI anisotropy in the overlying shale to the AVO responses for acquisitions with azimuth varying from 0 to 90 degrees. In the case of isotropic shale, the results are consistent with Sayers and Rickett (1997), where polarity changes of reflection occur at certain angles of incidence which are often refered to as reversal angles. The amplitude of reflectivity becomes zero and the phase jumps between 0 degree and 180 degrees discontinuously at the reversal point. The introduction of VTI influences the dependence of reflectivity on the angle of incidence (Rüger, 1997;

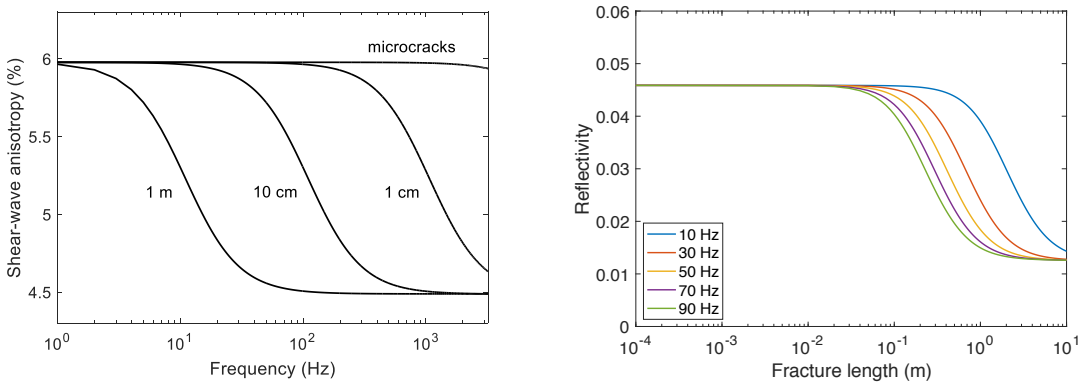

(a) (b)

Figure 6.2: The influence of fracture length to frequency-dependent anisotropy. (a) Shear-wave anisotropy as a function of frequency for various fracture sizes. The propagation is 75 degrees to the fracture normal. (b) P-wave reflectivity as a function of fracture size for various frequencies. The angle of incidence is 45 degrees and the propagation is perpendicular to fractures.

Tsvankin, 2001). Figure 6.3b compares the AVO responses at zero azimuth for various Thomsen's parameters of the shale. The presence of VTI anisotropy changes both reversal angles and the far-offset reflectivities. Such difference can be well illustrated by the corresponding angle-domain seismic traces in Figure 6.6a where the source is a Ricker wavelet with 40 Hz peak frequency. The red line represents the location of the interface. Although VTI does not give rise to azimuthal anisotropy in the overlying shale, its effect on angle dependence could further affect the azimuthal anisotropy of AVO responses at the VTI-HTI interface. As a result, the multiple polarity changes may no longer be observed as the azimuthal angle increases (Figure 6.3c). Although my results in Figure 6.3a agree with Sayers and Rickett (1997) in that the azimuthal anisotropy only become noticeable at very large angles, the presence of VTI in the overlying shale could lead to a much weaker azimuthal variation of reflectivity compared to results based on the isotropic shale assumption (Figures 6.3d and 6.3e).

I now investigate the effects of frequency-dependence in the HTI sand on the azimuthal AVO responses. Both isotropic and VTI overlying shales are considered. Figure 6.4 displays the variation of P-P reflectivity, which is the norm of the complex-valued reflection coefficient, with angle of incidence and azimuth at various frequencies. Again, significant azimuthal effects only occur at large angles of incidence. In the isotropic and

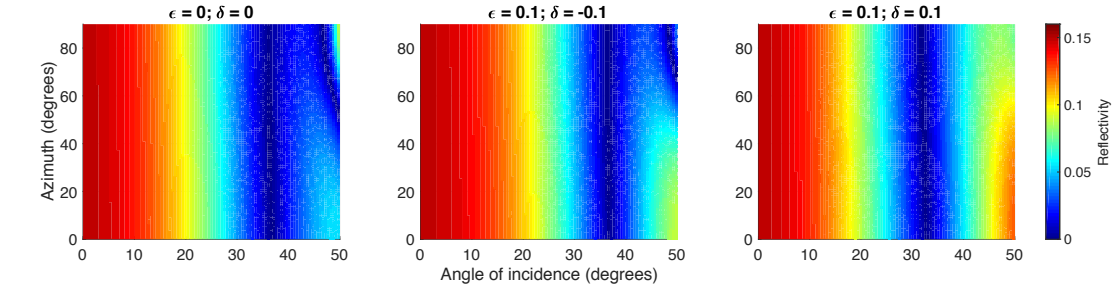

(a)

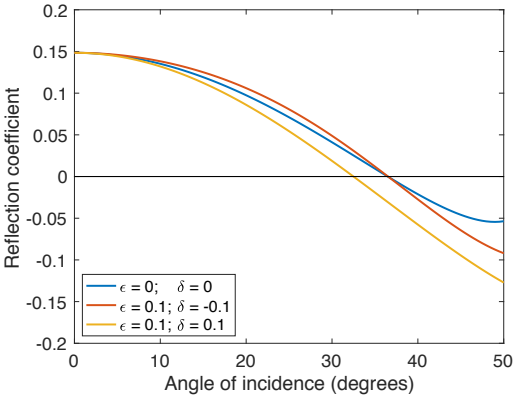

(b) 0-degree azimuth

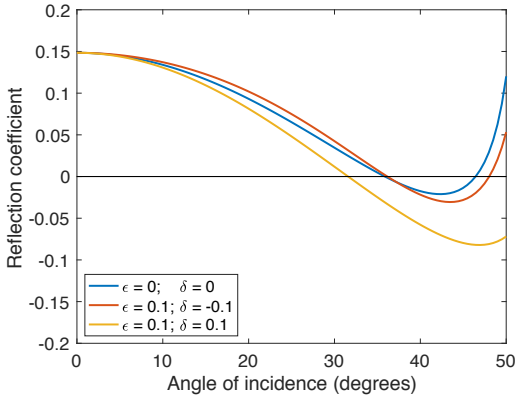

(c) 90-degree azimuth

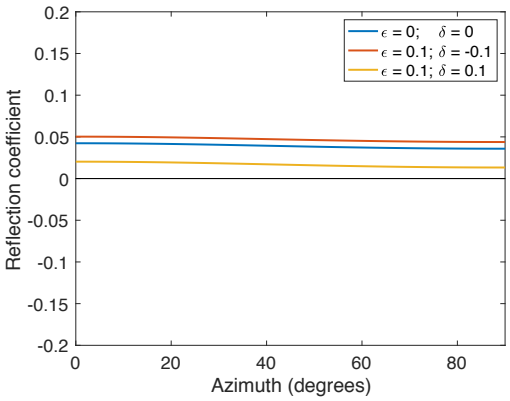

(d) 30-degree angle

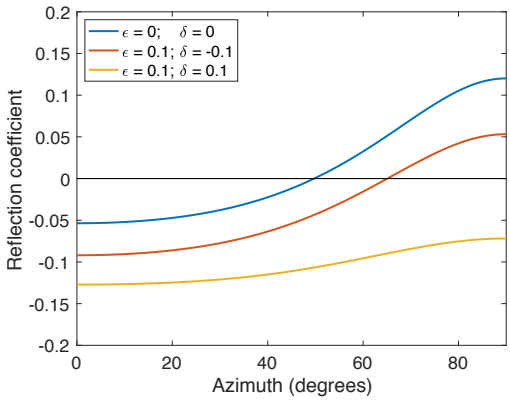

(e) 50-degree angle

Figure 6.3: (a) The variation of P-P reflectivity with angle of incidence and azimuth from the top of sand for a range of Thomsen's parameters of the VTI shale; (b) The variation of reflection coefficient with angle of incidence at 0-degree azimuth; (c) The variation of reflection coefficient with angle of incidence at 90-degree azimuth; (d) The variation of reflection coefficient with azimuth at 30-degree angle; (e) The variation of reflection coefficient with azimuth at 30-degree angle. The HTI sand is frequency independent.

VTI ($\epsilon = 0.1; \delta = -0.1$) shale cases shown in Figures 6.5a and 6.5b, the reflectivities at various frequencies do not reduce to zero, and the phase variations appear to be continuous. The corresponding pre-stack seismic traces therefore show strong phase variations with the increase of incidence angle (Figure 6.6b). The influence of dispersion is negli-

gible at small angles. For angles larger than 30 degrees, a more gradual variation in both amplitude and phase can be observed from the frequency-dependent case. In comparison to results shown in Figures 6.5a and 6.5b, phase variation in the VTI ($\epsilon = 0.1; \delta = 0.1$) case (Figure 6.5c) becomes less significant at large angles, as one can hardly observe noticeable phase effects on the seismic traces shown in the bottom of Figure 6.6b.

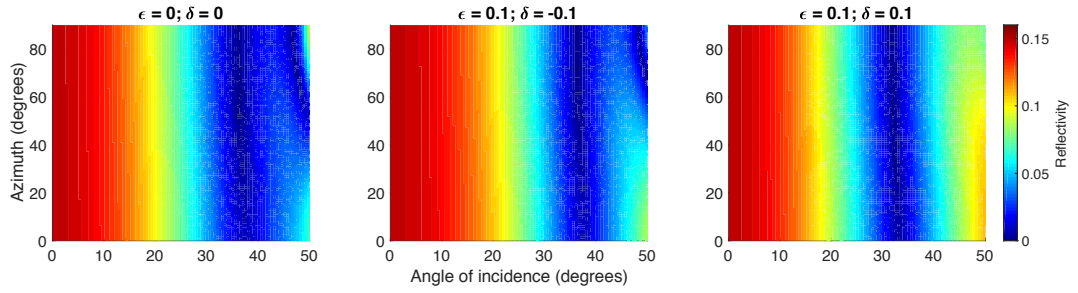

(a) 10 Hz

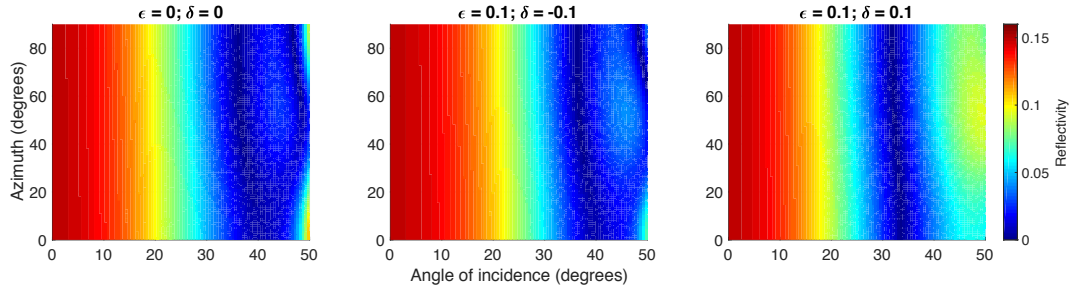

(b) 50 Hz

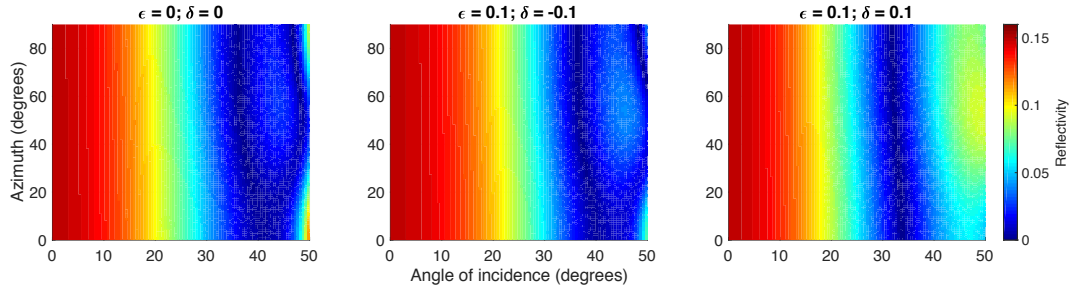

(c) 90 Hz

Figure 6.4: The variation of P-P reflectivity with angle of incidence and azimuth at the interface separated by VTI shale and frequency-dependent HTI sand for a range of frequencies at (a) 10 Hz (b) 50 HZ and (c) 90 Hz.

Since the azimuthal variation becomes obvious only when the angle of incidence is large, now I take the angle as 50 degrees and demonstrate the elastic and frequency-dependent behaviours of P wave reflections as a function of azimuth in Figure 6.7. In the frequency-independent case (Figure 6.3a), polarity change occurs at the reversal azimuth where the amplitude reduces to zero and the phase jumps from 180 degrees to 0 degree.

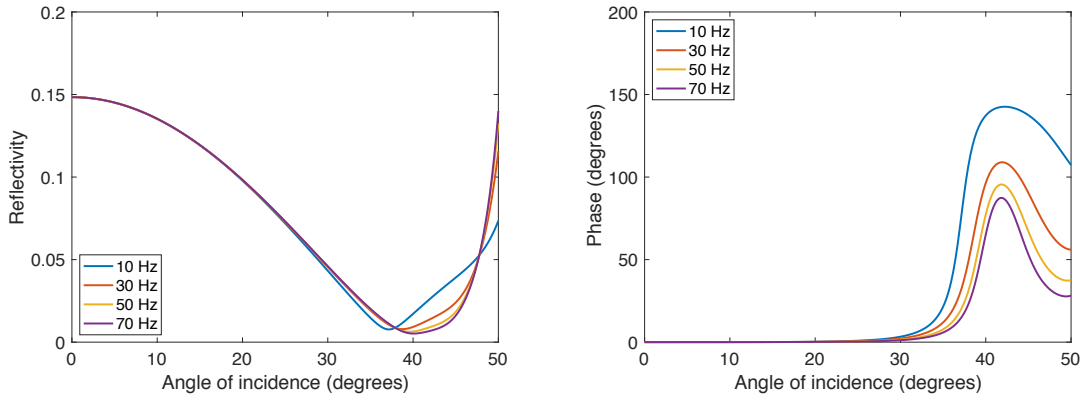

(a) isotropic ($\epsilon = 0; \delta = 0$) shale

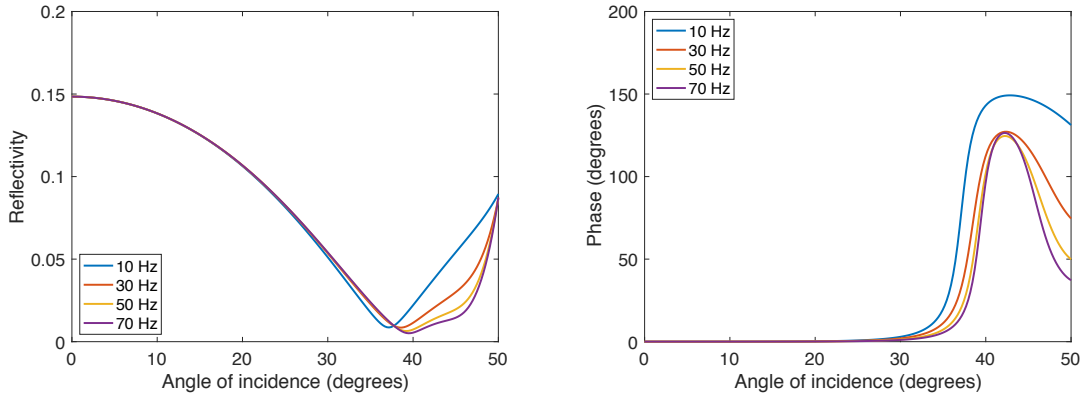

(b) VTI ($\epsilon = 0.1; \delta = -0.1$) shale

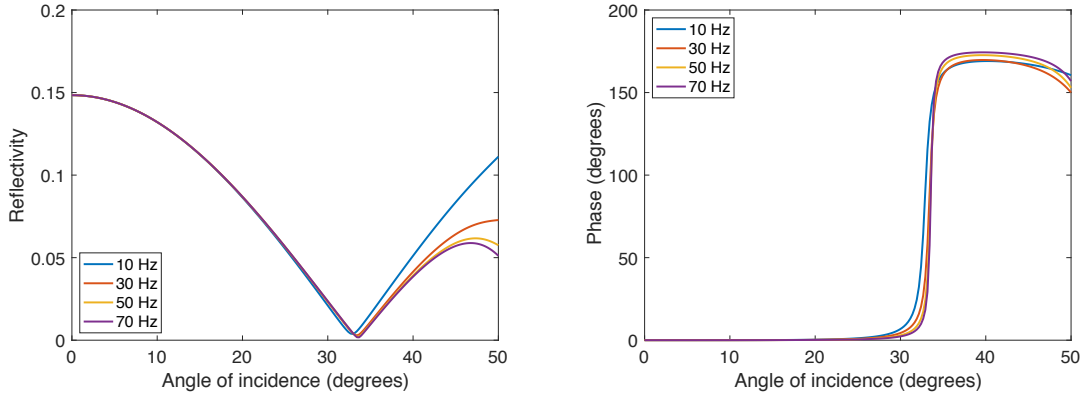

(c) VTI ($\epsilon = 0.1; \delta = 0.1$) shale

Figure 6.5: The frequency-dependent AVO curves and phase variations from acquisition perpendicular to fractures (zero azimuth) for (a) the isotropic shale case with $\epsilon = 0; \delta = 0$; (b) the VTI shale case with $\epsilon = 0.1; \delta = -0.1$; (c) the VTI shale case with $\epsilon = 0.1; \delta = 0.1$.

The introduction of dispersion leads to different behaviours regarding to phase reversal as Figures 6.7a and 6.7b demonstrate that the frequency-dependent reflection coefficient becomes non-zero and the phase varies continuously. Seismic dispersion is strong at small azimuths and becomes much weaker as the propagation approaches the direction parallel

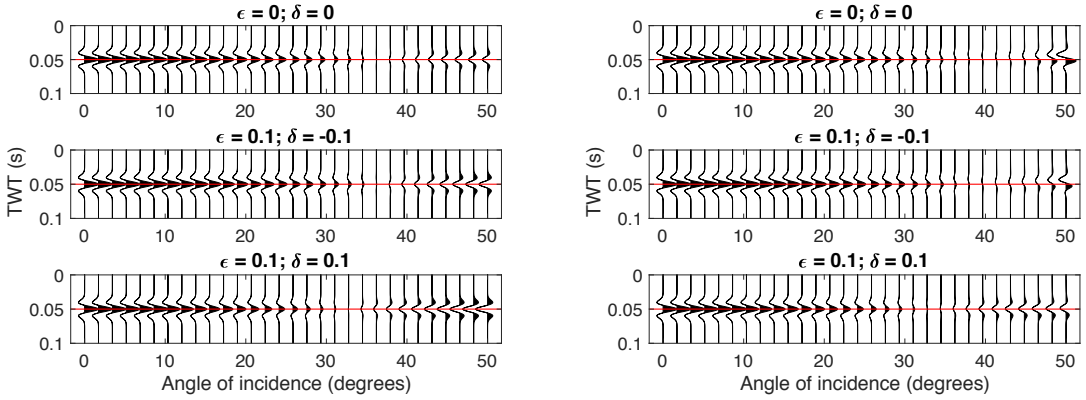

(a) elastic case

(b) frequency-dependent case

Figure 6.6: The pre-stack angle domain seismic traces from acquisition perpendicular to fractures (zero azimuth) for (a) the frequency-independent HTI sand overlaid by VTI shale and (b) the frequency-dependent HTI sand overlaid by VTI shale. Various Thomsen's parameters are used to characterize the VTI shale. The red line represents the location of the interface.

to fractures. This effect is clearly illustrated by comparing the azimuth-domain waveforms in Figures 6.8a and 6.8b. FDA plays an important role in reshaping the reflected waveforms in terms of amplitude and phase, and this phenomenon is particularly obvious for azimuth angles smaller than 60 degrees in this example.

I now consider the VTI shale being characterized by $\epsilon = 0.1; \delta = 0.1$. The reflectivity curves are shown in Figure 6.7c. In this case, polarity change can no longer be observed as the reflections are negative for all azimuths. The introduction of seismic dispersion in the HTI sand leads to weaker amplitudes of reflected waves (comparing Figures 6.8a and 6.8b), but minimal phase effects can be expected on the reflected waveforms as suggested by the phase curves in Figure 6.7c. The presence of VTI in the overlying shale could therefore significantly change the azimuthal behaviour of frequency-dependent AVO responses in terms of both amplitude and phase variations.

I further investigate the potential impacts of azimuthal phase effects on amplitude and apparent arrival time. I do this by considering the VTI shale case with $\epsilon = 0.1; \delta = -0.1$ where phase reversal occurs. Figure 6.9 displays the amplitude picking results. For the elastic case in Figure 6.9a, the picked amplitude at each azimuth fits well with the reflection coefficient curve, and clearly approaches zero when the azimuth is around 60 degrees. For the frequency-dependent case in Figure 6.9b, the amplitudes vary more gradually and

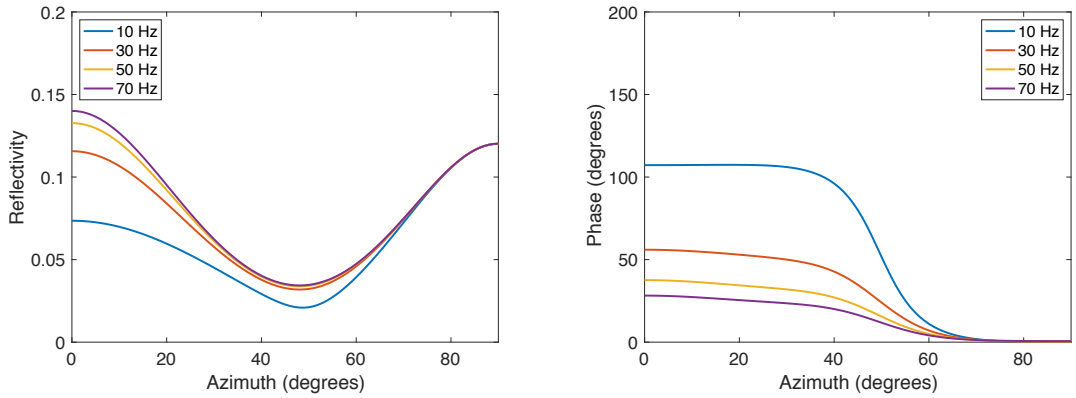

(a) isotropic ($\epsilon = 0; \delta = 0$) shale

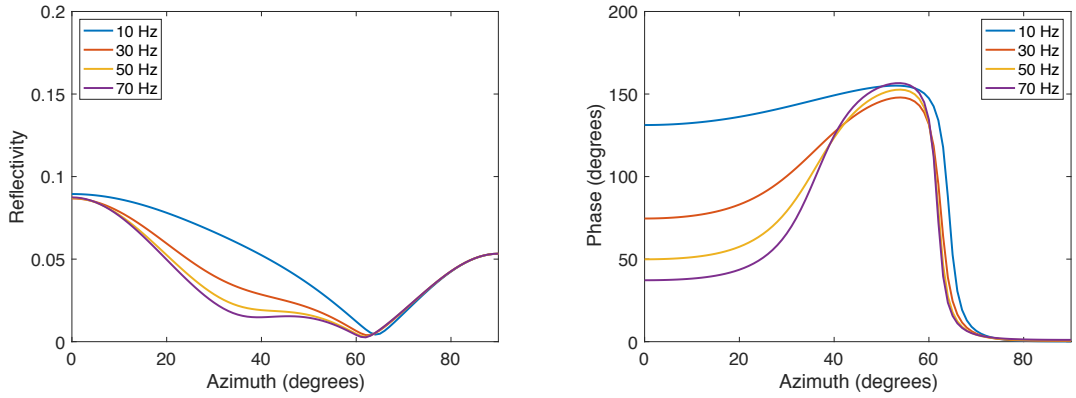

(b) VTI ($\epsilon = 0.1; \delta = -0.1$) shale

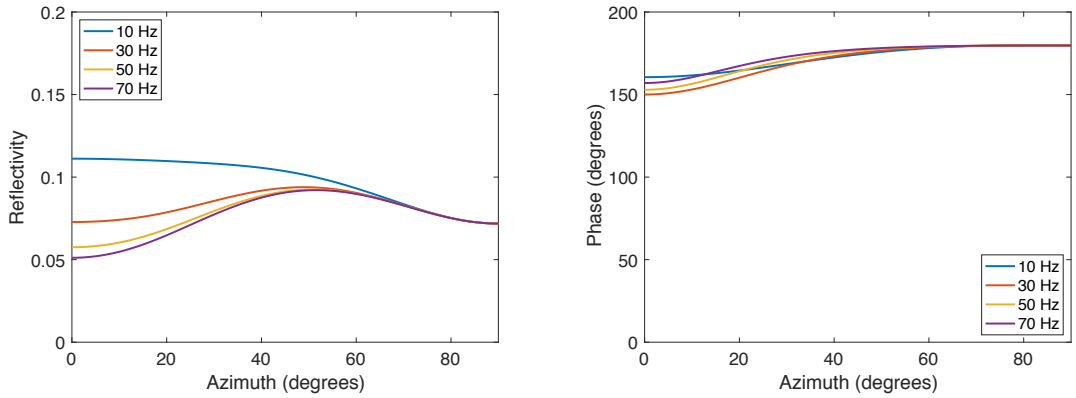

(c) VTI ($\epsilon = 0.1; \delta = 0.1$) shale

Figure 6.7: The frequency-dependent variation of top sand reflectivities and phases with azimuth at 50-degree angle of incidence for (a) the isotropic shale case with $\epsilon = 0; \delta = 0$; (b) the VTI shale case with $\epsilon = 0.1; \delta = -0.1$; (c) the VTI shale case with $\epsilon = 0.1; \delta = 0.1$.

never reduce to zero. They are approximately proportional to the reflection coefficients at the peak frequency. In the elastic case, the peak locates exactly in the horizon, while in the FDA case there is a difference which I refer to as the apparent azimuthal residual. Figure 6.10 shows this apparent azimuthal residual between the time depths of the wave-

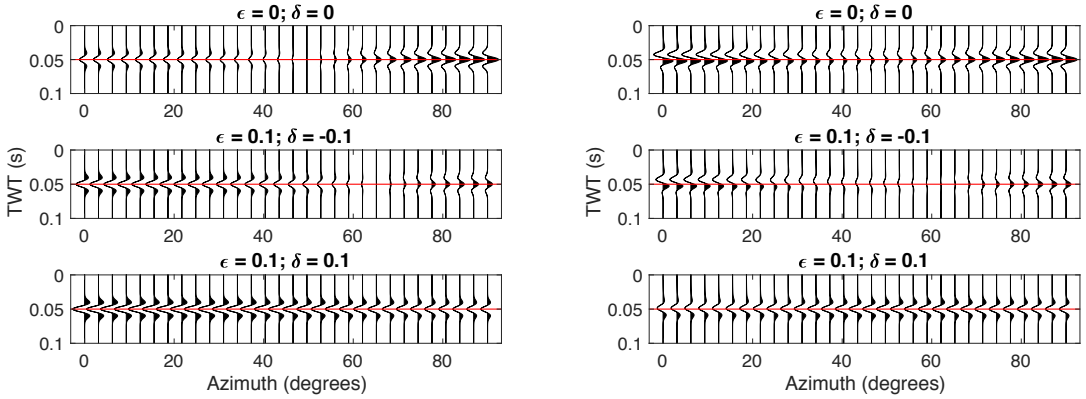

(a) elastic case (b) frequency-dependent case

Figure 6.8: The azimuth domain seismic traces from acquisition at 50-degree angle of incidence for (a) the frequency-independent HTI sand overlaid by VTI shale and (b) the frequency-dependent HTI sand overlaid by VTI shale. Various Thomsen's parameters are used to characterize the VTI shale. The first and second horizons represent the top and base sand reflections, respectively.

form peak and the true horizon. I note that failure to recognize this effect during velocity analysis could potentially give rise to incorrect estimate of azimuthal velocity variations.

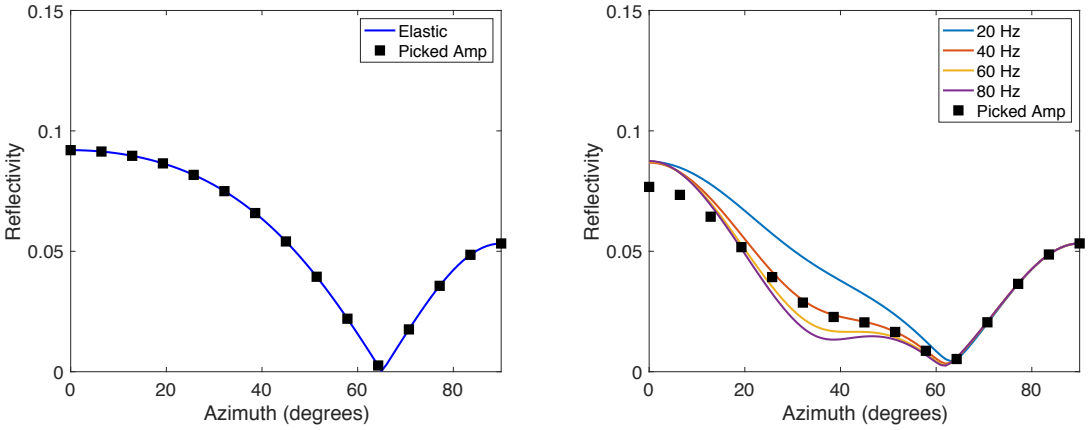

(a) elastic case (b) frequency-dependent case

Figure 6.9: The amplitude picking of azimuth-domain seismic traces for (a) the elastic case and (b) the frequency-dependent case. The overlying VTI shale is characterized by $\epsilon = 0.1; \delta = -0.1$. The angle of incidence is 50 degrees. Curves represent the reflection coefficients. Squares represent the picked amplitudes.

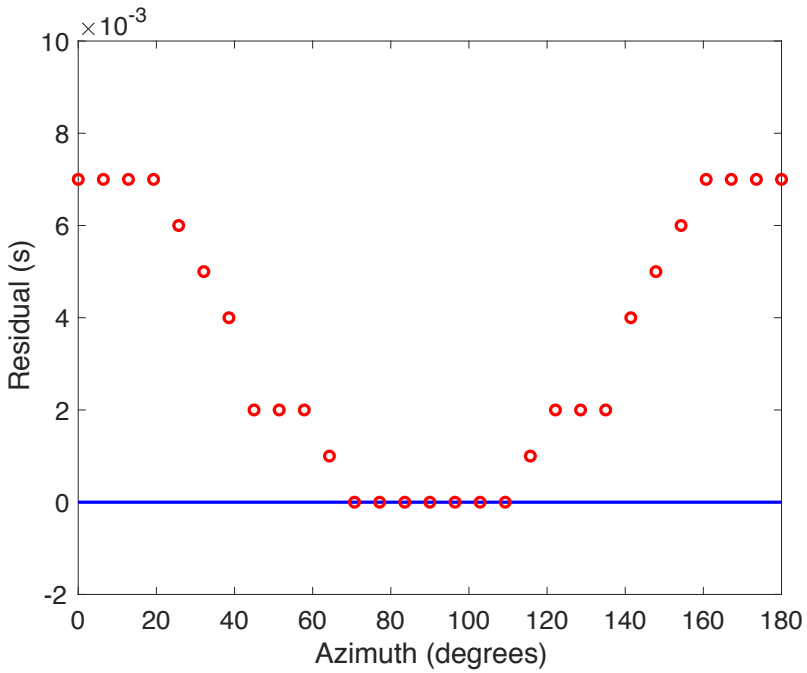

Figure 6.10: The variation of traveltime residual with azimuth for the seismic traces shown in Figure 6.8b ($\epsilon = 0.1; \delta = -0.1$). The blue line indicates the residual for the elastic case. The red circle represents the residual for the frequency-dependent case.

6.4 Bayesian inversion for fluid and fracture properties

Bayesian inversion has been widely used for estimating rock properties from seismic data (Mavko and Mukerji, 1998b; Spikes et al., 2007; Wu et al., 2014). Jin et al. (2017) proposed a Bayesian scheme aimed at recovering water saturation from pre-stack seismic data using a modelling technique that incorporates frequency-dependent reflection coefficients. In this paper, I extend previous technique to the anisotropic case with a particular focus on the estimation of water saturation, fracture density, and fracture length. I consider a single interface example with the upper layer being VTI shale and the lower layer being a partially saturated sand with aligned vertical fractures. Based on the inversion scheme proposed by Jin et al. (2017), the main steps in this study are as follows:

(i) Forward modelling the seismic trace $f\left(S_w, \varepsilon_f, a_f\right)$, as written from equation 6.21, for various values of water saturation S_w, fracture density ε_f and fracture length a_f by assuming all other background parameters are known.

(ii) Calculating the misfits between the observed data d (pre-stack seismic traces) and

the forward model responses at $\left(S_w, \varepsilon_f, a_f\right)$ by using equation

$$\Delta E = \sum \left\| d - f\left(S_w, \varepsilon_f, a_f\right) \right\|_2 \tag{6.22}$$

which is the L_2 norm of the error between data and forward modelling predictions.

(iii) Calculating the likelihood function $P\left(d|S_w, \varepsilon_f, a_f\right)$ from exponentially transforming the misfit:

$$P\left(d|S_w, \varepsilon_f, a_f\right) \propto \exp\left(-b \cdot \Delta E\right) \tag{6.23}$$

where b is a constant, the determination of which has been discussed by Jin et al. (2017). In this study, I choose value of 20 for illustration purposes.

(iv) Obtaining prior information $P\left(S_w, \varepsilon_f, a_f\right)$ from well-log analysis, and the posterior probability of inversion targets S_w, ε_f and a_f can be calculated by

$$P\left(S_w, \varepsilon_f, a_f|d\right) = \frac{P\left(d|S_w, \varepsilon_f, a_f\right) P\left(S_w, \varepsilon_f, a_f\right)}{P\left(d\right)} \tag{6.24}$$

where $P\left(d\right)$ is a constant that normalizes the final results.

I use same parameters in Table 6.1 to perform a synthetic study. The overlying VTI shale is characterized by Thomsen's parameters $\epsilon = 0.1$ and $\delta = -0.1$. The HTI sand is saturated by 60% water and 40% CO_2, and the patch parameter q is assumed to be $10q_0$. I consider two fracture cases with the same density 0.05 but different sizes, i.e., grain-scale with length of 1 mm and meso-scale with length of 1 m. Figure 6.11 shows the pre-stack data in both angle and azimuth domain with 10% Gaussian noise added to the synthetic seismic traces computed by equation 6.21.

Following the above steps, I first derive the forward seismic model as a function of S_w, ε_f, and a_f assuming that all other parameters are known. The likelihood function can then be obtained from the misfits between the observed data and model responses by scanning through the combinations of S_w, ε_f, and a_f using equation 6.22. As for a synthetic study, I only assume the prior probability distribution $P\left(S_w, \varepsilon_f, a_f\right)$ being constant within certain bounds, i.e., $S_w \in [0, 1]$, $\varepsilon_f \in [0, 0.1]$ and $a_f \in \left[10^{-4}, 10^{1}\right]$. In a real application, the prior

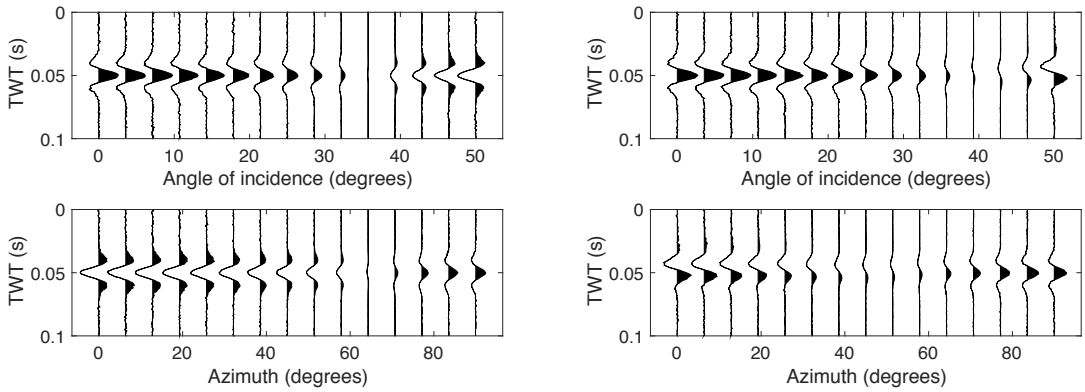

(a) micro-scale case

(b) meso-scale case

Figure 6.11: Synthetic angle- and azimuth-domain seismic data for (a) the micro-scale crack case and (b) the meso-scale fracture case. For the angle-domain data, the acquisition is at zero azimuth. For the azimuth-domain data, the angle of incidence is fixed at 50 degrees.

probability distribution of these parameters could be obtained from well-log analysis. I can then calculate the posterior probability distribution $P\left(S_w, \varepsilon_f, a_f|d\right)$ from equation 6.24.

Figure 6.12 displays the marginal distribution of the posterior probability $P\left(S_w, \varepsilon_f, a_f|d\right)$ for the grain-scale crack and large-scale fracture cases, respectively. For a given probability distribution $P(x, y, z)$, the marginal probability distribution of each variable is calculated by

$$P_m(x) = \sum_{y,z} P(x, y, z) \tag{6.25}$$

$$P_m(y) = \sum_{x,z} P(x, y, z) \tag{6.26}$$

$$P_m(z) = \sum_{x,y} P(x, y, z)\,. \tag{6.27}$$

It is clear that these two cases can be well distinguished. The fracture length for the large-scale case is accurately recovered, while a range of lengths smaller than 1 cm appear to satisfy the micro-scale case. This is because seismic dispersion is controlled by the fracture size, and could be negligible as the size approaches grain-scale. The effects of seismic dispersion associated with large-scale fractures also contribute to an accurate estimation of water saturation and fracture density. However, for the micro-scale crack

case where seismic dispersion is negligible, it is unlikely to accurately recover the water saturation. Figure 6.13 shows the estimation of S_w and a_f at fixed $\varepsilon_f = 0.05$. The results demonstrate that a more accurate estimation of water saturation can be achieved if the model can be effectively constrained. The consideration of seismic dispersion in azimuthal AVO analysis has therefore shown potential of discriminating large-scale fractures from micro-scale cracks.

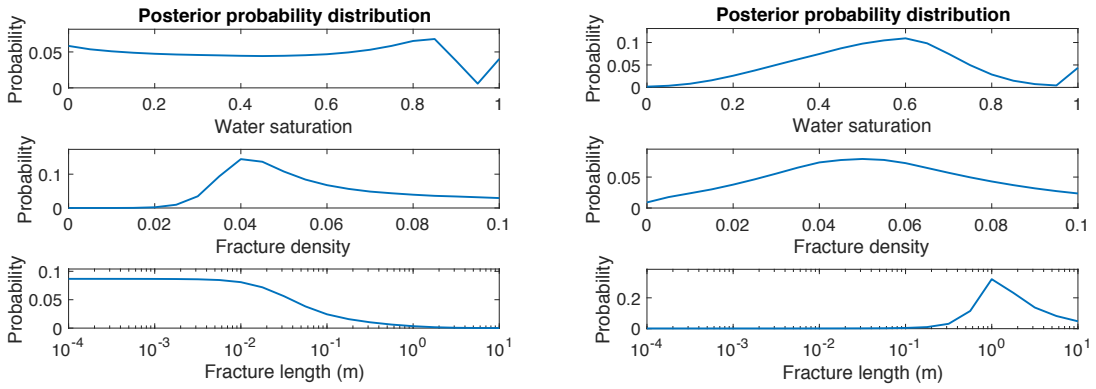

(a) micro-scale case (b) meso-scale case

Figure 6.12: Marginal distribution of the posterior probability for water saturation, fracture density, and fracture length, respectively. (a) The microcrack case with true fracture length 1 mm; (b) The large-scale fracture case with true fracture length 1 m.

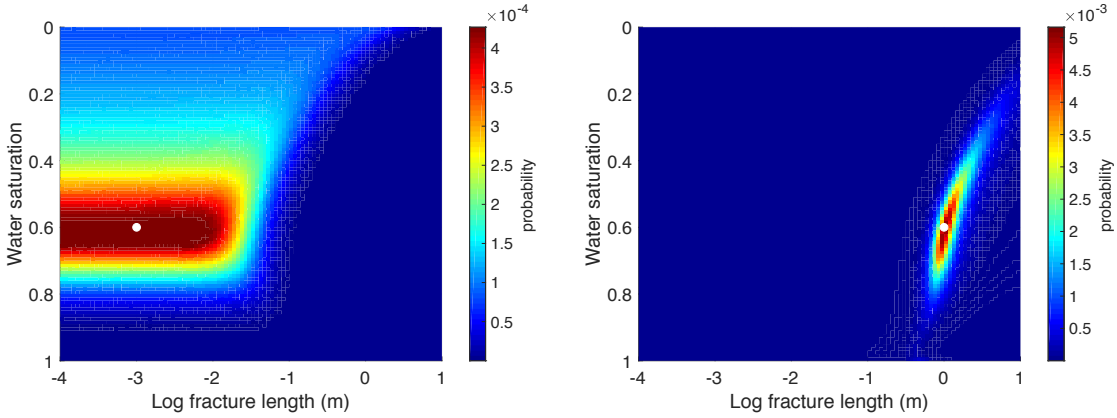

(a) micro-scale case (b) meso-scale case

Figure 6.13: The estimation of water saturation and fracture length based on the fracture density being determined as 0.05. (a) The microcrack case; (b) The large-scale fracture case. The true fracture length and water saturation is marked with white circle.

6.5 Conclusions

I have studied the effect of frequency-dependent anisotropy on azimuthal AVO response in a fractured Class I HTI sand overlaid by VTI shale. For acquisitions perpendicular to fractures, the frequency-dependent AVO behaviour shows a gradual continuous phase variation in contrast to the discontinuous phase reversal from the elastic case. The principal qualitative difference between frequency-dependent and frequency-independent responses lies in the azimuthal phase variation at wide angles of incidence. Such difference is visible on the synthetic seismograms calculated from a generalised convolutional modelling. I show modest effects on the picked amplitude but large effects on the apparent azimuthal traveltime residual. Failure to recognize this effect during velocity analysis could potentially give rise to incorrect estimate of azimuthal velocity variations. Fracture-induced dispersion influences both amplitude and phase variations of the P-wave reflections, leading to the possibility of using frequency-dependent azimuthal AVO to distinguish between micro-cracks and large-scale fractures.

Chapter 7

Conclusions and discussion

7.1 Conclusions

The aim of this thesis has been to improve our understanding of multiphase fluid effects on the anisotropic wave response of reservoirs containing fractures. To achieve this aim, I developed a new theoretical model calculating elastic moduli of a fractured rock saturated by two immiscible fluids. The theory was tested against newly published laboratory data. Based on the theory, I showed how seismic anisotropy of partially saturated rocks could be influenced by coupled patch and squirt effects, and also investigated the potential use of these effects for estimating fluid and fracture properties from seismic data. The main conclusions of the thesis are summarized below.

Seismic wave propagation through fractured rocks is greatly influenced by the distribution of fractures and the fluid content occupying the pore space. In Chapter 4, I derive expressions for the anisotropic frequency-dependent elastic constants by incorporating the relative mobilities of the saturating fluids and the coupled impact of squirt and patch effects. Fluid mobility can be lower in partially saturated rocks compared to the fully saturated case due to the presence of patchy saturation and relative permeability, and this can lead to a stiffening which dominates compressibility effects.

Such lowering effect on fluid mobility could lead to non-monotonic behaviour of SWS and even P-wave velocities with respect to changes in water saturation, complicating attempts to invert saturation from seismic data. While the squirt and patch effects on shear

properties are weaker than that on bulk properties, the impact on SWS in fractured rocks is potentially significant. Patchy saturation tends to reduce SWS due to its effect on lowering the characteristic frequency at intermediate saturations. Testing the theory against laboratory measurements suggests that both squirt and patchy mechanisms are significant for describing seismic anisotropy in partially saturated fractured rock.

The impact of fluid and aligned fractures on seismic anisotropy leads to the potential of using azimuthal P-wave reflections for the discrimination between micro-scale and large-scale fractures. This has been investigated through frequency-dependent azimuthal AVO responses of a Class I HTI sand model overlaid by VTI shale. Although VTI in the overburden does not lead to azimuthal anisotropy, its effect on angle dependence could significantly affect azimuthal AVO behaviours at far offsets. I show a modest effect on the amplitude and large effect on the phase, the latter of which could even be mistaken for azimuthal velocity variations. A convolutional modelling technique incorporating frequency-dependent azimuthal effects has been developed to calculate synthetic seismograms based on the derived squirt-patchy theory. The forward modelling can be used as a basis in a Bayesian scheme for inverting water saturation, fracture density and fracture length of a partially saturated fractured reservoir.

7.2 Discussion and future work

In this thesis I have studied frequency-dependent anisotropy in a fractured rock saturated by two fluids through the derivation of frequency-dependent elastic constants. The model derived in Chapter 4 shows that seismic anisotropy is sensitive to fluid through coupled effects from squirt and patch mechanisms.

The derivation is based on the model of Chapman (2003), in which the elastic constants are calculated through the theoretical framework of Eshelby (1957). This results in the theory being limited to dilute pore concentrations (low porosity). Jakobsen et al. (2003) proposed a model using the T-matrix approach that allows for non-dilute concentrations of inclusions. Jakobsen and Chapman (2009) further combined both global flow and squirt flow in a unified theory. It is worth mentioning that the squirt-patchy theory de-

rived in Chapter 4 could be generalized to incorporate global flow following the strategy of Jakobsen and Chapman (2009), which will be addressed in future research.

There are various approaches to modelling patchy saturation. White (1975) described fluid heterogeneity by introducing gas-filled spherical pockets in a water saturated porous rock. Later authors have discussed the 'bubble' effect on velocity dispersion and attenuation (e.g., Dutta and Odé, 1979; Carcione et al., 2003; Quintal et al., 2008). Johnson (2001) proposed a Biot-based theory by considering two geometrical parameters that would potentially allow us to deduce the effective sizes and shapes of the patches. Toms et al. (2007) proposed a model that considers randomly distributed fluid patches in 3D space, and discussed how the distribution of shapes and sizes of the fluid patches would affect dispersion and attenuation.

Alternatively, I model patch effects using a non-dimensional parameter q rather than considering any geometrical distribution. Since q quantifies the pressure variation between two fluids, it is likely to be related to wetting phenomenon such as capillary pressure, and so could vary as a function of saturation. In current literature, the physical mechanism behind q remains unclear and no explicit modelling of its dependence on saturation has been investigated. In future study, controlled laboratory experiments on fractured rocks saturated by various fluids could potentially provide physical insight into the understanding of the patch parameter q.

The use of q is a simple approach that allows us to describe the multi-fluid saturated rock through a unified model in which the squirt-flow mechanism, the uneven fluid pressures, and the relative permeability effects are incorporated. Previous idea of modelling velocity dispersion in partially saturated rocks uses the effective fluid approach combined with the single-fluid squirt theory (Amalokwu et al., 2014). In this thesis, my modelling approach explicitly describes the two-phase fluid effects through the calculation of elastic constants. I emphasize the importance of the relative permeability effect as it affects the effective fluid mobility and the characteristic frequency in a way that could lead to non-monotonic variations of shear modulus, SWS and P-wave velocities with changing water saturation.

The relative permeability model considered in this thesis is only assumed to be a function of fluid saturation. Besides, the absolute permeability is also assumed to be isotropic, despite the fact that the fractured medium is anisotropic. Ali and Jakobsen (2011) studied the influence of mesoscopic fractures on anisotropic permeability. Dmitriev and Maksimov (1998) and Dmitriyev and Maksimov (2001) suggested that relative permeability in anisotropic media depends not only on fluid saturation, but also on the direction of fluid flow. Maksimov and Dmitriev (2013) discussed the use of an anisotropic relative permeability tensor for the description of simultaneous flow of two immiscible fluids in anisotropic porous media. In the future, it would therefore be interesting to incorporate anisotropic tensors of both the absolute and relative permeabilities for a more accurate description of multiphase fluid effects in anisotropic media.

In Chapter 5, I have demonstrated that the theory can be conveniently used for explaining laboratory measurements of SWS and P-wave anisotropy in synthetic fractured rocks that are partially saturated by water/air (Amalokwu et al., 2014, 2015) and brine/CO_2 (Falcon-Suarez et al., 2019). Amalokwu et al. (2014) and Amalokwu et al. (2015) attempted to interpret their observations by using White's model to estimate an effective fluid modulus that accounts for the patch-related dispersion. This effective modulus was then used as an input to the model of Chapman (2003) to include squirt-flow effects. In my modelling approach, a good fit can only be achieved at an intermediate q value with the frequency falling in the dispersive range. This confirmed the conclusions of Amalokwu et al. (2014) and Amalokwu et al. (2015) that both patch and squirt mechanisms are required to fit laboratory observations of seismic anisotropy.

The squirt-patchy theory predicts a potential non-monotonic variation of both P- and S-wave anisotropy with water saturation if the relative permeability and patchy effects become significant. Such behaviour related to P-waves has been observed by Falcon-Suarez et al. (2019) as their experimental results show a slight increase in P-wave velocity at low CO_2 saturations. This agrees with my modelling results in Figure 5.14 at high frequencies considering both patchy and relative permeability effects. Such behaviour related to S-waves, however, has not been observed in their experiment. This could be

due to the measurement frequency being much higher than the fracture-scale characteristic frequency. Future laboratory measurements at lower frequencies would therefore be worth carrying out in order to validate the theory derived in this thesis.

Previous work by Chapman (2003) has shown that meso-scale fractures could lead to dispersion and attenuation in the seismic frequency band. This is still true for my work, but the situation becomes complicated due to effects of the relative permeability and uneven fluid pressures. Although the frequency-dependent SWS is primarily affected by fracture size a_f, the SWS-a_f relationship is complicated since the characteristic frequency is further influenced by fluid saturation and the patch parameter q.

The potential importance of frequency-dependent anisotropy to seismic fracture characterization is clear. Techniques based on shear-wave splitting have been particularly studied, while less attention has been paid to the impacts of fracture-related dispersion on P-wave reflections. In Chapter 6, I have examined frequency-dependent azimuthal effects on P-wave reflections based on a forward convolutional modelling strategy and the squirt-patchy theory derived in Chapter 4. According to the theory, the frequency regime where the fracture-related dispersion occurs is determined by the length scale of the fractures and the characteristic frequency ω_f, which is closely related to the timescale parameter τ defined by Chapman (2003). The behaviour of seismic dispersion is controlled by the value of τ, the impact of which has been studied by Maultzsch et al. (2003a). In the numerical example (section 6.3), I only choose $\tau = 2 \times 10^{-5}$ as used in Chapman (2003), although other values have also been considered in current literature (e.g., Amalokwu et al., 2016). In a real data application, τ acts as a parameter that has to be calibrated from available wells (Wu et al., 2014).

My theory considers only one set of aligned fractures in an isotropic background, and thus describes the fractured rock as a TI medium. Although considering such a model is simple and sufficient to model azimuthal anisotropy, fractured reservoirs can be orthorhombic and even triclinic in the presence of multiple sets of fractures (Grechka and Kachanov, 2006a,b; Tsvankin and Grechka, 2011), the influence of which on frequency-dependent anisotropy would be worth investigating in future research since a lower sym-

metry could complicate both angle and azimuth dependences of seismic reflections.

The forward modelling method of Jin et al. (2017) presented in section 6.2.2 calculates waveforms only based on frequency-dependent P-P reflection coefficients. The use of such a convolutional model with anisotropic reflectivity to interpret azimuthal amplitude variations is simple and convenient, but potentially problematic. Anisotropy in the overburden can lead to distortions in the amplitudes from transmission, spreading and attenuation (Maultzsch et al., 2003b), and these are not accounted for in the modelling. Methods which can be applied to data to correct for such effects have been discussed by Tsvankin (1995) and Xu and Tsvankin (2006).

The numerical example presented in section 6.3 shows that frequency-dependent effects on azimuthal AVO become significant at wide angles of incidence where azimuthal phase reversal occurs. The variation of amplitude with azimuth does not deviate far from corresponding reflection coefficients calculated from anisotropic Zoeppritz equations, but the phase variation could become obvious as the apparent azimuthal traveltime residuals are non-zero due to the presence of seismic dispersion. This is demonstrated by using only one model in which the overlying VTI shale is characterized by Thomsen's parameters $\epsilon = 0.1; \delta = -0.1$. It should be noted that such azimuthal phase variations should also be expected in other models such as an isotropic overlying shale as long as the phase reversal occurs. Such effects could be mistaken for azimuthal moveout, which may have implications for seismic velocity analysis.

The fracture length in reservoirs is usually several centimetres to meters, which is much larger than the length of the micro-scale cracks. While the inversion for micro-cracks may not be relevant to seismic exploration, I do this in section 6.4 to show the discrimination between these two scales. The study of fracture-induced dispersive effects on AVO responses can be considered as an extension of previous technique by Jin et al. (2017) to anisotropic case. Current inversion scheme by Jin et al. (2017) was based on an idealized forward convolutional modelling and might not be realistic for immediate practical application. Nevertheless, the technique incorporates frequency-dependent reflectivities and could in principle handle more complex models (e.g., multiple layers).

The numerical results indicate potential importance of the concepts to interpretation of azimuthal seismic response in field data, and application to particular datasets will form the focus of future work. Workflows for field data application of isotropic FAVO techniques have been presented by Wu et al. (2014). Robust inversion methods for fracture characterization from seismic reflections would require appropriate regularization strategies which will be addressed in future research.

A key current challenge for geophysicists is to link seismic data to reservoir modelling. In this thesis, I have linked seismic anisotropy to flow parameters in fractured reservoirs containing multiple fluids. I expect future work to focus on exploiting these results to improve the integration between seismology and reservoir engineering.

References

Adelinet, M., J. Fortin, Y. Guéguen, A. Schubnel, and L. Geoffroy, 2010, Frequency and fluid effects on elastic properties of basalt: Experimental investigations: Geophysical Research Letters, **37**.

Agersborg, R., M. Jakobsen, B. Ruud, and T. Johansen, 2007, Effects of pore fluid pressure on the seismic response of a fractured carbonate reservoir: Studia Geophysica et Geodaetica, **51**, 89–118.

Aki, K., and P. G. Richards, 2002, Quantitative seismology.

Al-Harrasi, O., J.-M. Kendall, and M. Chapman, 2011, Fracture characterization using frequency-dependent shear wave anisotropy analysis of microseismic data: Geophysical Journal International, **185**, 1059–1070.

Alford, R., 1986, Shear data in the presence of azimuthal anisotropy: Dilley, texas, *in* SEG Technical Program Expanded Abstracts 1986: Society of Exploration Geophysicists, 476–479.

Ali, A., and M. Jakobsen, 2011, Seismic characterization of reservoirs with multiple fracture sets using velocity and attenuation anisotropy data: Journal of Applied Geophysics, **75**, 590–602.

———, 2014, Anisotropic permeability in fractured reservoirs from frequency-dependent seismic amplitude versus angle and azimuth data: Geophysical prospecting, **62**, 293–314.

Amalokwu, K., A. I. Best, and M. Chapman, 2016, Effects of aligned fractures on the response of velocity and attenuation ratios to water saturation variation: A laboratory study using synthetic sandstones: Geophysical Prospecting, **64**, 942–957.

Amalokwu, K., M. Chapman, A. I. Best, T. A. Minshull, and X.-Y. Li, 2015, Water saturation effects on p-wave anisotropy in synthetic sandstone with aligned fractures: Geophysical Journal International, **202**, 1088–1095.

Amalokwu, K., M. Chapman, A. I. Best, J. Sothcott, T. A. Minshull, and X.-Y. Li, 2014, Experimental observation of water saturation effects on shear wave splitting in synthetic rock with fractures aligned at oblique angles: Geophysical Journal International, **200**, 17–24.

Ass'ad, J. M., R. H. Tatham, and J. A. McDonald, 1992, A physical model study of microcrack-induced anisotropy: Geophysics, **57**, 1562–1570.

Auld, B. A., 1990, Acoustic fields and waves in solids: RE Krieger.

Baird, A. F., J.-M. Kendall, and D. A. Angus, 2013, Frequency-dependent seismic anisotropy due to fractures: Fluid flow versus scattering: Geophysics, **78**, WA111–WA122.

Bakulin, A., V. Grechka, and I. Tsvankin, 2000a, Estimation of fracture parameters from reflection seismic data?part i: Hti model due to a single fracture set: Geophysics, **65**, 1788–1802.

———, 2000b, Estimation of fracture parameters from reflection seismic data?part ii: Fractured models with orthorhombic symmetry: Geophysics, **65**, 1803–1817.

———, 2000c, Estimation of fracture parameters from reflection seismic data?part iii: Fractured models with monoclinic symmetry: Geophysics, **65**, 1818–1830.

Bandyopadhyay, K., 2009, Seismic anisotropy: Geological causes and its implications to reservoir geophysics: Stanford University.

Barbosa, N. D., J. Rubino, E. Caspari, and K. Holliger, 2017, Sensitivity of seismic attenuation and phase velocity to intrinsic background anisotropy in fractured porous rocks: A numerical study: Journal of Geophysical Research: Solid Earth, **122**, 8181–8199.

Barbosa, N. D., J. G. Rubino, E. Caspari, and K. Holliger, 2018, Impact of fracture clustering on the seismic signatures of porous rocks containing aligned fractures: Geophysics, **83**, 1–54.

Batzle, M. L., D.-H. Han, and R. Hofmann, 2006, Fluid mobility and frequency-

dependent seismic velocity—direct measurements: Geophysics, **71**, N1–N9.

Benson, S., R. Pini, C. Reynolds, and S. Krevor, 2013, Relative permeability analyses to describe multi-phase flow in co2 storage reservoirs: Global CCS Institute.

Berkowitz, B., 2002, Characterizing flow and transport in fractured geological media: A review: Advances in water resources, **25**, 861–884.

Biot, M. A., 1941, General theory of three-dimensional consolidation: Journal of applied physics, **12**, 155–164.

———, 1956, Theory of propagation of elastic waves in a fluid-saturated porous solid. i. low-frequency range, ii. higher frequency range: the Journal of the Acoustical Society of America, **28**, 168–191.

Brajanovski, M., B. Gurevich, and M. Schoenberg, 2005, A model for p-wave attenuation and dispersion in a porous medium permeated by aligned fractures: Geophysical Journal International, **163**, 372–384.

Brajanovski, M., T. M. Müller, and B. Gurevich, 2006, Characteristic frequencies of seismic attenuation due to wave-induced fluid flow in fractured porous media: Geophysical Journal International, **166**, 574–578.

Brie, A., F. Pampuri, A. Marsala, O. Meazza, et al., 1995, Shear sonic interpretation in gas-bearing sands: Presented at the SPE Annual Technical Conference and Exhibition, Society of Petroleum Engineers.

Brooks, R., and T. Corey, 1964, Hydrau uc properties of porous media: Hydrology Papers, Colorado State University, **24**, 37.

Brown, R. J., and J. Korringa, 1975, On the dependence of the elastic properties of a porous rock on the compressibility of the pore fluid: Geophysics, **40**, 608–616.

Burnside, N., and M. Naylor, 2014, Review and implications of relative permeability of co2/brine systems and residual trapping of co2: International Journal of Greenhouse Gas Control, **23**, 1–11.

Carcione, J. M., B. Gurevich, and F. Cavallini, 2000, A generalized biot–gassmann model for the acoustic properties of shaley sandstones1: Geophysical Prospecting, **48**, 539–557.

Carcione, J. M., B. Gurevich, J. E. Santos, and S. Picotti, 2013, Angular and frequency-dependent wave velocity and attenuation in fractured porous media: Pure and Applied Geophysics, **170**, 1673–1683.

Carcione, J. M., H. B. Helle, and N. H. Pham, 2003, White's model for wave propagation in partially saturated rocks: Comparison with poroelastic numerical experiments: Geophysics, **68**, 1389–1398.

Caspari, E., M. Milani, J. G. Rubino, T. M. Müller, B. Quintal, and K. Holliger, 2016, Numerical upscaling of frequency-dependent p-and s-wave moduli in fractured porous media: Geophysical Prospecting, **64**, 1166–1179.

Castagna, J. P., and H. W. Swan, 1997, Principles of avo crossplotting: The leading edge, **16**, 337–344.

Chapman, M., 2003, Frequency-dependent anisotropy due to meso-scale fractures in the presence of equant porosity: Geophysical Prospecting, **51**, 369–379.

———, 2009, Modeling the effect of multiple sets of mesoscale fractures in porous rock on frequency-dependent anisotropy: Geophysics, **74**, D97–D103.

Chapman, M., and E. Liu, 2003, The frequency dependent azimuthal avo response of fractured rock.: Presented at the 2003 SEG Annual Meeting.

Chapman, M., E. Liu, and X.-Y. Li, 2006, The influence of fluid sensitive dispersion and attenuation on avo analysis: Geophysical Journal International, **167**, 89–105.

Chapman, M., S. Maultzsch, E. Liu, and X.-Y. Li, 2003, The effect of fluid saturation in an anisotropic multi-scale equant porosity model: Journal of Applied Geophysics, **54**, 191–202.

Chapman, M., S. V. Zatsepin, and S. Crampin, 2002, Derivation of a microstructural poroelastic model: Geophysical Journal International, **151**, 427–451.

Chen, H., and G. Zhang, 2017, Estimation of dry fracture weakness, porosity, and fluid modulus using observable seismic reflection data in a gas-bearing reservoir: Surveys in Geophysics, **38**, 651–678.

Cheng, C., 1993, Crack models for a transversely isotropic medium: Journal of Geophysical Research: Solid Earth, **98**, 675–684.

Chesnokov, E. M., J. H. Queen, A. A. Vichorev, H. B. Lynn, J. M. Hooper, I. O. Bayuk, J. A. Castagna, B. Roy, et al., 2001, Frequency dependent anisotropy: Presented at the 2001 SEG Annual Meeting, Society of Exploration Geophysicists.

Chichinina, T., V. Sabinin, and G. Ronquillo-Jarillo, 2006, Qvoa analysis: P-wave attenuation anisotropy for fracture characterization: Geophysics, **71**, C37–C48.

Collet, O., and B. Gurevich, 2016, Frequency dependence of anisotropy in fluid saturated rocks–part i: aligned cracks case: Geophysical Prospecting, **64**, 1067–1084.

Crampin, S., 1978, Seismic-wave propagation through a cracked solid: polarization as a possible dilatancy diagnostic: Geophysical Journal International, **53**, 467–496.

———, 1985, Evaluation of anisotropy by shear-wave splitting: Geophysics, **50**, 142–152.

Crampin, S., E. M. Chesnokov, and R. A. Hipkin, 1984, Seismic anisotropy-the state of the art: First break, **2**, 9–18.

Dmitriev, N., and V. Maksimov, 1998, On the structure of tensors of the coefficients for phase and relative penetrabilities of anisotropic porous media: Physics-Doklady, 56–58.

Dmitriyev, N., and V. Maksimov, 2001, Non-linear laws of fluid flow through anisotropic porous media: Journal of applied Mathematics and Mechanics, **65**, 935–940.

Domenico, S., 1976, Effect of brine-gas mixture on velocity in an unconsolidated sand reservoir: Geophysics, **41**, 882–894.

———, 1977, Elastic properties of unconsolidated porous sand reservoirs: Geophysics, **42**, 1339–1368.

Dutta, N., and H. Odé, 1979, Attenuation and dispersion of compressional waves in fluid-filled porous rocks with partial gas saturation (white model)?part ii: Results: Geophysics, **44**, 1789–1805.

Dutta, N., and A. Seriff, 1979, On white?s model of attenuation in rocks with partial gas saturation: Geophysics, **44**, 1806–1812.

Dvorkin, J., G. Mavko, and A. Nur, 1995, Squirt flow in fully saturated rocks: Geophysics, **60**, 97–107.

Dvorkin, J., and A. Nur, 1993, Dynamic poroelasticity: A unified model with the squirt

and the biot mechanisms: Geophysics, **58**, 524–533.

Ecker, C., J. Dvorkin, and A. Nur, 1998, Sediments with gas hydrates: Internal structure from seismic avo: Geophysics, **63**, 1659–1669.

Ecker, C., J. Dvorkin, and A. M. Nur, 2000, Estimating the amount of gas hydrate and free gas from marine seismic data: Geophysics, **65**, 565–573.

Ekanem, A., X. Li, M. Chapman, and I. Main, 2016, Effects of co2 on p-wave attenuation in porous media with micro-cracks: A synthetic modelling study: Journal of Applied Geophysics, **135**, 309–316.

Engelder, T., G. G. Lash, and R. S. Uzcátegui, 2009, Joint sets that enhance production from middle and upper devonian gas shales of the appalachian basin: AAPG bulletin, **93**, 857–889.

Eshelby, J. D., 1957, The determination of the elastic field of an ellipsoidal inclusion, and related problems: Proceedings of the Royal Society of London A: Mathematical, Physical and Engineering Sciences, The Royal Society, 376–396.

Falcon-Suarez, I., H. Marín-Moreno, F. Browning, A. Lichtschlag, K. Robert, L. J. North, and A. I. Best, 2017, Experimental assessment of pore fluid distribution and geomechanical changes in saline sandstone reservoirs during and after co2 injection: International Journal of Greenhouse Gas Control, **63**, 356–369.

Falcon-Suarez, I., G. Papageorgiou, A. Munoz, Z. Jin, M. Chapman, and A. I. Best, 2019, Co2-brine substitution effects on ultrasonic p- and s-wave velocities and attenuation in synthetic sandstone with fractures aligned at oblique angles: submitted.

Foster, D. J., R. G. Keys, and F. D. Lane, 2010, Interpretation of avo anomalies: Geophysics, **75**, 75A3–75A13.

Gaiser, J., N. Moldoveanu, C. Macbeth, R. Michelena, and S. Spitz, 2001, Multicomponent technology: The players, problems, applications, and trends: Summary of the workshop sessions: The Leading Edge, **20**, 974–977.

Galvin, R., and B. Gurevich, 2009, Effective properties of a poroelastic medium containing a distribution of aligned cracks: Journal of Geophysical Research: Solid Earth, **114**.

Galvin, R. J., and B. Gurevich, 2015, Frequency-dependent anisotropy of porous rocks with aligned fractures: Geophysical Prospecting, **63**, 141–150.

Gassmann, F., 1951, Über die elastizität poröser medien: Vierteljahrsschrift der Naturforschenden Gesellschaft in Zürich, **96**, 1–23.

Grechka, V., and M. Kachanov, 2006a, Effective elasticity of fractured rocks: A snapshot of the work in progress: Geophysics, **71**, W45–W58.

———, 2006b, Seismic characterization of multiple fracture sets: Does orthotropy suffice?: Geophysics, **71**, D93–D105.

Grechka, V., and I. Tsvankin, 1998, 3-d description of normal moveout in anisotropic inhomogeneous media: Geophysics, **63**, 1079–1092.

Green, G., 1848, On the laws of the reflexion and refraction of light at the common surface of two non-crystallized media: Transactions of the Cambridge Philosophical Society, **7**, 1.

Gregory, A., 1976, Fluid saturation effects on dynamic elastic properties of sedimentary rocks: Geophysics, **41**, 895–921.

Guo, J., J. G. Rubino, S. Glubokovskikh, and B. Gurevich, 2017, Effects of fracture intersections on seismic dispersion: theoretical predictions versus numerical simulations: Geophysical Prospecting, **65**, 1264–1276.

Gupta, I., 1974, Premonitory seismic-wave phenomena before 2 earthquakes in nevada: TRANSACTIONS-AMERICAN GEOPHYSICAL UNION, AMER GEOPHYSICAL UNION 2000 FLORIDA AVE NW, WASHINGTON, DC 20009, 355–355.

Gurevich, B., 2003, Elastic properties of saturated porous rocks with aligned fractures: Journal of Applied Geophysics, **54**, 203–218.

Gurevich, B., M. Brajanovski, R. J. Galvin, T. M. Müller, and J. Toms-Stewart, 2009, P-wave dispersion and attenuation in fractured and porous reservoirs–poroelasticity approach: Geophysical Prospecting, **57**, 225–237.

Gurevich, B., and S. Lopatnikov, 1995, Velocity and attenuation of elastic waves in finely layered porous rocks: Geophysical Journal International, **121**, 933–947.

Hall, S. A., and J.-M. Kendall, 2003, Fracture characterization at valhall: Application

of p-wave amplitude variation with offset and azimuth (avoa) analysis to a 3d ocean-bottom data set: Geophysics, **68**, 1150–1160.

Han, D.-h., and M. L. Batzle, 2004, Gassmann's equation and fluid-saturation effects on seismic velocities: Geophysics, **69**, 398–405.

Hardage, B. A., M. V. DeAngelo, P. E. Murray, and D. Sava, 2011, Multicomponent seismic technology: Society of Exploration Geophysicists.

Helbig, K., 1994, Foundations of anisotropy for exploration seismics: Pergamon Press.

Huang, L., R. R. Stewart, S. Sil, and N. Dyaur, 2015, Fluid substitution effects on seismic anisotropy: Journal of Geophysical Research: Solid Earth, **120**, 850–863.

Hudson, J., 1980, Overall properties of a cracked solid: Mathematical Proceedings of the Cambridge Philosophical Society, Cambridge Univ Press, 371–384.

Hudson, J., E. Liu, and S. Crampin, 1996, The mechanical properties of materials with interconnected cracks and pores: Geophysical Journal International, **124**, 105–112.

Hudson, J., T. Pointer, and E. Liu, 2001, Effective-medium theories for fluid-saturated materials with aligned cracks: Geophysical Prospecting, **49**, 509–522.

Hudson, J. A., 1981, Wave speeds and attenuation of elastic waves in material containing cracks: Geophysical Journal International, **64**, 133–150.

Hunt, L., S. Reynolds, T. Brown, S. Hadley, J. Downton, and S. Chopra, 2010, Quantitative estimate of fracture density variations in the nordegg with azimuthal avo and curvature a case study: The Leading Edge, **29**, 1122–1137.

Hunziker, J., M. Favino, E. Caspari, B. Quintal, J. G. Rubino, R. Krause, and K. Holliger, 2018, Seismic attenuation and stiffness modulus dispersion in porous rocks containing stochastic fracture networks: Journal of Geophysical Research: Solid Earth, **123**, 125–143.

Iding, M., and P. Ringrose, 2010, Evaluating the impact of fractures on the performance of the in salah co2 storage site: International Journal of Greenhouse Gas Control, **4**, 242–248.

Innanen, K. A., 2011, Inversion of the seismic avf/ava signatures of highly attenuative targets: Geophysics, **76**, R1–R14.

Jakobsen, M., and M. Chapman, 2009, Unified theory of global flow and squirt flow in cracked porous media: Geophysics, **74**, WA65–WA76.

Jakobsen, M., J. A. Hudson, and T. A. Johansen, 2003, T-matrix approach to shale acoustics: Geophysical Journal International, **154**, 533–558.

Jenner, E., 2002, Azimuthal avo: Methodology and data examples: The Leading Edge, **21**, 782–786.

Jin, Z., M. Chapman, X. Wu, and G. Papageorgiou, 2017, Estimating gas saturation in a thin layer by using frequency-dependent amplitude versus offset modelling: Geophysical Prospecting, **65**, 747–765.

Johnson, D. L., 2001, Theory of frequency dependent acoustics in patchy-saturated porous media: The Journal of the Acoustical Society of America, **110**, 682–694.

Jones, T. D., 1986, Pore fluids and frequency-dependent wave propagation in rocks: Geophysics, **51**, 1939–1953.

Kelder, O., and D. M. Smeulders, 1997, Observation of the biot slow wave in water-saturated nivelsteiner sandstone: Geophysics, **62**, 1794–1796.

King, M., J. Marsden, and J. Dennis, 2000, Biot dispersion for p-and s-wave velocities in partially and fully saturated sandstones: Geophysical Prospecting, **48**, 1075–1089.

King, M. S., 1966, Wave velocities in rocks as a function of changes in overburden pressure and pore fluid saturants: Geophysics, **31**, 50–73.

———, 2005, Rock-physics developments in seismic exploration: A personal 50-year perspective: Geophysics, **70**, 3ND–8ND.

King, M. S., and J. R. Marsden, 2002, Velocity dispersion between ultrasonic and seismic frequencies in brine-saturated reservoir sandstones: Geophysics, **67**, 254–258.

Knight, R., J. Dvorkin, and A. Nur, 1998, Acoustic signatures of partial saturation: Geophysics, **63**, 132–138.

Lebedev, M., J. Toms-Stewart, B. Clennell, M. Pervukhina, V. Shulakova, L. Paterson, T. M. Müller, B. Gurevich, and F. Wenzlau, 2009, Direct laboratory observation of patchy saturation and its effects on ultrasonic velocities: The Leading Edge, **28**, 24–27.

Li, X.-Y., 1997, Fractured reservoir delineation using multicomponent seismic data: Geo-

physical Prospecting, **45**, 39–64.

———, 1999, Fracture detection using azimuthal variation of p-wave moveout from orthogonal seismic survey lines: Geophysics, **64**, 1193–1201.

Liu, E., M. Chapman, I. Varela, X. Li, J. H. Queen, and H. Lynn, 2007, Velocity and attenuation anisotropy: Implication of seismic fracture characterizations: The Leading Edge, **26**, 1170–1174.

Liu, E., M. Chapman, Z. Zhang, and J. H. Queen, 2006, Frequency-dependent anisotropy: Effects of multiple fracture sets on shear-wave polarizations: Wave Motion, **44**, 44–57.

Liu, E., J. A. Hudson, and T. Pointer, 2000, Equivalent medium representation of fractured rock: Journal of Geophysical Research: Solid Earth, **105**, 2981–3000.

Liu, E., and A. Martinez, 2012, Seismic fracture characterization: Netherlands: EAGE Publication.

Liu, E., J. Queen, X. Li, M. Chapman, S. Maultzsch, H. Lynn, and E. Chesnokov, 2003, Observation and analysis of frequency-dependent anisotropy from a multicomponent vsp at bluebell-altamont field, utah: Journal of Applied Geophysics, **54**, 319–333.

Liu, W., S. Cao, Z. Jin, Z. Wang, and Y. Chen, 2018, A novel hydrocarbon detection approach via high-resolution frequency-dependent avo inversion based on variational mode decomposition: IEEE Transactions on Geoscience and Remote Sensing, **56**, 2007–2024.

Lu, H., X. Lu, J. Fan, M. Zhao, H. Wei, B. Zhang, and Y. Lu, 2016, Controlling effect of fractures on gas accumulation and production within the tight sandstone: A case study on the jurassic dibei gas reservoir in the eastern part of the kuqa foreland basin, china: Journal of Natural Gas Geoscience, **1**, 61–71.

Lynn, H. B., W. E. Beckham, K. M. Simon, C. R. Bates, M. Layman, and M. Jones, 1999, P-wave and s-wave azimuthal anisotropy at a naturally fractured gas reservoir, bluebell-altamont field, utah: Geophysics, **64**, 1312–1328.

Lynn, H. B., K. M. Simon, C. R. Bates, M. Layman, R. Schneider, and M. Jones, 1995, Use of anisotropy in p-wave and s-wave data for fracture characterization in a naturally fractured gas reservoir: The Leading Edge, **14**, 887–893.

Lynn, H. B., and L. A. Thomsen, 1986, Reflection shear-wave data along the principal axes of azimuthal anisotropy, *in* SEG Technical Program Expanded Abstracts 1986: Society of Exploration Geophysicists, 473–476.

MacBeth, C., 2002, Multi-component vsp analysis for applied seismic anisotropy: Elsevier.

Maksimov, V. M., and N. M. Dmitriev, 2013, A new approach to the study of a representative anisotropic core sample and two-phase flow in anisotropic filtering porous environments: Nafta-Gaz, **69**, 302–309.

Marson-Pidgeon, K., and M. K. Savage, 1997, Frequency-dependent anisotropy in wellington, new zealand: Geophysical Research Letters, **24**, 3297–3300.

Martin, M. A., and T. L. Davis, 1987, Shear-wave birefringence: A new tool for evaluating fractured reservoirs: The Leading Edge, **6**, 22–28.

Maultzsch, S., M. Chapman, E. Liu, and X. Y. Li, 2003a, Modelling frequency-dependent seismic anisotropy in fluid-saturated rock with aligned fractures: implication of fracture size estimation from anisotropic measurements: Geophysical Prospecting, **51**, 381–392.

Maultzsch, S., S. Horne, S. Archer, and H. Burkhardt, 2003b, Effects of an anisotropic overburden on azimuthal amplitude analysis in horizontal transverse isotropic media: Geophysical Prospecting, **51**, 61–74.

Mavko, G., and D. Jizba, 1991, Estimating grain-scale fluid effects on velocity dispersion in rocks: Geophysics, **56**, 1940–1949.

Mavko, G., and T. Mukerji, 1995, Seismic pore space compressibility and gassmann?s relation: Geophysics, **60**, 1743–1749.

———, 1998a, Bounds on low-frequency seismic velocities in partially saturated rocks: Geophysics, **63**, 918–924.

———, 1998b, A rock physics strategy for quantifying uncertainty in common hydrocarbon indicators: Geophysics, **63**, 1997–2008.

Mavko, G., T. Mukerji, and J. Dvorkin, 2009, The rock physics handbook: Tools for seismic analysis of porous media: Cambridge university press.

Mavko, G., and A. Nur, 1975, Melt squirt in the asthenosphere: Journal of Geophysical Research, **80**, 1444–1448.

Milani, M., L. Monachesi, J. I. Sabbione, J. G. Rubino, and K. Holliger, 2016, A generalized effective anisotropic poroelastic model for periodically layered media accounting for both biot's global and interlayer flows: Geophysical Prospecting, **64**, 1135–1148.

Mueller, M. C., 1991, Prediction of lateral variability in fracture intensity using multicomponent shear-wave surface seismic as a precursor to horizontal drilling in the austin chalk: Geophysical Journal International, **107**, 409–415.

Mukerji, T., and G. Mavko, 1994, Pore fluid effects on seismic velocity in anisotropic rocks: Geophysics, **59**, 233–244.

Müller, T., and E. Rothert, 2006, Seismic attenuation due to wave-induced flow: Why q in random structures scales differently: Geophysical Research Letters, **33**.

Müller, T. M., and B. Gurevich, 2005, A first-order statistical smoothing approximation for the coherent wave field in random porous media: The Journal of the Acoustical Society of America, **117**, 1796–1805.

Müller, T. M., B. Gurevich, and M. Lebedev, 2010, Seismic wave attenuation and dispersion resulting from wave-induced flow in porous rocks?a review: Geophysics, **75**, 75A147–75A164.

Murphy, W. F., 1982, Effects of partial water saturation on attenuation in massilon sandstone and vycor porous glass: The Journal of the Acoustical Society of America, **71**, 1458–1468.

———, 1984, Acoustic measures of partial gas saturation in tight sandstones: Journal of Geophysical Research: Solid Earth, **89**, 11549–11559.

Narr, W., D. S. Schechter, and L. B. Thompson, 2006, Naturally fractured reservoir characterization: Society of Petroleum Engineers Richardson, Texas.

Nelson, R., 2001, Geologic analysis of naturally fractured reservoirs: Elsevier.

Norris, A. N., 1993, Low-frequency dispersion and attenuation in partially saturated rocks: The Journal of the Acoustical Society of America, **94**, 359–370.

O'Connell, R. J., and B. Budiansky, 1974, Seismic velocities in dry and saturated cracked

solids: Journal of Geophysical Research, **79**, 5412–5426.

Odebeatu, E., J. Zhang, M. Chapman, E. Liu, and X.-Y. Li, 2006, Application of spectral decomposition to detection of dispersion anomalies associated with gas saturation: The Leading Edge, **25**, 206–210.

Olofsson, B., T. Probert, J. H. Kommedal, and O. I. Barkved, 2003, Azimuthal anisotropy from the valhall 4c 3d survey: The Leading Edge, **22**, 1228–1235.

Ostrander, W., 1984, Plane-wave reflection coefficients for gas sands at nonnormal angles of incidence: Geophysics, **49**, 1637–1648.

Papageorgiou, G., K. Amalokwu, and M. Chapman, 2016, Theoretical derivation of a brie-like fluid mixing law: Geophysical Prospecting, **64**, 1048–1053.

Papageorgiou, G., and M. Chapman, 2015, Multifluid squirt flow and hysteresis effects on the bulk modulus–water saturation relationship: Geophysical Journal International, **203**, 814–817.

———, 2017, Wave-propagation in rocks saturated by two immiscible fluids: Geophysical Journal International, **209**, 1761–1767.

Plona, T. J., 1980, Observation of a second bulk compressional wave in a porous medium at ultrasonic frequencies: Applied physics letters, **36**, 259–261.

Pointer, T., E. Liu, and J. A. Hudson, 2000, Seismic wave propagation in cracked porous media: Geophysical Journal International, **142**, 199–231.

Pride, S. R., and J. G. Berryman, 2003, Linear dynamics of double-porosity dual-permeability materials. i. governing equations and acoustic attenuation: Physical Review E, **68**, 036603.

Pride, S. R., J. G. Berryman, and J. M. Harris, 2004, Seismic attenuation due to wave-induced flow: Journal of Geophysical Research: Solid Earth, **109**.

Pyrak-Nolte, L. J., and D. D. Nolte, 1992, Frequency dependence of fracture stiffness: Geophysical Research Letters, **19**, 325–328.

Qian, Z., M. Chapman, X.-Y. Li, H.-C. Dai, E. Liu, Y. Zhang, and Y. Wang, 2007, Use of multicomponent seismic data for oil-water discrimination in fractured reservoirs: The Leading Edge, **26**, 1176–1184.

Quintal, B., R. Jänicke, J. G. Rubino, H. Steeb, and K. Holliger, 2014, Sensitivity of s-wave attenuation to the connectivity of fractures in fluid-saturated rocks: Geophysics, **79**, WB15–WB24.

Quintal, B., S. M. Schmalholz, and Y. Y. Podladchikov, 2008, Low-frequency reflections from a thin layer with high attenuation caused by interlayer flow: Geophysics, **74**, N15–N23.

Quintal, B., H. Steeb, M. Frehner, and S. M. Schmalholz, 2011, Quasi-static finite element modeling of seismic attenuation and dispersion due to wave-induced fluid flow in poroelastic media: Journal of Geophysical Research: Solid Earth, **116**.

Quintal, B., H. Steeb, M. Frehner, S. M. Schmalholz, and E. H. Saenger, 2012, Pore fluid effects on s-wave attenuation caused by wave-induced fluid flowpore fluid effects on s-wave attenuation: Geophysics, **77**, L13–L23.

Rathore, J., E. Fjaer, R. Holt, and L. Renlie, 1995, P-and s-wave anisotropy of a synthetic sandstone with controlled crack geometryl 1: Geophysical Prospecting, **43**, 711–728.

Ren, H., G. Goloshubin, and F. J. Hilterman, 2009, Poroelastic analysis of amplitude-versus-frequency variations: Geophysics, **74**, N41–N48.

Rubino, J., E. Caspari, T. M. Müller, and K. Holliger, 2017, Fracture connectivity can reduce the velocity anisotropy of seismic waves: Geophysical Journal International, **210**, 223–227.

Rubino, J., T. M. Müller, L. Guarracino, M. Milani, and K. Holliger, 2014, Seismoacoustic signatures of fracture connectivity: Journal of Geophysical Research: Solid Earth, **119**, 2252–2271.

Rubino, J. G., E. Caspari, T. M. Müller, M. Milani, N. D. Barbosa, and K. Holliger, 2016, Numerical upscaling in 2-d heterogeneous poroelastic rocks: Anisotropic attenuation and dispersion of seismic waves: Journal of Geophysical Research: Solid Earth, **121**, 6698–6721.

Rubino, J. G., L. Guarracino, T. M. Müller, and K. Holliger, 2013, Do seismic waves sense fracture connectivity?: Geophysical Research Letters, **40**, 692–696.

Rubino, J. G., and K. Holliger, 2012, Seismic attenuation and velocity dispersion in het-

erogeneous partially saturated porous rocks: Geophysical Journal International, **188**, 1088–1102.

Rubino, J. G., C. L. Ravazzoli, and J. E. Santos, 2009, Equivalent viscoelastic solids for heterogeneous fluid-saturated porous rocks: Geophysics, **74**, N1–N13.

Rueger, A., and I. Tsvankin, 1997, Using avo for fracture detection: Analytic basis and practical solutions: The Leading Edge, **16**, 1429–1434.

Rüger, A., 1997, P-wave reflection coefficients for transversely isotropic models with vertical and horizontal axis of symmetry: Geophysics, **62**, 713–722.

———, 1998, Variation of p-wave reflectivity with offset and azimuth in anisotropic media: Geophysics, **63**, 935–947.

Rutherford, S. R., and R. H. Williams, 1989, Amplitude-versus-offset variations in gas sands: Geophysics, **54**, 680–688.

Sams, M., J. Neep, M. Worthington, and M. King, 1997, The measurement of velocity dispersion and frequency-dependent intrinsic attenuation in sedimentary rocks: Geophysics, **62**, 1456–1464.

Sayers, C., 1994, The elastic anisotrophy of shales: Journal of Geophysical Research: Solid Earth, **99**, 767–774.

Sayers, C. M., 1998, Misalignment of the orientation of fractures and the principal axes for p and s waves in rocks containing multiple non-orthogonal fracture sets: Geophysical Journal International, **133**, 459–466.

Sayers, C. M., and J. E. Rickett, 1997, Azimuthal variation in avo response for fractured gas sands: Geophysical Prospecting, **45**, 165–182.

Schoenberg, M., 1980, Elastic wave behavior across linear slip interfaces: The Journal of the Acoustical Society of America, **68**, 1516–1521.

———, 1983, Reflection of elastic waves from periodically stratified media with interfacial slip: Geophysical Prospecting, **31**, 265–292.

Schoenberg, M., and J. Douma, 1988, Elastic wave propagation in media with parallel fractures and aligned cracks: Geophysical Prospecting, **36**, 571–590.

Schoenberg, M., and J. Protázio, 1992, 'zoeppritz' rationalized and generalized to

anisotropy: Journal of Seismic Exploration, **1**, 125–144.

Schoenberg, M., and C. M. Sayers, 1995, Seismic anisotropy of fractured rock: Geophysics, **60**, 204–211.

Shapiro, S. A., E. Rothert, V. Rath, and J. Rindschwentner, 2002, Characterization of fluid transport properties of reservoirs using induced microseismicity: Geophysics, **67**, 212–220.

Shuey, R., 1985, A simplification of the zoeppritz equations: Geophysics, **50**, 609–614.

Sondergeld, C., and C. Rai, 1992, Laboratory observations of shear-wave propagation in anisotropic media: The leading edge, **11**, 38–43.

Spikes, K., T. Mukerji, J. Dvorkin, and G. Mavko, 2007, Probabilistic seismic inversion based on rock-physics models: Geophysics, **72**, R87–R97.

Thomsen, L., 1986, Weak elastic anisotropy: Geophysics, **51**, 1954–1966.

———, 1995, Elastic anisotropy due to aligned cracks in porous rock: Geophysical Prospecting, **43**, 805–829.

Tillotson, P., M. Chapman, A. I. Best, J. Sothcott, C. McCann, W. Shangxu, and X.-Y. Li, 2011, Observations of fluid-dependent shear-wave splitting in synthetic porous rocks with aligned penny-shaped fractures: Geophysical Prospecting, **59**, 111–119.

Tillotson, P., M. Chapman, J. Sothcott, A. I. Best, and X.-Y. Li, 2014, Pore fluid viscosity effects on p-and s-wave anisotropy in synthetic silica-cemented sandstone with aligned fractures: Geophysical Prospecting, **62**, 1238–1252.

Tillotson, P., J. Sothcott, A. I. Best, M. Chapman, and X.-Y. Li, 2012, Experimental verification of the fracture density and shear-wave splitting relationship using synthetic silica cemented sandstones with a controlled fracture geometry: Geophysical Prospecting, **60**, 516–525.

Tisato, N., and B. Quintal, 2013, Measurements of seismic attenuation and transient fluid pressure in partially saturated berea sandstone: evidence of fluid flow on the mesoscopic scale: Geophysical Journal International, **195**, 342–351.

Tisato, N., B. Quintal, S. Chapman, Y. Podladchikov, and J.-P. Burg, 2015, Bubbles attenuate elastic waves at seismic frequencies: First experimental evidence: Geophysical

Research Letters, **42**, 3880–3887.

Toms, J., T. M. Müller, and B. Gurevich, 2007, Seismic attenuation in porous rocks with random patchy saturation: Geophysical Prospecting, **55**, 671–678.

Tsvankin, I., 1995, Body-wave radiation patterns and avo in transversely isotropic media: Geophysics, **60**, 1409–1425.

———, 1997a, Anisotropic parameters and p-wave velocity for orthorhombic media: Geophysics, **62**, 1292–1309.

———, 1997b, Reflection moveout and parameter estimation for horizontal transverse isotropy: Geophysics, **62**, 614–629.

———, 2001, Seismic signatures and analysis of reflection data in anisotropic media: Elsevier.

Tsvankin, I., J. Gaiser, V. Grechka, M. Van Der Baan, and L. Thomsen, 2010, Seismic anisotropy in exploration and reservoir characterization: An overview: Geophysics, **75**, 75A15–75A29.

Tsvankin, I., and V. Grechka, 2011, Seismology of azimuthally anisotropic media and seismic fracture characterization: Society of Exploration Geophysicists Tulsa, OK.

Van der Kolk, C., W. Guest, and J. Potters, 2001, The 3d shear experiment over the natih field in oman: the effect of fracture-filling fluids on shear propagation: Geophysical Prospecting, **49**, 179–197.

Walsh, J., 1965, The effect of cracks on the compressibility of rock: Journal of Geophysical Research, **70**, 381–389.

Wang, S., X.-Y. Li, Z. Qian, B. Di, and J. Wei, 2007, Physical modelling studies of 3-dp-wave seismic for fracture detection: Geophysical Journal International, **168**, 745–756.

Wang, Y., S. Chen, and X.-Y. Li, 2015, Anisotropic characteristics of mesoscale fractures and applications to wide azimuth 3d p-wave seismic data: Journal of Geophysics and Engineering, **12**, 448.

Wang, Z., 2001, Fundamentals of seismic rock physics: Geophysics, **66**, 398–412.

Wang, Z., and A. Nur, 1990, Dispersion analysis of acoustic velocities in rocks: The Journal of the Acoustical Society of America, **87**, 2384–2395.

White, J., 1975, Computed seismic speeds and attenuation in rocks with partial gas saturation: Geophysics, **40**, 224–232.

———, 1983, Underground sound: Application of seismic waves: Elsevier. Methods in geochemistry and geophysics.

Winkler, K. W., 1985, Dispersion analysis of velocity and attenuation in berea sandstone: Journal of Geophysical Research: Solid Earth (1978–2012), **90**, 6793–6800.

Wu, X., M. Chapman, X.-Y. Li, and P. Boston, 2014, Quantitative gas saturation estimation by frequency-dependent amplitude-versus-offset analysis: Geophysical Prospecting, **62**, 1224–1237.

Wu, Y.-S., 2015, Multiphase fluid flow in porous and fractured reservoirs: Gulf Professional Publishing.

Xu, S., 1998, Modelling the effect of fluid communication on velocities in anisotropic porous rocks: International Journal of Solids and Structures, **35**, 4685–4707.

Xu, X., and I. Tsvankin, 2006, Anisotropic geometrical-spreading correction for wide-azimuth p-wave reflections: Geophysics, **71**, D161–D170.

Yang, L., X. Wu, and M. Chapman, 2015, Impacts of kerogen content and fracture properties on the anisotropic seismic reflectivity of shales with orthorhombic symmetry: Interpretation, **3**, ST1–ST7.

Zatsepin, S. V., and S. Crampin, 1997, Modelling the compliance of crustal rock- i. response of shear-wave splitting to differential stress: Geophysical Journal International, **129**, 477–494.

Zoeppritz, K., 1919, On the reflection and propagation of seismic waves at discontinuities: Erdbebenwellen VII B, 66–84.

Publications

Chapters 4, 5 and 6 in this thesis have been published as

Jin, Z., M. Chapman, and G. Papageorgiou, 2018, Frequency-dependent anisotropy in a partially saturated fractured rock: Geophysical Journal International, **215**, 1985–1998.

Jin, Z., M. Chapman, G. Papageorgiou, and X. Wu, 2018, Impact of frequency-dependent anisotropy on azimuthal P-wave reflections: Journal of Geophysics and Engineering, **15**, 2530–2544.